Application of Nanostructured Materials and Multi-junction Structure in Polymer Solar Cells

Dissertation by

Yangqin Gao

In Partial Fulfillment of the Requirements

For the Degree of

Doctor of Philosophy of Science

King Abdullah University of Science and Technology

Thuwal, Kingdom of Saudi Arabia

December 2015

The dissertation of Yangqin Gao is approved by the examination committee.

Committee Chairperson: Prof. Pierre M. Beaujuge

Committee Member: Prof. Osman Bakr

Committee Member: Prof. Boon S. Ooi

Committee Member: Prof. Edward H. Sargent

December 2015

Yangqin Gao

ABSTRACT

Application of Nanostructured Materials and Multi-junction Structure in Polymer Solar Cells

Yangqin Gao

With power conversion efficiency surpassing the 10% milestone for commercialization, photovoltaic technology based on solution-processable polymer solar cells (PSCs) provides a promising route towards a cost-efficient strategy to address the ever-increasing worldwide energy demands. However, to make PSCs successful, challenges such as insufficient light absorption, high maintenance costs, and relatively high production costs must be addressed. As solutions to some of these problems, the unique properties of nanostructured materials and complimentary light absorption in multi-junction device structure could prove to be highly beneficial.

As a starting point, integrating nanostructure-based transparent self-cleaning surfaces in PSCs was investigated first. By controlling the length of the hydrothermally grown ZnO nanorods and covering their surface with a thin layer of chemical vapor-deposited SiO_2, a highly transparent and UV-resistant superhydrophobic surface was constructed. Integrating the transparent superhydrophobic surface in a PSC shows minimal impact on the figure of merit of the PSC. To address the low mechanical durability of the transparent superhydrophobic surface based on SiO_2-coated ZnO nanorods, a novel method inspired by the water condensation process was developed. This method involved directly growing hollow silica half-nanospheres on the substrate through the

condensation of water in the presence of a silica precursor. Benefit from the decreased back scattering efficiency and increased light transport mean free path arise from the hollow nature, a transparent superhydrophobic surface was realized using submicrometer sized silica half-nanospheres. The decent mechanical property of silica and the "direct-grown" protocol are expected to impart improved mechanical durability to the transparent superhydrophobic surface.

Regarding the application of multi-junction device structure in PSCs, homo multi-junction PSCs were constructed from an identical polymer absorber, in which the homo-tandem device showed an enhanced power conversion efficiency (PCE) (8.3% vs 7.7%) relative to the optimized single junction PSC. The high open voltage (>1.8 V) achieved in homo-tandem PSCs allowed for water splitting with an estimated solar-to-fuel conversion efficiency of 6%.

Lastly, a hybrid tandem cell was also constructed using a polymer and a colloidal quantum dot subcell. Different hybrid tandem device architectures were proposed and show a promising PCE of 6.7%.

ACKNOWLEDGEMENTS

First of all, I would like to express my sincere appreciation to KAUST, my ex-advisor Prof. Ghassan Jabbour, and my dissertation advisor Prof. Pierre M. Beaujuge for accepting me as a PhD student and providing the scientific environment to support my study.

I would like to extend my special appreciation and thanks to my dissertation advisor, Prof. Pierre M. Beaujuge, for his guidance, encouragement, and patience, which allowed me to improve myself. Prof. Beaujuge has been an extremely passionate advisor and I greatly appreciate the opportunity to be mentored by him. Having a serious research attitude and working systematically are some of what I learned from him, which will accompany me for my whole life.

I would also like to thank my committee members, Prof. Osman Bakr, Prof. Boon S. Ooi, Prof. Peng Wang and Prof. Edward H. Sargent, for their unconditional support, valuable suggestions and warm encouragement throughout the course of this study. Special thanks go to Prof. Edward H. Sargent and Dr Zhijun Ning, Dr Sjoerd Hoogland, and Dr Michael M. Adachi in his group for their scientific contributions in the hybrid tandem work.

I owe my sincere gratitude to all of my colleagues and collaborators. Thanks to Dr Tayirjan T. Isimjan and Dr Issam Gereige for leading me to the superhydrophobic field. The fruitful discussions with them inspired me to deeply explore the extraordinary behavior of water on surfaces. A sincere thank you to Dr Abdulrahman El Labban for

setting up the solar cell fabrication equipment and personally training me. Without his contribution, this work would have been thoroughly difficult to complete. I would also like to thank Prof. Kazuhiro Takanabe and Mr Tatsuya Shinagawa in his group for their help and patient explanation of the water splitting experiment. I would like to thank Prof. Aram Amassian and Dr Taesoo Kim in his group for their continuous support and collaboration in the hybrid tandem work. My appreciation also goes to all of the members of the Beaujuge group for their valuable advice and support as friends. They made my experience in the lab stimulating, enjoyable, and fun. Special thanks goes to Ms Yuanfang Hou for her work in nanostructure characterization, Mr Federico Cruciani, Mr Mahmoud Abdul Hamid, Dr Julien Warnan, Dr Clément Cabanetos, and Dr Shengjian Liu for their hard work in the synthesis of fascinating polymers, and Dr Qasim Saleem and Dr Marios Neophytou for their help in polishing this dissertation.

Finally, I would like to thank my family and friends for all of their emotional support. No matter the failures and frustration I encountered every day, they were always there and encouraged me not to give up. Without the support and encouragement of my parents and my sister, I could not have finished 5 years of study away from home. My final appreciation goes to my girlfriend, Liping Feng, for all her support and everything she has done for me. I feel flattered to have her love, and her understanding for the short time I could be with her during graduate school.

TABLE OF CONTENTS

ABSTRACT 4
ACKNOWLEDGEMENTS 6
TABLE OF CONTENTS 8
LIST OF ABBREVIATIONS 10
LIST OF ILLUSTRATIONS 12
LIST OF TABLES 18
Chapter 1 Introduction and Motivation 19
1.1 World Power Demand 19
1.2 Polymer Solar Cell 22
1.2.1 Properties of Conjugated Polymer 22
1.2.2 Device Architectures 25
1.2.3 Challenges and Motivation 29
1.3 Application of Nanostructured Materials to PSCs 30
1.3.1 Self-Cleaning PSCs 31
1.3.1.1 The Self-Cleaning Surface 31
1.3.1.2 Transparent Self-Cleaning Surfaces 35
1.3.1.3 Mechanically Durable Transparent Self-Cleaning Surface 37
1.3.2 Light Trapping by Nanostructured Materials 40
1.4 Application of Multi-junction Structures to PSCs 43
1.5 Objective and Organization of the Dissertation 45
Chapter 2 Highly Transparent and UV-Resistant Superhydrophobic SiO_2-Coated ZnO Nanorod Arrays 49
2.1 Introduction 49
2.2 Experimental Section 51
2.2.1 Preparation of the SiO_2-coated ZnO Nanorod Arrays 51
2.2.2 Characterization Procedures and Supporting Analyses 54
2.3 Results and Discussion 56

2.4 Conclusion 71
Chapter 3 Arrays of Hollow Silica Half-Nanospheres via the Breath Figure Approach 73
3.1 Introduction 74
3.2 Experimental Section 76
3.3 Results and discussion 82
3.4 Conclusion and Perspectives 104
Chapter 4 Homo-Tandem Polymer Solar Cells with V_{OC} > 1.8 V for Efficient PV-driven Water Splitting 106
4.1 Introduction 106
4.2 Experimental Section 109
4.2.1 Materials and Synthesis 109
4.2.2 Solar Cell Device Fabrication and Characterization 110
4.3 Results and Discussion 114
4.4 Conclusion 134
Chapter 5 Hybrid Colloidal Quantum Dot-Polymer Bulk Heterojunction Tandem Solar Cells 135
5.1 Introduction 135
5.2 Experimental Section 137
5.2.1 Materials and Synthesis 137
5.2.2 Solar Cell Device Fabrication 138
5.3 Results and Discussion 142
5.4 Conclusion 154
Chapter 6 Conclusions and Future Work 156
6.1 Conclusions 156
6.2 Future work 159
REFERENCES 165
LIST OF PBLICATIONS 178

LIST OF ABBREVIATIONS

BF	Breath figure
BHJ	Bulk-heterojunction
CQD	Colloidal quantum dots
CVD	Chemical vapor deposition
DANs	Nanoimprinted deterministic aperiodic nanostructures
DH-CQD	Depleted-heterojunction colloidal quantum dots
EDX	Energy-dispersive X-ray spectroscopy
EQE	External quantum efficiency
FF	Fill factor
FTO	Fluorine-tin-oxide
GW	Gigawatt
IQE	Internal quantum efficiency
ITO	Tin-doped indium oxide
J_{SC}	Short-circuit currents
MPA	3-mercaptopropionic acid
NIR	Near infrared
NP	Nanoparticle
OPV	Organic photovoltaic
PBDTTPD	Poly(benzo[1,2-*b*:4,5-*b'*]dithiophene–thieno[3,4-*c*]pyrrole-4,6-dione)
$PC_{71}BM$	[6,6]-phenyl-C71-butyric acid methyl ester

PCE	Power conversion efficiency
PDMS	Polydimethylsiloxane
PEDOT:PSS	Poly(3,4-ethylenedioxythiophene): poly(styrenesulfonate)
PET	Poly(ethylene terephtalate)
PV	Photovoltaic
PMMA	Poly(methyl methacrylate)
PS	Polystyrene
PSCs	Polymer solar cells
PTCS	1H,1H,2H,2H-Perfluorododecyltrichlorosilane
PTES	1H,1H,2H,2H-perfluorodecyltriethoxysilane
RMS	Room mean square
SEM	Scanning electron microscopy
TEM	Transmission electron microscopy
TEOS	Tetraethoxysilane
TW	Terawatts
V_{OC}	Open-circuit voltage
XRD	X-ray diffraction

LIST OF ILLUSTRATIONS

Figure 1.1: Summary of the projected world energy demand predicted by the U.S. Energy Information Administration. 20
Figure 1.2: Estimated practically exploitable energy from various renewable energy sources. ... 21
Figure 1.3: Several representative conjugated polymers. 23
Figure 1.4: Device architectures of conjugated polymer-based PSCs: (a) single layer PSCs; (b) bilayer structured PSCs; (c) bulk heterojunction PSCs. 26
Figure 1.5: Micro/nano-structures exist on natural self-cleaning bio-surfaces: lotus leaf, cicada wings, and mosquito compound eyes. 32
Figure 1.6: (a) Contact angle of liquid droplet on a flat surface fulfils Young's equation. Two different wetting states exist when a liquid droplet sits on a rough surface: (b) Wenzel state and (c) Cassie state. (d) Schematic illustration of the self-cleaning mechanism when water rolls off a superhydrophobic surface. 33
Figure 1.7: (a) Atomic force microscopy (AFM) shows a high density of nanohair structures on the PET surface after anisotropic oxygen plasma etching. (b) Hydrophobilization of the nanostructured surface by CVD of semi-fluorosilanes (c) Photographs of water droplets on the transparent superhydrophobic PET substrate after surface hydrophobilization. 36
Figure 1.8: (a) Schematic illustration of the co-assembly of APTS-SiO_2 nanoparticles of different sizes. (b) SEM image of dual-sized APTS-SiO_2 nanoparticles successively dip coated onto Si wafers with 100 and 20 nm nanoparticles. (c) UV-Vis spectra of superhydrophobic nanoparticle films dip coated in different sequences and compared to bare glass. 38
Figure 1.9: (a) Sketch of the procedure undertaken to prepare transparent superhydrophobic surfaces. (b) TEM image taken after the PS core has been removed by calcination. (c) High resolution TEM image of two neighboring silica capsules connected by a silica bridge that formed during CVD of tetraethoxysilane. (d) Particles can't be removed by double sided tape after binding them chemically to the surface by silica bridges. 39
Figure 1.10: (a) Schematic illustration of the fabrication process flow for a nanostructured PSC with nanoimprinted DANs. (b) AFM image of the subsequently spin-coated PTB7-Th: $PC_{71}BM$ active layer on top of the nanoimprinted nanostructured ZnO layer. (c) Current density versus voltage (J–V) characteristics of PSCs in nanostructure and flat device configuration, recorded under 100 mW cm^{-2} AM 1.5G simulated solar illumination. (d) Absorption spectra of the devices with and without nanoimprinted DANs, and absorption enhancement. 42
Figure 2.1: (a) Schematic description of the preparation of superhydrophobic SiO_2-coated ZnO nanorod arrays on glass (PTES= perfluorodecyltriethoxysilane). (b) Transmittance spectra of ZnO seed layers of various thicknesses (c) Transmittance spectra of ZnO nanorod arrays grown on 5 nm ZnO seed layer with different growth times. Inset: SEM cross-section of ZnO nanorods obtained after 25 min. (d) Evolution of the static contact and sliding angles of PTES-treated ZnO nanorod arrays grown on 5 nm ZnO seed layer for various growth times. Inset: Photograph of a 2 μL water droplet placed on selected PTES-treated ZnO nanorod arrays. (e) Evolution of the

surface roughness (RMS) and average nanorod length (by SEM) in relation to the ZnO-nanorod growth time. 57
Figure 2.2: Enlarged transmittance spectra of ZnO nanorod arrays (non PTES-treated) grown on a 5 nm seed layer with different growth times. 58
Figure 2.3: (a) Cross-section SEM image of ZnO nanorod arrays grown on a 5 nm seed layer with a growth time of 25 min. (b) X-ray diffraction patterns of ZnO nanorods (grown for 25 min on a 5 nm seed layer) with various SiO_2 deposition times (non-PTES-treated). (c) Effect of the volume of water droplets on the sliding angle (PTES-treated ZnO nanorods, grown for 25 min, on a 5 nm seed layer). (d) AFM image (5x5 μm) of ZnO nanorods grown on a 5 nm seed layer with a growth time of 25 min (non PTES-treated). Note: Imaging of the actual topography of the nanostructured surface is limited by the aspect ratio of the cantilever, yet a relative RMS roughness can be inferred from the measurement. 59
Figure 2.4: Transmittance spectra of SiO_2-coated ZnO nanorods (grown for 25 min on a 5 nm ZnO seed layer) for various SiO_2 deposition times. Inset: TEM image of SiO_2-coated ZnO obtained after 3h of SiO_2 deposition. (b) SEM image (top-view) of the SiO_2-coated ZnO obtained after 6h of SiO_2 deposition. (c) Evolution of contact angles and surface roughness (RMS) in PTES-treated SiO_2-coated ZnO nanorod arrays (grown for 25 min on 5 nm ZnO seed layer) for various SiO_2 deposition times: static contact angle, sliding angle, surface roughness. (d) Evolution of contact angles on PTES-treated SiO_2-coated ZnO nanorod arrays with UV irradiation time (365 nm, ~ 2 mW cm^{-2}) (e) SEM image of the SiO_2/ZnO nanocomposite surface after application and subsequent removal of a scotch tape pressed at 10 kPa for 1 min: the adhesive (dark region) peels off and remains bound to the nanostructured coating. (f) Magnified SEM image showing that the integrity of the nanorod arrays is retained under the bound adhesive (darker regions). 61
Figure 2.5: TEM image of ZnO nanorods (grown for 25min, on a 5nm seed layer) with SiO_2 deposition times of a) 3h, b) 6h, c) Energy-dispersive X-ray spectroscopy (EDX) spectrum of ZnO nanorods obtained after a SiO_2 deposition time of 6h. 63
Figure 2.6: Reflectance spectra of SiO_2-coated ZnO nanorods (grown for 25 min on a 5 nm ZnO seed layer) for various SiO_2 deposition times (non-PTES-treated). 64
Figure 2.7: a) SEM image (top-view) of ZnO nanorods (grown for 25 min, on a 5 nm seed layer) obtained after a SiO_2 deposition time of 3h. b) Cross-section SEM image of ZnO nanorods (grown for 25 min, on a 5 nm seed layer) with SiO_2 deposition time of 3h, and c) 9h. 65
Figure 2.8: (a) Sketch of the setup used to perform water drop and sand bursting test. (b) SEM image of the surface after sand bursting test shows collapsed SiO_2-coated ZnO nanorods. 66
Figure 2.9: (a) Schematic of a BHJ polymer solar cell including the SiO_2/ZnO nanocomposite. (b) Water droplets positioned on the front of the superhydrophobic device remain perfectly spherical. (c) *J*-V characteristic of a superhydrophobic (SH) cell superimposed on that of a bare reference (Ref.) cell; AM 1.5G solar illumination (100 mW cm^{-2}). (d) EQE spectra of the SH cell and the Ref. Cell. (e) Water droplets positioned on a bare transparent sheet of PET (2x2”). (f) Droplets positioned on superhydrophobic PET (static angle: 160°). (g) PET retains its superhydrophobicity upon repeated bending (>200 times). 69

Figure 3.1: (a) Schematic illustration of the stepwise process of forming hollow silica half-nanospheres via the BF approach on PTCS-modified glass substrates (PTCS = perfluorooctyltrichlorosilane, TEOS = tetraethyl orthosilicate). (b) SEM image of a PTCS-modified glass substrate subsequently subjected to a post-deposition cleaning process (see Experimental Section), before exposure to an atmosphere saturated with water, ammonia (from a 20% w/v ammonium hydroxide aqueous solution) and TEOS vapors (3 h, room temperature, under *ca.* 100 Torr): the substrate is not amenable to the development of nanostructured patterns via the BF approach. (c) SEM image of an "as-cast" PTCS-modified glass (presence of PTCS aggregates) after exposure to the same TEOS precursor under the same conditions: arrays of silica "nanodomes" can be observed across the substrate. Inset: Magnified cross-sectional SEM image of one of the silica "nanodomes", emphasizing the hollow nature of the nanostructures. 84
Figure 3.2: AFM images (1x1 µm) of (a) PTCS-modified glass after extended sonication in ethanol (1 h), (b) "as-cast" PTCS-modified glass composed of a continuous and dense pattern of PTCS aggregates (pattern obtained after 1 h of vapor deposition of PTCS at 90°C under a pressure of *ca.* 130 Torr), (c) "as-cast" PTCS-modified glass with aggregates formed on a hydrated glass substrate, (d) "as-cast" PTCS-modified glass with aggregates formed on a dehydrated glass substrate, and (e) three-dimensional AFM image (1x1 µm) of the "as-cast" PTCS-modified glass with aggregates formed on a dehydrated glass substrate. 86
Figure 3.3: (a) AFM image (3x3 µm) of "as-cast" PTCS-modified glass composed of a continuous and dense pattern of PTCS aggregates formed on a dehydrated glass substrate (pattern obtained after 1 h of vapor deposition of PTCS at 90°C under a pressure of ca. 130 Torr); Scale bar: 600 nm. (b-d) AFM images (1x1 µm) of various PTCS-modified substrates (patterns obtained after 1 h of vapor deposition of PTCS at 90°C under a pressure of ca. 130 Torr): (b) fused silica, (c) silicon substrate with ca. 200 nm thermally growth oxidized layer, (d) borosilicate glass substrate. 87
Figure 3.4: AFM images (1x1 µm) of distinct patterns of PTCS aggregates obtained on a dehydrated glass substrate after (a) 5 min, (b) 10 min, or (c) 30 min of vapor deposition of PTCS at 90°C under a reduced pressure of ca. 130 Torr. (d) Height histograms associated with PTCS vapor-deposition steps of 30 min and 1 h at 90°C..... 89
Figure 3.5: AFM images (1x1 µm) of distinct patterns of PTCS aggregates obtained on a dehydrated glass substrate after 1 h of vapor deposition of PTCS at (a) 30°C, (b) 60°C, and (c) 120°C under a reduced pressure of ca. 130 Torr. (d) Height histograms associated with PTCS vapor-deposition steps of 1 h at various temperatures ranging from 30°C to 120°C, in 30°C steps. 91
Figure 3.6: (a) SEM image of an array of hollow silica half-nanospheres formed on a dehydrated and PTCS-modified glass substrate (deposited at 120°C for 1 h, under ca. 130 Torr) upon 3 h exposure (room temperature, under ca. 100 Torr) to an atmosphere saturated in water, ammonia (from a 20% w/v ammonium hydroxide aqueous solution) and TEOS vapors, resulting in the hydrolysis of the TEOS precursor and in the formation of a thin shell of silica (SiO_2) around individual water droplets. (b) Cross-sectional SEM image of the same array of hollow silica half-nanospheres. (c) TEM image of the hollow silica half-nanospheres lifted off of the PTCS-modified glass substrate. (d) SEM image of an array of hollow silica half-nanospheres formed on PTCS-

modified glass substrate prepared following the same protocol as described in (a) and subjected to TEOS hydrolysis for only 1 h (20% w/v ammonium hydroxide solution, room temperature, under ca. 100 Torr). 94
Figure 3.7: Area distribution map of silica half-nanospheres formed on a dehydrated and PTCS-modified glass substrate (deposited at 120°C for 1 h, under ca. 130 Torr) upon a 3 h exposure (room temperature, under ca. 100 Torr) to an atmosphere saturated in water, ammonia (from a 20% w/v ammonium hydroxide aqueous solution) and TEOS vapors. 95
Figure 3.8: SEM images of several arrays of hollow silica half-nanospheres formed on dehydrated and PTCS-modified glass substrates and upon various TEOS hydrolysis conditions: (a) PTCS-modified glass: 1 h PTCS deposition at 30°C and under ca. 130 Torr / TEOS hydrolysis step: 3 h exposure (room temperature, under ca. 100 Torr) to an atmosphere saturated in water, ammonia (20% w/v ammonium hydroxide solution) and TEOS vapors. (b) PTCS-modified glass: 1 h PTCS deposition at 30°C and under ca. 130 Torr / TEOS hydrolysis step: 6 h exposure (room temperature, under ca. 100 Torr) to an atmosphere saturated in water, ammonia (diluted ammonium solution: 2.5%) and TEOS vapors. (c) PTCS-modified glass: 1 h PTCS deposition at 120°C and under ca. 130 Torr / TEOS hydrolysis step: 6 h exposure (room temperature, under ca. 100 Torr) to an atmosphere saturated in water, ammonia (diluted ammonium hydroxide solution: 2.5%) and TEOS vapors. (d) UV-Vis-NIR transmittance spectra of selected PTCS-modified and nanostructured glass substrates. 97
Figure 3.9: SEM images of several arrays of hollow silica half-nanospheres formed on dehydrated and PTCS-modified glass substrates and upon various TEOS hydrolysis conditions: (a) PTCS-modified glass: 1 h PTCS deposition at 60°C and under ca. 130 Torr / TEOS hydrolysis step: 3 h exposure (room temperature, under ca. 100 Torr) to an atmosphere saturated in water, ammonia (20% w/v ammonium hydroxide solution) and TEOS vapors. (b) PTCS-modified glass: 1 h PTCS deposition at 90°C and under ca. 130 Torr / TEOS hydrolysis step: 3 h exposure (room temperature, under ca. 100 Torr) to an atmosphere saturated in water, ammonia (20% w/v ammonium hydroxide solution) and TEOS vapors. (c) PTCS-modified glass: 1 h PTCS deposition at 60°C and under ca. 130 Torr / TEOS hydrolysis step: 6 h exposure (room temperature, under ca. 100 Torr) to an atmosphere saturated in water, ammonia (diluted ammonium hydroxide solution: 2.5%) and TEOS vapors. (d) PTCS-modified glass: 1 h PTCS deposition at 90°C and under ca. 130 Torr / TEOS hydrolysis step: 6 h exposure (room temperature, under ca. 100 Torr) to an atmosphere saturated in water, ammonia (diluted ammonium hydroxide solution: 2.5%) and TEOS vapors. 98
Figure 3.10: (a) SEM image of hollow silica half-nanosphere attached with 40 nm silica nanoparticles. (b) Photo of water droplet positioned on the transparent superhydrophobic surface. (c) Load force recorded during the nanoindentation process and fitted with Hertz model. (d) Deformation formed on the half-nanosphere. 101
Figure 3.11: SEM image of an assembly of hollow silica half-nanospheres formed on a superhydrophobic array of perfluorodecyltriethoxysilane (PTES)-modified ZnO nanorods. Inset: Magnified cross-sectional SEM image of one of the apparent silica “nanodomes”, emphasizing the hollow nature of the nanostructures. 103

Figure 4.1: (a) Molecular structures of the polymer donor PBDTTPD and the fullerene acceptor $PC_{71}BM$ used in the multi-junction PSC devices. (b) Schematic homo-tandem device architecture. (c) Schematic triple-junction device architecture. (d) Simplified energy diagram of the homo-tandem PSC device architecture. 114
Figure 4.2: Single-junction PBDTTPD:$PC_{71}BM$ device performance with different active layer thicknesses: (a) *J*-V curves; (b) absorption spectra of the active layers; (c) external quantum efficiency (EQE); and (d) calculated internal quantum efficiency (IQE)..... 115
Figure 4.3: (a) Integrated photocurrent for AM1.5G irradiation from 300 nm to 680 nm by assuming a 100% EQE device. (b) Simulated short current vs. active layer thickness by assuming a 100% IQE device. The waveform of the curve illustrates the strong interference effect inside the active layer..... 117
Figure 4.4: External quantum efficiency and corresponding integrated photocurrent for a single junction PBDTTPD:$PC_{71}BM$ device with active layer in thicknesses of (a) 90 nm, (b) 150 nm and (c) 200 nm. 119
Figure 4.5: (a) Power conversion efficiency (PCE) of homo-tandem PSCs predicted from optical and electrical modeling. (b) *J*-V curves of optimized single-junction and homo-tandem PSCs superimposed with that predicted from optical and electrical modeling for the homo-tandem device with an optimized subcell thickness combination (70-nm front cell, and a 120-nm back cell). (c) Absorption of a single-junction PSC device with 70-nm and 120-nm active layers, a control single-junction PSC device with an “unrealistically” thick active layer of 1,000 nm (simulated via transfer matrix modeling), and an optimized homo-tandem solar cell with a 70-nm front cell and a 120-nm back cell. (d) EQE of single-junction devices with 70-nm and 120-nm active layers along with their calculated “total EQEs” for the optimized tandem device inferred from the spectral absorption and IQE of the combined subcells. 121
Figure 4.6: Predicted figures of merit for a PBDTTPD:$PC_{71}BM$ homo-tandem solar cell from combined optical and electrical modeling (a) V_{OC}, (b) FF and (c) J_{SC}..... 122
Figure 4.7: Transmission, reflection and absorption spectra measured by UV-Vis spectrometer for a 68-nm PBDTTPD:$PC_{71}BM$ photoactive layer spin-coated on glass. Transmission, reflection and absorption spectra obtained from transfer-matrix modeling are also present to show the consistency between experimental and modeling results. 124
Figure 4.8: Statistical PV performance for single-junction, tandem and triple-junction PBDTTPD devices. For each result, the markers denote the average values and the error bars show the standard deviation across 10 devices. 127
Figure 4.9: (a) PCE of triple-junction PSCs predicted from combined optical and electrical modeling. (b) *J*-V curves of constructed and model predicted triple-junction PSC with an optimized thickness combination (50-nm front cell, a 65-nm middle cell and a 120-nm back cell). 130
Figure 4.10: Predicted figures of merit for a PBDTTPD:$PC_{71}BM$ triple-junction solar cell from combined optical and electrical modeling (a) V_{OC}, (b) FF and (c) J_{SC}..... 131
Figure 4.11: (a) Overall I-V characteristics of water splitting in the two-electrode cell configuration used in this study for demonstration; a platinum wire and nickel foam are used as

cathode and anode for water electrolysis, respectively, with a 1 M NaOH solution as the electrolyte. (b) *J*-V curves of the homo-tandem solar cell measured using a water electrolysis cell with different surface area ratios of the solar cell and the water splitting electrodes using a source measurement unit. 132
Figure 4.12: (a) Schematic PV-driven electrochemical water splitting study. (b) PCE of the homo-tandem PSC (measured via source-measurement unit) and estimated solar-to-hydrogen conversion efficiency (η) at various operating voltages. 133
Figure 5.1: (a) Chemical structure of used materials, including a PbS quantum dot after ligand exchange, conjugated polymer donor PBDTTPD and $PC_{71}BM$ as the fullerene acceptor. (b) Optical density of PbS CQD film and PBDTTPD: $PC_{71}BM$ active layers 143
Figure 5.2: Schematic device structure for (a) bottom-illuminated conventional hybrid tandem and (b) bottom-illuminated inverted hybrid tandem. *J*-V characteristic curves of the optimized hybrid tandem devices and single-junction devices for (c) bottom-illuminated conventional hybrid tandem and (d) bottom-illuminated inverted hybrid tandem. 145
Figure 5.3: (a) Schematic description of the utilized transparent conductive electrode structure. (b) Transmittance and sheet resistance for the transparent conductive electrode with varied Ag thickness. SEM image of 7 nm Ag film deposited on MoO_x (c) without insertion of 1 nm Au and (d) with insertion of 1 nm Au. 149
Figure 5.4: Schematic device structure for top-illuminated conventional hybrid tandem. (b) *J*-V characteristic curves of the optimized top-illuminated conventional hybrid tandem devices and single-junction devices. (c) Schematic device structure for top-illuminated inverted hybrid tandem. (d) *J*-V characteristic curves of the preliminary constructed top-illuminated conventional hybrid tandem devices with different sized CQDs and single-junction devices. ... 151
Figure 6.1: Schematic illustration for spatial control of the position of the hollow half-nanospheres on the surface. 162
Figure 6.2: Schematic illustration of the fabrication process flow for a nanostructured PSC by using hollow half-nanosphere structure as template. 163
Figure 6.3: Schematic illustration of the light trapping mechanism in nanostructured PSCs. 164

LIST OF TABLES

Table 2-1: Summarized static water contact angle and sliding angle for PTES-treated SiO_2-coated ZnO nanorod arrays before and after the water drop test. 67
Table 2-2: Summarized static water contact angle and sliding angle for PTES-treated SiO_2-coated ZnO nanorod arrays before and after the sand bursting test. 68
Table 4-1: Single-junction PBDTTPD:$PC_{71}BM$ device performance with different active layer thicknesses. 116
Table 4-2: PV performance figures for the constructed and predicted (via combined optical and electrical modeling) homo-tandem and triple-junction PSCs with optimized subcell thickness combinations. 125
Table 5-1: Summarized figures of merit for bottom-illuminated conventional and inverted hybrid tandem device, along with the performance of single-junction devices. 147
Table 5-2: Summarized figures of merit for top-illuminated conventional hybrid tandem device, along with the performance of single-junction devices. 152
Table 5-3: Summarized figures of merit for top-illuminated conventional hybrid tandem device with different size of CQDs, along with the performance of single-junction devices. 153
Table 6-1: Various metal oxides achievable by low-temperature atomic layer deposition (ALD) with volatile metalorganics as precursor and H_2O as reactant. 159

Chapter 1

Introduction and Motivation

1.1 World Power Demand

Due to pressures of population increase and rapid economic development, the world energy demand is projected to more than double by 2050 according to empirical predictions of the U.S. Energy Information Administration (Figure 1.1). They calculate a continuous power consumption of 30 terawatts (TW) even with aggressive conservation and energy efficiency measures.[1-2] More than 85 percent of the increase in global energy demand occurs among the developing nations outside the Organization for Economic Cooperation and Development, known as non-OECD. Finding sufficient energy supplies to fulfill the ~ 14 TW energy gap by 2050 is one of society's most daunting challenges.

Owing to limited reserves and serious harmful environmental effects, fossil fuels including liquid fuels, natural gas and coal are not suitable as a long-term energy source, even though they currently account for 80 percent of the world energy. The other conceptually viable option, nuclear power, confronts a similar situation as fossil fuels. The terrestrial uranium resource base for nuclear power would be exhausted in 10 years assuming an equivalent consumption speed to fulfil the energy gap.

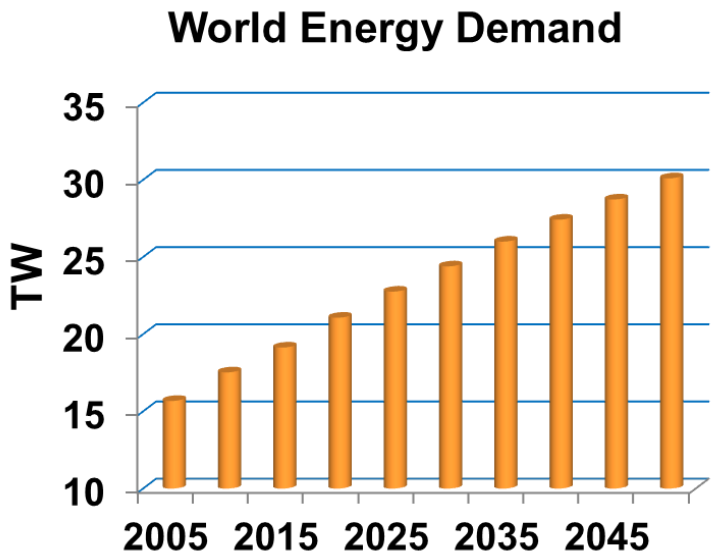

Figure 1.1: Summary of the projected world energy demand predicted by the U.S. Energy Information Administration.[1]

Among the renewable energy sources, most yield a limited amount of practically exploitable energy (Figure 1.2). For example, traditional sources of renewal energy (hydroelectric, wind, geothermal) can only contribute an estimated of 2-12 TW of energy.

On the other hand, solar energy can contribute a significant impressive 600 TW of potentially exploitable energy. Solar energy is, by far, the largest renewable source that exists on Earth. A massive amount of solar energy, equivalent to 120,000 TW, is delivered from the Sun to the Earth's surface. If the solar energy can be efficiently harvest, the world energy demand can be far more satisfied, even in the most aggressive energy demand scenarios.[3] Therefore, photovoltaic technology is regarded as one of the most promising strategies which can fulfill the long-term energy needs by itself.

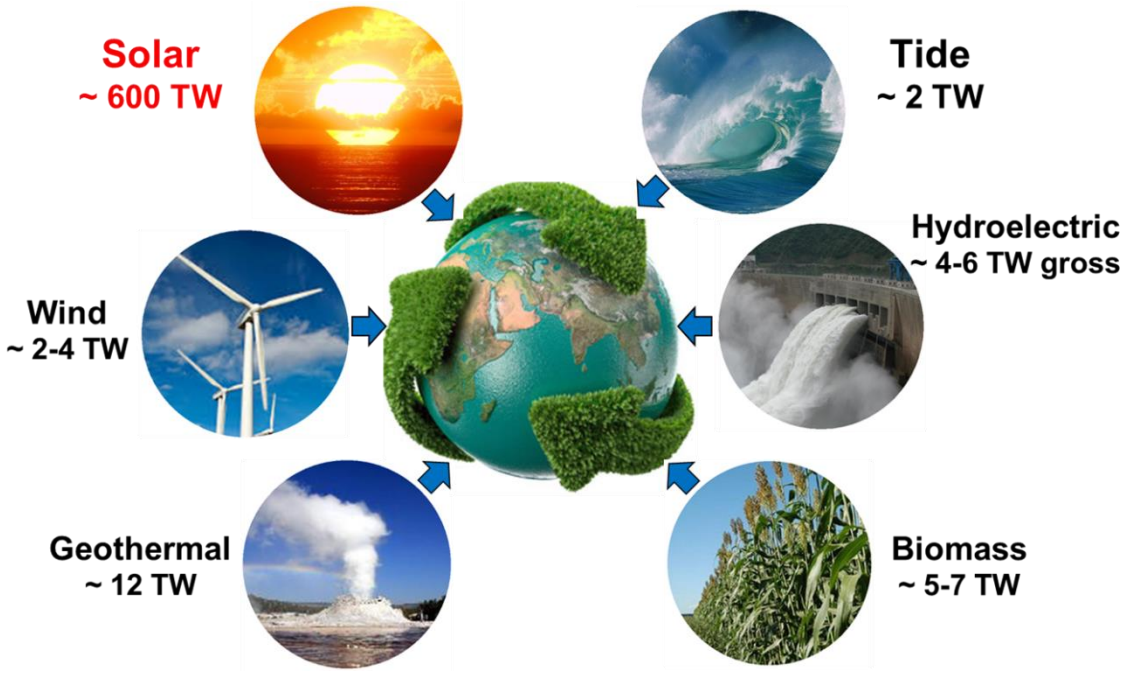

Figure 1.2: Estimated practically exploitable energy from various renewable energy sources.

However, due to the high production cost and low production capacity of the first generation photovoltaics based on thick crystalline semiconductors, photovoltaic technology cannot currently compete with primary fossil energy cost-wise. It also cannot currently bridge the 14 TW energy gap within the next 35 years,[4] as illustrated by the following. Take the average power conversion efficiency (PCE) of 15% for commercialized solar panel. Assuming a global average solar irradiation of 6,000 W*hr m^{-2} day^{-1} (the solar irradiance in Jeddah, Saudi Arabia),[5] a production speed of ~ 338 m^2 s^{-1} is required to fulfil the 14 TW energy gap. However, the annual global production power of a photovoltaic module is ~ 40 gigawatt (GW) in 2014,[6] equivalent to a production speed of 33.8 m^2 s^{-1}, which is at least one order of magnitude less than the required production speed. With the aim of bringing down production costs and

dramatically improving production capacity, photovoltaic technologies based on solution-processable photovoltaic materials, such as organic dyes, organic semiconductors, and quantum dot absorbers, have attracted considerable attention in recent years. Due to the solution-processability of these materials, the economically high throughput roll-to-roll printing process can be implemented to boost the production capacity and reduce the production cost of the photovoltaic module.

1.2 Polymer Solar Cell

The discovery of tunable electrical conductivity in doped conjugated polymer in the 1970s paved the way for constructing cheap semiconductors from polymeric materials.[7-8] With the demonstration of the photovoltaic effect in polymer solar cells (PSCs) by using cheap polymer semiconductor as functional material to harvest light energy, PSCs have emerged as a promising candidate for photovoltaic technology. Due to their light-weight, mechanical flexibility, solution processability, and large-area cost-efficient manufacture compatibility,[9-12] PSCs have garnered increasing attention in the last two decades. Hence, it is no surprise that power conversion efficiencies of single junction PSCs have reached up to 11%.[13]

1.2.1 Properties of Conjugated Polymer

Conjugated polymers are organic macromolecules that are characterized by a backbone chain of alternating single and double bonds. Several representative conjugated polymers are shown in Figure 1.3. In the simplest case, this characteristic alternated single and double bonding configuration leads to a linear chain of sp^2 hybridized carbon

atoms with overlapped π-orbitals. The delocalized π-electrons arise from the overlapping of π-orbitals form a conduction band, and are expected to give rise to metallic behavior in conjugated polymers. However, many attempts to construct conductive polymers with this extended conjugated π-electron system failed in early years.[14-16] Either bond alternation or electron correlation induce a large band gap which forbids thermal excitation of carriers across the band gap at room temperature, resulting in low observed conductivities.[17-18]

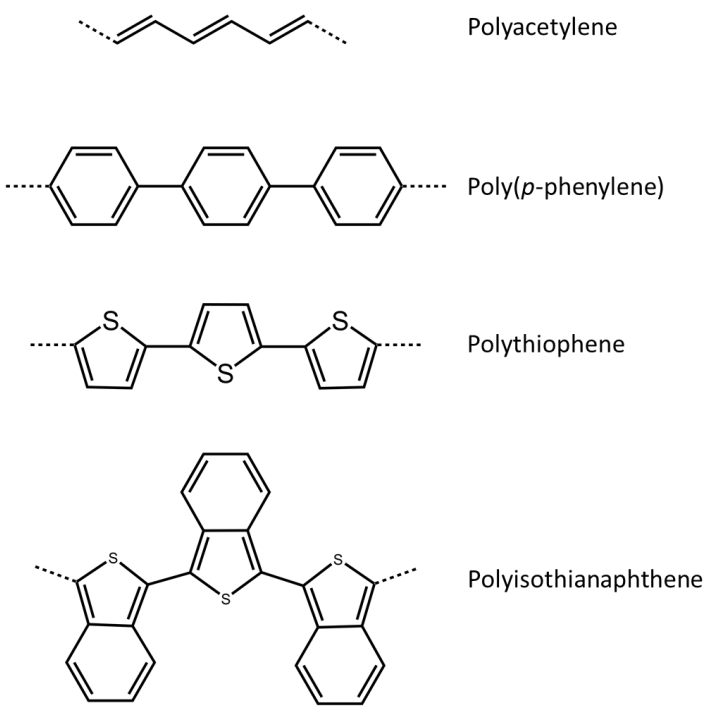

Figure 1.3: Several representative conjugated polymers.

Enhanced electrical conductivity of conjugated polymer was first discovered in halogen doped polyacetylene in the 1970s.[7-8] By controlling the nature and concentration of the dopant species, polyacetylene can be chemically doped to n-type and p-type by using

electron-donating (donor) or electron-accepting (acceptor) dopants. In this way, the electrical conductivity of polyacetylene can be controlled and varied over a range of more than eleven orders of magnitude. Electrical conductivity as high as 560 Ω^{-1} cm^{-1} has been achieved in AsF_5 doped polyacetylene.[7-8, 19-20] The ability to control electrical properties in conjugated polymer can enable it to perform as an insulator, a semiconductor or a metal. This recognition led to a sudden spurt in research, especially related to polymer semiconductors. Consequently, a significant amount of effort was made to explain the underlying charge-carrier transport mechanism, and numerous types of conductive conjugated polymers were invented to overcome the air instability problem of polyacetylene and to explore the limitation of these organic semiconductors.[21-40] It turns out that the formation of defect states induced by charge transfer between polymer and dopant species is responsible for the enhanced electrical conductivity in doped conjugated polymers. Different from the rigid periodic structures formed in inorganic semiconductors by covalently bonded atoms with multi-coordinates, the two-fold coordination of bonding motifs present in conjugated polymers is generally more susceptible to structural distortion. As a result, instead of exciting charge carriers in terms of electrons and holes as the case in traditional inorganic semiconductors, 'electronic' excitations in conjugated polymers always accompanied structural distortions near the excited charge carriers. These are collectively known as a polaron. Therefore, the charge transport in conjugated polymer is a process that not only involves the movement of charge carriers, but also involves moving the structural distortion together with the charge carrier. Consequently, the

charge transport in conjugated polymers is much lower than that in inorganic semiconductors due to the extra energy required to move structural distortion as the polaron moves along the backbone, hopping between polymer chains. This charge transport behavior imparts the limited conductivity in pure conjugated polymer. As more polarons are created through charge transfer between polymer and dopant species arising from the doping process, the conductivity of doped conjugated polymers is enhanced. In this context, an electron refers to a negatively charged polaron and a hole refers to a positively charged polaron.

In contrast to traditional inorganic semiconductors, polymer semiconductors have the advantage of optical and electronic tunability through molecular engineering. By choosing specific building blocks for the backbone and substituent groups, the delocalization of π-electrons can be tailored, imparting conjugated polymers with a desired energy band gap and energy level.[41] This was a major reason for the rapid growth of this active field.

1.2.2 Device Architectures

In order to convert light energy into electrical energy, the light absorbing material is required to have separated excited and ground states. The energy gap between the two separated states should be larger than k_BT, where k_B is the Boltzmann's constant and T is temperature. In this way, the excited charge carriers formed upon photon absorption can be maintained at a higher electrochemical energy for a long time. Hence, before decaying back to ground state, they can be selectively collected at corresponding

electrodes through asymmetric electronic configurations, converting the photon energy to electrical energy. Therefore, undoped and lightly doped conjugated polymers which possess semiconducting properties are able to act as functional photovoltaic materials to construct PSCs.

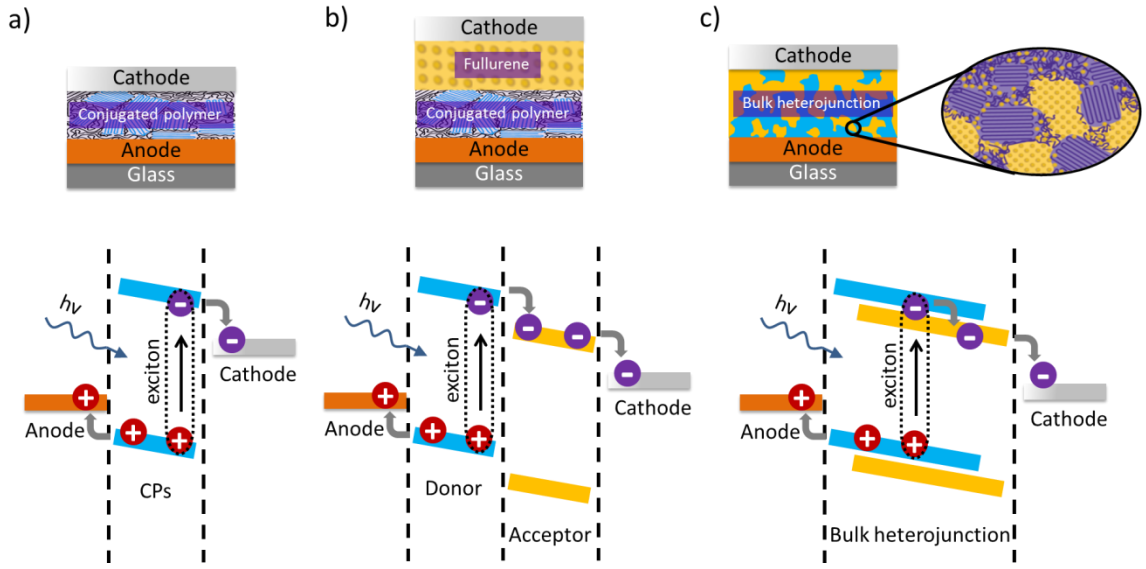

Figure 1.4: Device architectures of conjugated polymer-based PSCs: (a) single layer PSCs; (b) bilayer structured PSCs; (c) bulk heterojunction PSCs.

However, the single layer PSC developed in early years, in which a single layer of conjugated polymer is sandwiched between two electrodes with different work functions (Figure 1.4a), gave extremely poor device performance with a low photocurrent, even though clear photovoltaic phenomenon and reasonable open voltage are observed.[42-44] This was due to the intrinsic low dielectric constant of conjugated polymers (~ 3-5), and the large binding energy (~ 0.3 eV) of the exciton formed upon photon absorption.[44] In fact, the binding energy is much larger than the thermal energy or the present built-in electric field arising from the different work

functions of the electrodes. Hence, rather than spontaneously dissociate into free carriers, as is the case in inorganic semiconductors, the exciton excited in conjugated polymer is much more likely to recombine after a certain length of diffusion within the polymer.[45] Combined with the much lower electron mobility in most conjugated polymers, only a few excitons formed near the electron-collecting electrode can be dissociated and collected, resulting in a single layer PSC to produce very little current.

A breakthrough happened when it is found that an exciton can go through efficient dissociation at heterojunction interfaces formed by organic semiconductors with offset energy bands. The band offset present at the organic semiconductor interface could provide enough energy to overcome the considerably large exciton binding energy.[46] As expected, bilayer structured PSCs, for example, in which a heterojunction formed by two layers of organic semiconductor sandwiched between two electrodes with different work functions (Figure 1.4b), show improved photocurrent than that of a single layer PSC.[47] Here, instead of using all conjugated polymers to construct the junction, a combination of conjugated polymer with fullerene or its derivatives is used due to the high electron mobility and large electron affinity of the fullerene.[48] In a bilayer structured PSC, an exciton that diffuses to the heterojunction interface before recombining can be efficiently dissociated, resulting in oppositely charged free carriers at each side. Once the dissociation of exciton is achieved, the resulting free carriers can be collected at corresponding electrodes via drift, driven by the built-in electric potential formed by the two electrodes with different work functions. However, the

performance of bilayer structured PSC still shows limited device performance, unsuitable for practical application. This low device performance arises from the extremely short exciton diffusion length inherent in the polymer semiconductors. Limited by the significant structural disorder and a short intrinsic exciton lifetime, the exciton diffusion length in most conjugated polymer is typically on the order of 5-10 nm,[49] which is much shorter than the absorption length of the material (~ 100 nm). For this reason, only the excitons formed within 10 nm away from the heterojunction can diffuse to the interface before decaying back to the ground state, and being split to form free charge carriers which contribute to the photocurrent. Therefore, the effective thickness of the semiconductor layer is geometrically constrained by the short exciton diffusion length. Ultimately, the limited efficiency of bilayer structured polymer solar cells is a result of the mismatch between the short exciton diffusion length and the thick absorption length in films of conjugated polymers.

As both exciton diffusion length and absorption length arises from the intrinsic properties of conjugated polymer, the mismatch between these two lengths can only be solved from the geometric perspective of the device. Therefore, a new concept of device structure, bulk heterojunction device structure (Figure 1.4c), was proposed to solve the conflict between the short exciton diffusion length and the thick absorption length.[50-52] The bulk heterojunction structure is formed by casting a single solution prepared by blending polymer and fullerene together. During the drying process of the casted solution, the donor and acceptor components would demix with each other due

to the difference in solubility and chemical potential. Ideally, each component can form a continuous network during the spontaneous phase separation process, interpenetrating each other on the nanoscale. This would result in pure donor and acceptor domains co-existing alongside domains of blended donor and acceptor molecules. Because the phase separation induced interpenetration network can be tuned to have a nanomorphology with extensive domains on the order of 10-20 nm (comparable to the exciton diffusion length), almost all of the excitons formed in the active layer have the ability to diffuse to the closest heterojunction interface to produce current. Primarily due to this property, the bulk heterojunction device structure is the most popular adopted device structure in PSCs, and results in pronounced improvement in device performance. However, finding the right processing conditions for a specific polymer system to achieve the optimum bulk heterojunction morphology on the scale of exciton diffusion length is a challenging task. Study of the blend morphology with a variety of microscopic, spectroscopic, and X-ray scattering techniques has shown that the blend morphology can be influenced by the choice of processing solvent,[53] addition of processing additives,[54] drying time,[55] solute concentration, or subsequent thermal[56] and solvent vapor annealing[57] process. Until now, no robust and universal strategy has been demonstrated to give the right bulk heterojunction morphology in PSCs.

1.2.3 Challenges and Motivation

With significant advances in exploiting new materials,[41, 58-59] optimization of BHJ morphology,[60] light management and improvement in interface characteristics,[61-66] the

PCEs of single junction PSCs have approached 11%,[13] the milestone efficiency for commercialization. As this record number is quite close to the average PCE of 15% for commercialized inorganic photovoltaic modules, it could be possible that commercialization of PSCs would soon become a reality. However, the bankruptcy of Konarka Technology, Inc. in late May 2012 after raising $170 million from investors, released a somber message to the PSC research and development community: high PCE numbers are not sufficient for the commercialization of PSCs. Instead of pursuing the highest PCE numbers in PSCs, there are still serious issues that impede the path towards commercialization for PSCs. Some of these are short life time, intrinsic intermittent power supply,[67] high maintenance cost due to dust accumulation,[68-69] and relatively high production cost.[70] Addressing these issues to pave the way for the commercialization of PSCs is as important as pursuing higher PCE numbers, considering the efficiencies of PSCs are becoming contestable with inorganic PSCs. Addressing these issues is quite challenging and would require significant interdisciplinary work. This dissertation aims to tackle some of these issues by focusing on the application of nanostructured materials and multi-junction structure to PSCs as a way to reduce maintenance and production costs.

1.3 Application of Nanostructured Materials to PSCs

In the broadest sense, nanostructured materials show structural features with sizes in the range of 1 nm to a few hundred nanometers in at least one dimension. Novel physical and chemical properties arise from their high surface to volume ratio and nano-

scale confined dimensions. The mechanical, electrical, and optical properties of the material can be manipulated, which has resulted in tremendous innovative applications. With regards to PSCs, implementation of the unique properties of nanostructured materials may shine a light on how to solve some of their practical problems.

1.3.1 Self-Cleaning PSCs

After the installation of solar panels, accumulation of dust, pollution, and animal matter on the surface can seriously block sunlight and cause a dramatic decrease in efficiency of the solar cell. A decrease of ~ 17.4%/month in the output power have been reported in sandy areas and more than 2.3%/month in rainy ones.[68-69] To keep the output power of solar cells at a constant level, extensive labor work needs to be done to clean the surface of solar panels, which further increase the cost of solar energy. Interestingly, many bio-surfaces exist in nature on plants and insects that have admirable self-cleaning abilities that keep them clean even under extreme environmental conditions. Hence, implementing the self-cleaning strategies of bio-surfaces on solar panels is an extremely attractive, but potentially challenging proposition.

1.3.1.1 The Self-Cleaning Surface

The unique micro/nano-structures shown in those bio self-cleaning surfaces are believed to be one of the key factors that impart the self-cleaning ability (Figure 1.5). These structures induce a large water contact angle with a small sliding angle, so that surface contaminants can be flushed away as water rolling over on the surface. (Figure 1.6d).[71-74] Liquid wettability on micro/nano-structured surfaces has been studied well

before the mystery of self-cleaning bio-surfaces was revealed, and two different states were found depending on whether the liquid penetrates the underlying structure or not.[75-76]

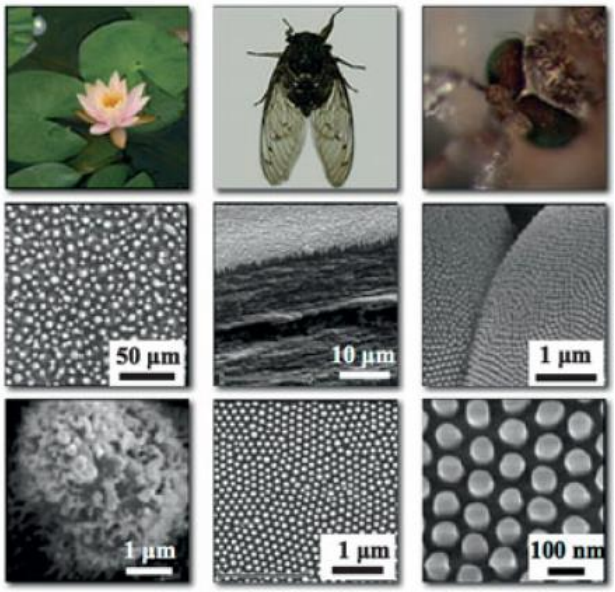

Figure 1.5: Micro/nano-structures exist on natural self-cleaning bio-surfaces: lotus leaf, cicada wings, and mosquito compound eyes (from left to right).[74]

When a liquid drop is deposited on a flat surface (Figure 1.6a), in order to minimize the Gibbs free energy of the system, the contact angle (θ_e) of the liquid drop follows Young's equation[77]:

$$\cos(\theta_e) = \frac{\gamma_{sv} - \gamma_{sl}}{\gamma_{lv}} \quad (1)$$

, where γ_{sv} is the solid-vapor interfacial energy, γ_{sl} is the solid-liquid interfacial energy, and γ_{lv} is the liquid-vapor interfacial energy.

On a rough surface, if the liquid totally wets the underlying rough structure (Figure 1.6b), it is referred to being in the Wenzel state. Since there are more liquid-solid

interfacial contacts present compared to the situation when the liquid sits on a flat surface, the apparent contact angle, θ_r^w, can be expressed as shown in equation (2):

$$\cos\theta_r^w = r\cos\theta_e \quad (2)$$

, where r is the ratio of the actual liquid-solid contact area to the projected area on the horizontal plane.

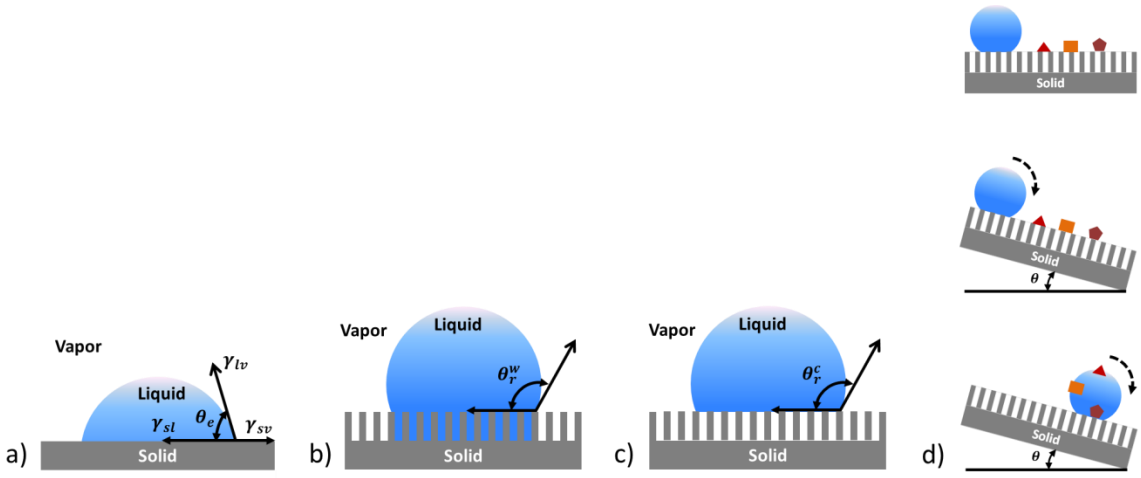

Figure 1.6: (a) Contact angle of liquid droplet on a flat surface fulfils Young's equation. Two different wetting states exist when a liquid droplet sits on a rough surface: (b) Wenzel state and (c) Cassie state. (d) Schematic illustration of the self-cleaning mechanism when water rolls off a superhydrophobic surface.

When a liquid droplet sits on top of the rough structure without penetrating the underlying rough structure (Figure 1.6c), it is known to be in the Cassie state. As air is trapped at the interface, the apparent contact angle, θ_r^c, can be expressed per equation (3):

$$\cos\theta_r^c = f\cos\theta_e + f - 1 \quad (3)$$

, where f is the projected surface fraction of solid at contact interface.

It can be noted that depending on the texture design of the rough surface, both Wenzel and Cassie state can impart a very high liquid contact angle for a micro/nano-structured surface composed by liquid-repelling material ($\theta_e > 90^\circ$). However, due to the difference in liquid-solid contact area, Wenzel and Cassie states are different in their adhesion behavior. Only in the Cassie state, it is possible to have a surface with minimum interaction with the deposited liquid droplet, so that a tiny gravity force induced by the small angle tilting enables roll-off of the liquid droplet, and removes the contaminants deposited on the surface (Figure 1.6d). Actually, just playing with the texture design of the rough surface by introducing so called “reentrant” or “doubly reentrant” structures, an ultra-liquid-repellent surface can be realized for an extremely low surface tension liquid ($\sigma_{lv} < 15\ mJ\ m^{-2}$) irrespective of the wettability of the composed surface materials, which further highlights the importance of micro/nano-structures to self-cleaning surfaces.[78-80] By applying an external force on the liquid droplet deposited on the rough surface, irreversible and reversible transitions[81-83] between the two states can be observed, which suggest that both Wenzel and Cassie states might co-exist, represents the corresponding local free energy minima of the system. It turns out that in which state the deposited liquid droplet sits, is not only a consideration of thermodynamics, but also a perspective of kinetics.[78-80, 84-86] To design a self-cleaning surface which is both thermodynamically and kinetically robust to support the liquid droplet in the Cassie state is critical for practical self-cleaning applications.

Since water has a relatively high surface tension, superhydrophobic surfaces which shows high apparent water contact angle (>150°) and low sliding angle (<10°) are easy to be realized on various kinds of surfaces.[87-95] And, also, because water falls as rain in every part of the world, superhydrophobic surface would be a good candidate to be use as self-cleaning surfaces in solar cell panels.

The first reported artificial surperhydrophobic surface can traced back to 1986 when Sacher et al. reported that by depositing hexamethyldisiloxane on silicon chips in a high-energy plasma at low temperature, a water repellent surface with an extremely high water contact angle (~ 180°) and a near-zero roll-off angle can be obtained.[96] Since then, a broad range of technologies from top-down to bottom-up approaches have been utilized to make superhydrophobic surfaces. In general, anisotropic plasma etching and standard lithography procedures are widely used in top-down approaches to create the micro/nano-structures on the surface.[81, 93, 97-102] On the other hand, sol-gel,[87, 90-91, 103-104] layer-by-layer self-assembly,[92, 105-107] vapor deposition and microphase separation techniques are commonly used to generate the micro/nano-structures on the surface from the bottom.[88, 94, 108-110] Followed by hydrophobilization of the surface with a low surface energy material, such as CF_4 or semi-fluorosilanes, superhydrophobic surface can be easily obtained via both approaches.

1.3.1.2 Transparent Self-Cleaning Surfaces

Besides the requirement of a superhydrohobic surface to incorporate the self-cleaning property into PSCs, it is obvious that the transmittance of the coating should be as high

as possible so that the performance of PSCs will not be impacted. However, superhydrophobicity and transparency all depend on surface roughness and so, are generally antagonistic properties. While high surface roughness is a prerequisite to achieve superhydrophobicity, it may also cause undesired light scattering which diminishes the transparency of the coating. As light scattering, including Rayleigh scattering and Mie scattering, is a function of roughness size and the refractive index of the materials, it is critical to carefully control both the degree of roughness and the coating-substrate refractive index matching. To achieve the matching superhydrophobicity and transparency, it is recommended that the rough surface should be composed of features with a size close to 100 nm, to minimize undesired light scattering while still preserving its air trapping ability.[111]

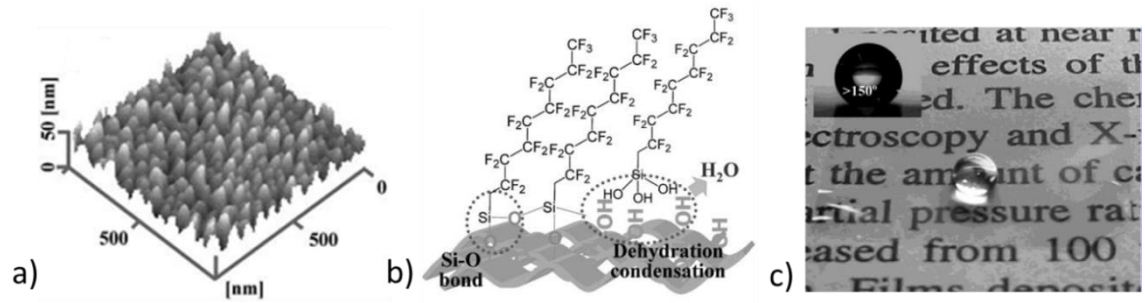

Figure 1.7: (a) Atomic force microscopy (AFM) shows a high density of nanohair structures on the PET surface after anisotropic oxygen plasma etching. (b) Hydrophobilization of the nanostructured surface by CVD of semi-fluorosilanes (c) Photographs of water droplets on the transparent superhydrophobic PET substrate after surface hydrophobilization.[99]

By selective removal of the noncrystalline domain in poly(ethylene terephtalate) (PET) sheet with anisotropic oxygen plasma etching, Teshima et al.[99] have created a high

density of sub-100 nm diameter nanohair structures possessing a height of ~ 150 nm (Figure 1.7). They imparted superhydrophobicity to the surface by modifying the rough surface with chemical vapor deposition (CVD) of fluorosilane. In similar fashion, various different polymers can be used to make transparent superhydrophobic surfaces.[112-115] Furthermore, similar geometrical nanostructures can also be made using inorganic nanorods, such as ZnO, from hydrothermal, vapor and sputtering processes.[116-120]

1.3.1.3 Mechanically Durable Transparent Self-Cleaning Surface

However, since polymers are generally soft materials and inorganic nanorods are quite fragile, they both lack mechanical robustness, which creates a big challenge for the commercialization of their superhydrophobic coating.[121] To enhance the mechanical robustness, inorganic nanoparticles (NPs) which possess higher Mohs hardness, such as silica, TiO_2, ITO, etc. could be used as material to form the rough structure. Cao and Gao[122] used layer-by-layer process to deposit multilayers of silica (20 nm) and polystyrene (PS) (60 nm) nanoparticle (NP) mixture on glass. Upon removal of the sacrificial PS NPs by calcination at 550°C for 4 hours, a hierarchical rough structure composed of silica NPs was obtained. Treating the film with fluorosilanes resulted in a superhydrophobic surface with a water contact angle of more than 160° and a transmittance higher than 90%. Karunakaran et al.[123] coated glass substrates by dip-coating 3-Aminopropyltrimethoxysilane (APTS)-functionalized silica NPs of two sizes (20 nm and 100 nm) in sequence to create dual-scale roughness (Figure 1.8). A transparent superhydrophobic surface was finally obtained by vapor deposition of fluorosilane.

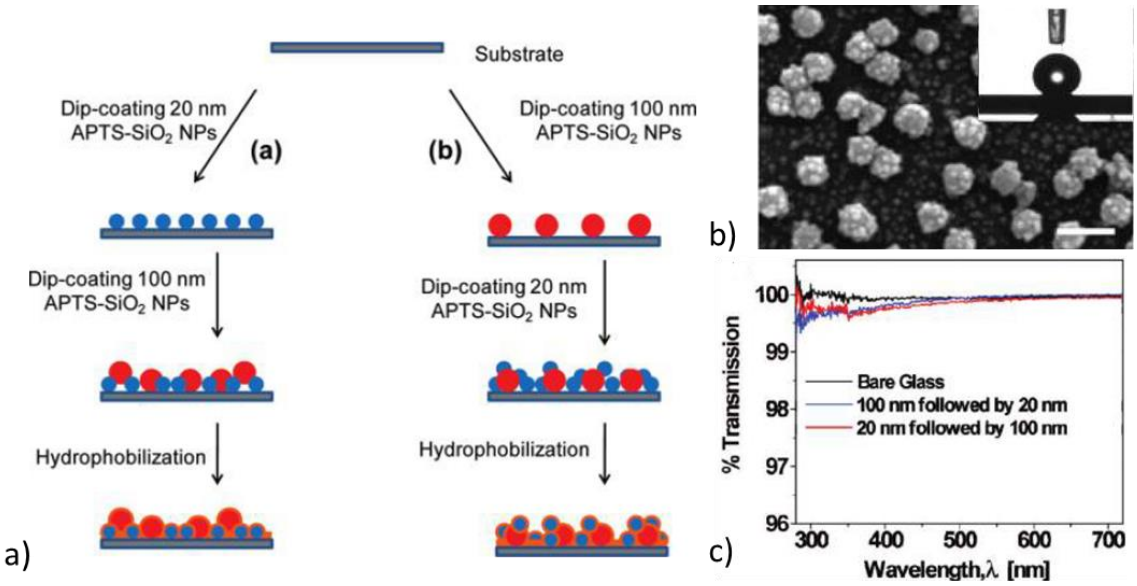

Figure 1.8: (a) Schematic illustration of the co-assembly of APTS-SiO_2 nanoparticles of different sizes. (b) SEM image of dual-sized APTS-SiO_2 nanoparticles successively dip coated onto Si wafers with 100 and 20 nm nanoparticles. (c) UV-Vis spectra of superhydrophobic nanoparticle films dip coated in different sequences and compared to bare glass.[123]

Again, the mechanical robustness of the obtained superhydrophobic surface in these methods is quite low as the adhesion force between NPs themselves, and between NPs and the substrate is not strong enough to survive in a simple tape peeling test.[124] Alternatively, hybridmaterials composed of hard NPs embedded in a polymer matrix shows a promising way to enhance the adhesion forces between NPs themselves and the substrate.[125-127] As an example, Francisco et al.[126] mixed oligodimethylsiloxane modified silica NPs with poly(methyl methacrylate) (PMMA) (the binder) in solution. Spray-coating of the mixed solution on glass resulted in a transparent superhydrophobic surface with improved mechanical stability.

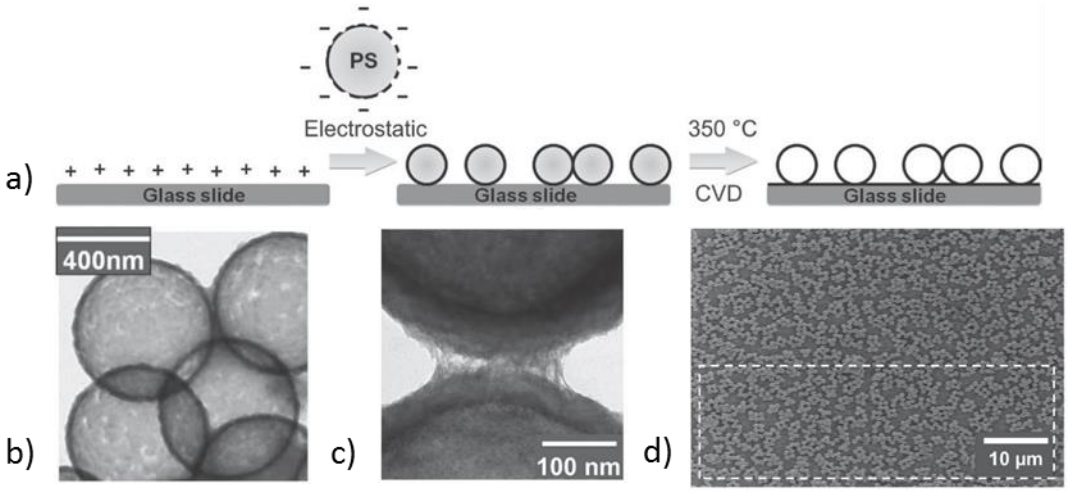

Figure 1.9: (a) Sketch of the procedure undertaken to prepare transparent superhydrophobic surfaces. (b) TEM image taken after the PS core has been removed by calcination. (c) High resolution TEM image of two neighboring silica capsules connected by a silica bridge that formed during CVD of tetraethoxysilane. (d) Particles can't be removed by double sided tape after binding them chemically to the surface by silica bridges.[128]

Instead of using solid materials as construction blocks to fabricate transparent superhydrophobic coatings, hollow structured materials with low volumetric density values could also be used. As the hollow structured materials show decreased back scattering efficiency and increased light transport mean free path,[129] up to micro sized roughness can be achieved with relatively high transparency, yielding a good compromise between superhydrophobicity and transparency without sacrificing too much in surface roughness.[128, 130] Deng et al.[128] synthesized raspberry-like spherical particles by attaching nano-sized silica NPs (~ 50 nm) on the surface of micro-sized PS spheres. After layer-by-layer processing to transfer the raspberry-like particles on top of glass following by calcination at 350°C to remove the PS template, they obtained a superhydrophobic surface with a water contact angle of 160° after surface

hydrophobilization. Interestingly, the transparency of the coating was found be the same as glass (Figure 1.9). Furthermore, they coated the surface with a thin layer of CVD deposited silica to lock-bridge the individual hollow microspheres, which enhanced the adhesion force between the micro structure and the substrate. After silica deposition, the coating is reported to have survived the peeling test with double sided adhesive tape pressed at 10 kPa and an impact abrasion test by sand grains (100 – 300 µm) with impact energy of 1.6 x 10^{-9} J. However, the high calcination temperature used to burn off the template (350°C) is not suitable for low thermal resistant substrates, not to mention environmentally harmful and energy demanding, and thus, is not fit for large scale production. Furthermore, due to the spherical shape of the hollow raspberry-like particles, which lessens the interaction between the structure and the substrate, the ability of the coating to survive at outdoor conditions remains highly doubtful. Pursuing new methodology to generate large scale, highly transparent and mechanically robust superhydrophobic surfaces is still ongoing, which should provide a boost for the development of self-cleaning PSCs.

1.3.2 Light Trapping by Nanostructured Materials

Besides incorporating nanostructured materials at the outmost surface of PSCs to impart the self-cleaning property to PSCs, embedding nanostructured materials inside the PSCs is also useful. Preliminary reports on enhanced light absorption in nanostructured PSCs indicate that light trapping can be realized by embedding nanostructured materials inside the PSCs to further enhance the PCE. Actually, light

management has already been shown to be a successful strategy in the development of low cost highly efficient crystalline silicon solar cells. The most mature crystalline silicon solar cells available on the market are constructed with a thickness of 180-300 μm to reach maximum light absorption. This results in both a high production cost and film quality requirement. Effective light management, including anti-reflection and light trapping realized by light scattering at the micron-size textured surface, is able to enhance light absorption inside the absorber, reducing the film thickness as well as production cost. Based on statistical ray optics analysis, the maximum achievable absorption enhancement for a solar cell can be estimated by Yablonovitch limitation of $4n^2$, where n is the refractive index of the absorbing material.[131-132]

In PSCs, limited by the trade-off of a strong interference effect and low carrier mobilities, the optimum photoactive layer thickness for state-of-the-art material systems is normally around 100 nm, resulting in low absorption efficiency between 60% to 80%.[133-135] Therefore, light management is also considered as an important strategy to further enhance the PCE of PSCs. However, light management achieved in crystalline silicon solar cell based on micron-scale textured surface is not suitable for PSCs because of their high surface roughness. New light management strategies based on nanostructured materials have been proposed and are considered to be promising for PSCs, but are still under development due to difficulties in their integration.[66, 136] Several groups have shown light absorption enhancement by integrating the nanostructured

materials inside PSCs to boost the PCE.[64, 137-143] Chen et al.[142] incorporated nanoimprinted deterministic aperiodic nanostructures (DANs) into single-junction PSCs

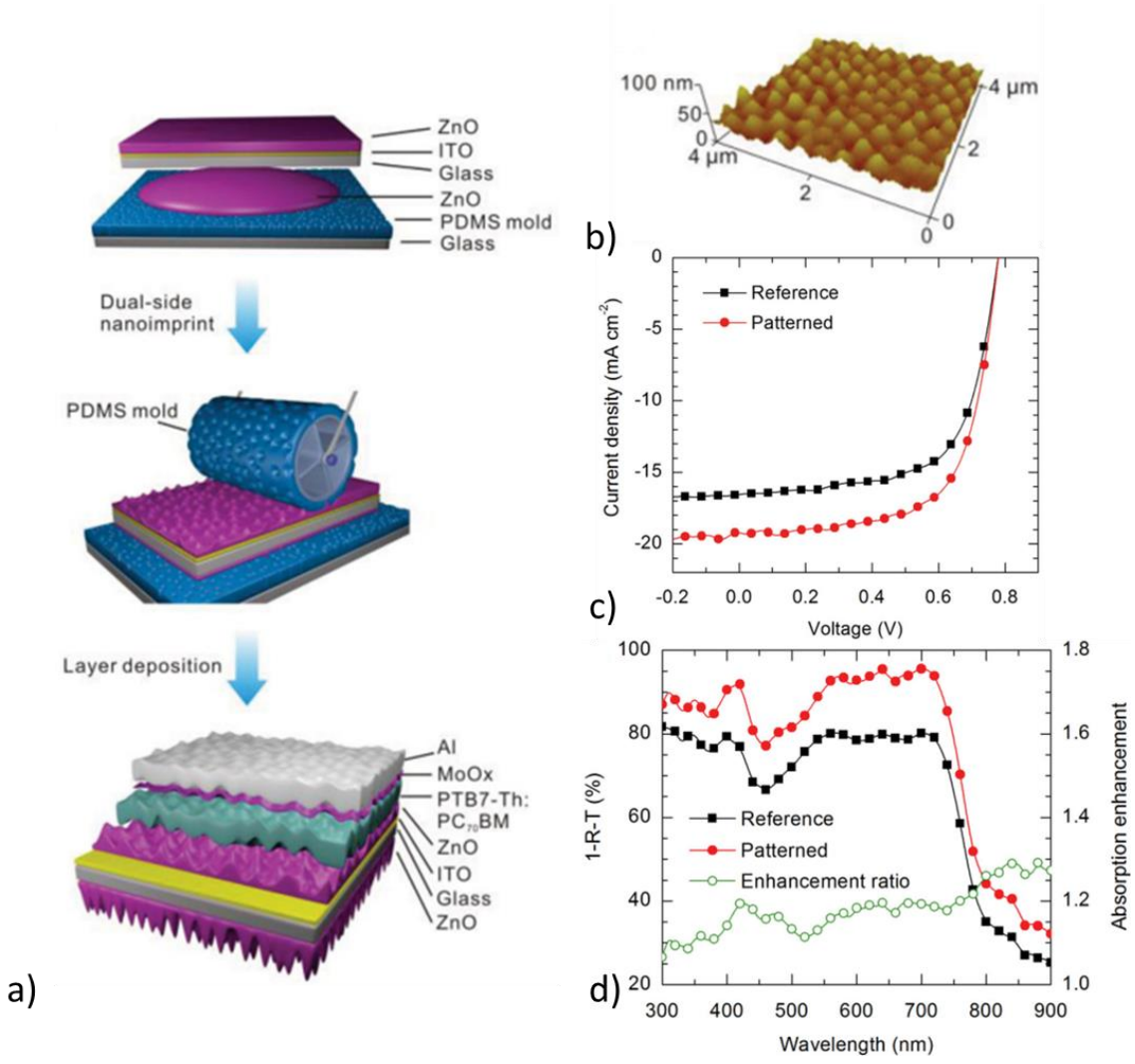

Figure 1.10: (a) Schematic illustration of the fabrication process flow for a nanostructured PSC with nanoimprinted DANs. (b) AFM image of the subsequently spin-coated PTB7-Th: $PC_{71}BM$ active layer on top of the nanoimprinted nanostructured ZnO layer. (c) Current density versus voltage (J–V) characteristics of PSCs in nanostructure and flat device configuration, recorded under 100 mW cm^{-2} AM 1.5G simulated solar illumination. (d) Absorption spectra of the devices with and without nanoimprinted DANs, and absorption enhancement.[142]

with poly[4,8-bis(5-(2-ethylhexyl)thiophen-2-yl)benzo[1,2-b:4,5-b'] dithiophene-*co*-3-fluorothieno [3,4-b]thiophene-2-carboxylate]:[6,6]-phenyl-C71-butyric acid methyl ester (PTB7-Th:$PC_{71}BM$) blend as the photoactive layer (Figure 1.9). Compared with the reference device with a flat bulk heterojunction structure, they achieved enhanced light absorption in nanostructured PSCs, yielding an 18% increase in photocurrent without sacrificing the charge transport properties. The light absorption enhancement was stated to be caused by self-enhanced absorption due to collective effects of the pattern-induced anti-reflection, light scattering as well as the surface plasmonic resonance.

1.4 Application of Multi-junction Structures to PSCs

As mentioned previously, even though the PCEs of single junction PSCs have approached the 10% milestone for commercialization, the relatively high production cost remains as the major challenge. Kalowekamo and Baker[70] performed analysis on the production cost of PSCs and found that the cost of transparent conductive substrate occupies a large percent of the materials cost (34-36%). Meanwhile, the PSCs module cost is inversely proportional to the PCE. Hence, enhancing the PCE of PSCs is one of the most straight forward ways to reduce the module cost. To further enhance the PCE of PSCs, the issues of unsatisfying light absorption limited by the trade-off of strong interference effects and low carrier mobilities present in PSCs have to be addressed.[133-135] To overcome the light absorption problem as well as reducing the production cost, multiple PSCs connected in series with complementary absorbing photoactive layers stacked on top of the same transparent conductive substrate have been explored. This multi-

junction structure can also reduce thermalization loss of photonic energy during the photon-to-electron conversion process, resulting in PCEs that outperform the Shockley–Queisser limit. Indeed, the PCE of multi-junction PSCs are approaching the 12% mark in recent years.[144-149]

On the other hand, due to the daily and seasonal variability in solar irradiation, solar-to-electricity supply is intrinsically intermittent. To address this challenge, several important factors should be considered to utilize solar energy for world energy demand. Fundamentally, solar energy conversion, storage and distribution should have minimal environmental effect. A cost-effective way to achieve this ideal on the terawatt scale is quite challenging. A promising solution lies in the conversion of solar-to-chemical energy, which can be stored easily, transported effectively, and used upon demand.[67, 150-151] Particularly, solar driven water splitting attracts much attention as the only waste product upon utilization of hydrogen is water. As photoelectrochemical water splitting is normally done in an alkaline solution with inert electrodes, byproduct/side reactions can be diminished and the Faradaic efficiency is high enough to reach more than 90%.[152-154] Faradaic efficiency characterizes the fraction of charge involved in a desired electrochemical reaction divided by the total charge transferred into the electrolysis system. Although efficient photoelectrochemical water splitting with solar-to-fuel efficiency of 18.3% has been realized using an AlGaAs/Si tandem solar cell,[155] the high cost of commercialization still remains a concern. As PSCs has potential in large-area cost-efficient manufacturing, combining PSCs in photoelectrochemical water splitting

will benefit both. Regarding the energy barrier that exists in water splitting, a minimum potential of 1.23 V is required to provide the thermodynamic driving force, but 1.4-1.9 V is needed in practice because of overpotentials due to reaction kinetics.[67] Most of the reported high efficient polymer tandem solar cells cannot reach such a high voltage at their maximum power point, and so, triple-junction solar cells have often been used. Einster has shown an estimated solar-to-fuel efficiency of ~3.1% can be achieved by using a triple-junction PSC composed of one layer of a large bandgap polymer and two layers of small bandgap polymers.[156]

1.5 Objective and Organization of the Dissertation

This dissertation is divided into four chapters to accomplish two major goals in reducing the maintenance and production costs for PSCs. The first two chapters are aimed at developing environmentally robust transparent superhydrophobic coating which can be applied to PSCs to exhibit self-cleaning. In order to achieve this goal, three conditions should be fulfilled at the same time. First, the superhydrophobicity should be achieved (high water contact angle > 150° with low sliding angle < 10°) to impart self-cleaning. Second, the coating should be highly transparent so that the performance of PSCs won't be impacted. Lastly, the coating should be robust to the outside environmental conditions. This includes and not limited to the resistance to UV irradiation and mechanical impact. Although there has been extensive research about the development of superhydrophobic coatings, the consideration of transparency and environmental

robustness has not been completely explored. The first two chapters make contributions towards those issues.

Specifically, chapter 2 describes a strategy to turn a UV-sensitive transparent superhydrophobic surface into a UV-resistant one without impacting the transparency of the coating. In this chapter, the correlation of transparency and superhydrophobicity with respect to the length of ZnO nanorod is checked. ZnO nanorods with proper lengths are used to construct transparent superhydrophobic surfaces. As ZnO are typically prone to UV-triggered photo-oxidation reactions, the wettability of the constructed surface is altered from superhydrophobic to superhydrophilic under UV irradiation. To circumvent this shortcoming, a thin layer of chemical vapor deposited SiO_2 is proposed to cover the surface of the ZnO nanorods and act as a physical barrier. In this method, we created a highly transparent UV-resistant superhydrophobic surface which shows minimal impact on the figure of merit of the PSCs. Double-side tape peeling test shows decent adhesion of the nanostructure to the substrate. However, the sand bursting test shows the nanorod structure is more or less fragile to survive under high energy impacting conditions.

To achieve a mechanically robust transparent superhydrophobic coating, we proposed a novel methodology in chapter 3 to form arrays of hollow silica half-nanospheres via the breath figure approach. In our methodology, chemical vapor deposition of silica is performed at the same time as the formation of breath figures through water condensation. In this way, a thin layer of silica is formed to cover the condensed nano-

sized water droplets. Upon removal of the condensed water by simple evaporation in vacuo leaves arrays of hollow silica half-nanospheres on the surface. Nano-indentation performed on the hollow silica half-nanosphere shows a decent Young's modulus of ~ 52 GPa. As the formed silica half-nanosphere is hollow, transparent superhydrophobic coating was realized with submicron sized half-nanospheres.

The second objective of this dissertation is related to our group's interest in developing highly efficient multi-junction PSCs which is the focus of chapters 4 and 5. We show that an enhanced PCE can be realized by stacking multiple active layers on the same costive transparent conductive substrate. To successfully stack multiple active layers from distinct solution and processing conditions, an efficient recombination layer which can physically separate and electrically connect each subcells should be developed for multi-junction PSCs.

Specifically, chapter 4 describes the construction of homo multi-junction PSCs from an identical polymer absorber, which shows an enhanced PCE (8.3% vs 7.7%) compare to an optimized single junction PSC of the same polymer absorber. Combined optical and electrical modeling is utilized to simulate the multi-junction device performance, and shows acceptable consistency with the experimental results. Furthermore, due to the high open voltage (>1.8 V) achieved in homo-tandem PSCs, homo-tandem driven water splitting in an electrochemical cell with an estimated solar-to-fuel conversion efficiency of ~ 6% was achieved.

In chapter 5, a polymer:fullerene bulk heterojunction is joined together with colloidal quantum dots (CQD) to construct a CQD–polymer hybrid tandem. Compared to the strong absorption in the visible range by the polymer, CQD showed extended absorption in the near-infrared range. Combining CQD with polymers would open the path towards the construction of efficient hybrid tandem devices that combine the advantages of both parts. Different device architectures to construct the hybrid CQD-polymer tandem are proposed and tested in this chapter.

Chapter 2

Highly Transparent and UV-Resistant Superhydrophobic SiO_2-Coated ZnO Nanorod Arrays

(Paper published in ACS Applied Materials & Interfaces)[157]

2.1 Introduction

Superhydrophobic coatings can have a significant impact on the development of glass and plastics with self-cleaning[158-161] and anti-fogging[162-163] properties, while also adding value to a wide range of tribological[164-166] and microfluidics applications.[167-170] In superhydrophobic coatings, hierarchical roughness introduces multiscale voids and gaps, trapping air at the material-water interface and, in turn, inducing high contact angles (>150°) with water droplets, low contact angle hysteresis and sliding angles.

The design and development of self-cleaning coatings for use in solar panels is especially important given that nearly half of the overall power conversion efficiency of solar panels can be lost due to dust accumulation every year.[69] In addition to the water- and dust-repellent property requirements, superhydrophobic coatings for photovoltaics

must be highly transmissive to both visible and near-IR light as well as being UV-resistant and durable. A few recent studies discuss transparent superhydrophobic coatings applied to photovoltaics.[128, 160, 171] One promising approach utilizes solution-processed SiO_2-coated polymer microbeads that can be made hollow by calcination of the polymer template (350°C).[128] The resulting microcapsules can be bridged in a CVD step with SiO_2 precursors to yield a mechanically resistant and highly transparent coating that can be applied to organic photovoltaic (OPV) devices on glass.[128] Meanwhile, approaches by which highly transmissive and nanostructured coating materials can be produced in a sequence of low-temperature steps (<150°C) would make them applicable to a variety of flexible plastics, which is one of the key directions of research in the OPV community.[172]

Nanostructured oxides such as ZnO and TiO_2 possess high band gaps and, as a result, high visible transmissivities, and can be either solution-processed[117, 173-175] or hydrothermally grown using established methods.[105, 176] Notably, as light scatters across oxide arrays, parasitic reflectivity is suppressed, such that nanostructured oxides can be used to improve the transparency of glass.[177-180] Here, we describe the preparation of a highly transmissive (avg. 93-95%) and UV-resistant superhydrophobic coating based on SiO_2-coated ZnO nanorod arrays grown on ultra-thin seed layer (~ 5nm), and demonstrate that the presence of the superhydrophobic nanocomposite does not significantly impact the figures of merit of OPV devices. We also show that the sequential steps used for the preparation of the SiO_2/ZnO nanocomposite can be

reproduced on a thin transparent sheet (2x2”) of PET, which retains its superhydrophobicity upon repeated bending, suggesting that the superhydrophobic nanocomposite can be applied to flexible photovoltaics and displays.

2.2 Experimental Section

2.2.1 Preparation of the SiO_2-coated ZnO Nanorod Arrays

Materials: Zinc nitrate hexahydrate ($Zn(NO_3)_2 \cdot 6H_2O$, 98%) was purchased from Fisher Chemicals. Hexamethylenetetramine ($(CH_2)_6N_4$, 99%) and ammonium hydroxide (NH_4OH, 20% in water) were purchased from Acros. Acetone, isopropanol, chloroform, chlorobenzene, 1-chloronaphthalene, tetraethyl orthosilicate ($Si(OC_2H_5)_4$, 98%), and 1H, 1H, 2H, 2H-perfluorodecyltriethoxysilane (PTES) (98%) were purchased from Aldrich. (6,6)-phenyl-C71-butyric acid methyl ester ($PC_{71}BM$) was purchased from SOLENNE. Poly(3,4-ethylenedioxythiophene): poly(styrenesulfonate) PEDOT:PSS (Clevios™ P VP AI 4083) was purchased from Heraeus. Extran 300 detergent was purchased from EMD. All of the chemicals were used as received without any purification. Milli-Q water with a resistivity >18.0 MΩ·cm was used in the preparation of aqueous solutions. The glass slides were purchased from VWR (VistavisionTM) and the flexible sheets of polyethylene terephthalate (PET; thickness: 0.1 mm) were purchased from Goodfellow (ES301400). The adhesion tape used for the “scotch tape” experiment was purchased from 3M (Scotch (3M) Permanent Double Sided tape #34-8507-8235-9 1/2 wide).

Deposition of the ZnO Seed Layer: Bare glass slides and tin-doped indium oxide (ITO, 15 $\Omega\ sq^{-1}$) patterned glass substrates were first scrubbed with a diluted Extran 300

detergent solution to remove organic residues, and then immersed in a sonication bath of diluted Extran 300 for 15 min (Branson 5510). Next, the substrates were rinsed under flowing deionized water for 5 min and sonicated for 15 min each in baths of acetone and isopropanol. After a final last 5 min rinse in flowing deionized water, the substrates were dried under nitrogen. Regarding the ITO-coated glass: the ITO side was covered with a thin layer of PMMA drop-cast from a chloroform solution (0.25g/ml) in order to protect the conducting oxide during the sequential steps used for the preparation of the ZnO nanorod arrays. The substrates were placed in the sputtering chamber (Equipment Support Co., Cambridge, England) at a distance of 15 cm from the ZnO target. The chamber was evacuated to $6x10^{-8}$ Torr and refilled with argon to 5 mTorr, the pressure at which the deposition of the seed layer was processed (room temperature, RF power of 50 W). The thickness of the seed layer was adjusted by controlling the deposition time and checked by ellipsometry (M-2000, J.A. Woollam Co.).

Hydrothermal Growth of the ZnO Nanorods: The substrates coated with ZnO seed layer were suspended upside down in a container filled with an aqueous solution of zinc nitrate hexahydrate (0.025 M) and hexamethylenetetramine (0.025 M) at 90°C. The time of ZnO nanocrystal growth was varied from 0 to 1h in order to yield nanorod arrays of various lengths. Next, the substrates were removed from the hydrothermal bath and thoroughly rinsed under flowing DI water. Regarding the ITO-coated glass: the drop-cast thin layer of PMMA protecting ITO was carefully peeled off. Finally, the substrates were

dried under nitrogen and finally heated to 100°C in a vacuum-oven (3h) to remove residual water.

Deposition of the SiO_2 Scaffold: Samples with ZnO nanorod sizes optimized for transparency (growth time: 25 min), either on bare glass slides or on ITO-coated glass, were used for the next steps. Regarding the ITO-coated glass: the ITO side was covered with a thin layer of PMMA drop-cast from a chloroform solution (0.25 g/ml) to protect the conducting oxide during SiO_2 deposition and treatment with PTES. Next, the nanostructured substrates were subjected to UV-ozone for 15 min to activate the SiO_2 surface, and were then placed in a glass chamber, between 2 vessels containing 1 mL of tetraethoxysilane (TEOS) and 1 mL of ammonia, respectively. The glass chamber was slowly evacuated to 160 Torr and maintained at room temperature. The SiO_2 deposition time was varied between 1h and 12h to yield SiO_2 scaffolds of various thicknesses.

Passivation of ZnO/SiO_2 with PTES: The ZnO-nanostructured substrates (with or without SiO_2) were placed at the center of a petri dish with 2 mL of PTES in ethanol (1%, v/v) drop-cast on the edge. 2 mL of water was carefully drop-casted around the samples, avoiding contact with the PTES drops while providing a moist atmosphere. The petri dish was then covered and heated to 140°C (1h) in an oven in order to achieve the PTES surface passivation. Finally, the nanostructured substrates were carefully rinsed with acetone and further sonicated in acetone for 5 min to remove (i) unreacted PTES and (ii) the PMMA layer on the ITO-coated glass substrates.

2.2.2 Characterization Procedures and Supporting Analyses

Equipment and Characterization: Optical transmittance measurements were performed with a Cary 6000i UV-Vis-NIR spectrophotometer under normal incidence (ZnO nanostructured side). The reflectance measurements were performed with a Lambda 950 UV-Vis spectrophotometer (PerkinElmer) equipped with an integration sphere. The static contact angle was measured with a DSA100 from KRUSS, using DI water droplets of 2 µL. Note: when water droplets could not readily be transferred to the surface of the nanostructured substrate due to the superhydrophobicity of the surface, tweezers were used to gently tap the tip of the needle producing the droplets and to allow droplet deposition. As the droplets immobilized on the surface, the static contact angle was measured. The sliding angles were measured on 2 µL water droplets that were placed on the flat surface that was progressively tilted at a rate of 0.2°/s, and the angle at which the first of several droplets started to slide on the surface was recorded as the sliding angle (results averaged over a minimum of 3 measurements). Atomic force microscopy (AFM) was performed with a Dimension Icon scanning probe microscope (BRUKER) in tapping mode, and a high aspect ratio antimony-doped Si cantilever with a spring constant of 42 N/m (TESPA-HAR, Veeco) was used for the analyses; the radius of the tip was less than 10 nm. Scanning electron microscopy (SEM) was performed with a FEI Nova Nano 630 equipped with a through-lens detector; the acceleration voltage was tuned to 1-5 kV, spot size: 0.5-1.5, working distance: 1-3 mm. In the cross-section SEM characterizations, Pt was sputtered on the sample to compress the charging effects (deposition time: 20 s; current intensity: 5mA). X-ray diffraction (XRD) experiments were

carried out on a high-resolution D8 Discover from BRUKER with a Cu Kα radiation point source (k = 1.5406 Å); the scan range was set between 25 and 90 and a scanning rate of 1s/step was used for the measurements. A focused ion beam (FIB, Helios 400s, FEI) was used to prepare the samples for cross-sectional transmission electron microscopy (TEM) by a "lift-out" protocol. Prior to FIB milling, samples were coated with a polymer photoresist (PMMA) to protect the SiO_2-coated ZnO nanorod surface. The lamellae were thinned with a Ga ion-beam (30 kV, 0.28 nA) and cleaned at an accelerating voltage of 2 kV and a current intensity of 47 pA. High-resolution transmission electron microscopy was performed on a Titan ST, working at an accelerating voltage of 300 kV.

Water drop and sand bursting test: For water drop test, a plastic baker with bottom part punched by densely packed needles was used as the container. The bottom of the baker is circle in diameter of 10 cm. The size of the formed water droplet was calculated from the weight of a number of the water droplets and takes the average. Water droplet with average diameter of 3.2mm was used. The container fulfill with water was positioned 7 m on top of the test surface to simulate the rain fall. For each test, 1.2 L of water is used for each time, and the water is finished in 10 min. The static water contact angle and sliding angle was checked before and after each test. For sand bursting test, sea sand collected from KAUST beach was used. The size of the sand grains varies from 200 µm to 500 µm with an average size of ~ 350 µm obtained from the statistical counting under optical microscopy. The sand drops from 10 cm high and impact on the test surface in

45˚. For each sand bursting test, 45 g sand grains are used. The static water contact angle and sliding angle was checked before and after each test.

2.3 Results and Discussion

As part of the ZnO nanorod hydrothermal growth process, a seed layer of ZnO must be deposited on pre-cleaned glass (Figure 2.1a, step 1) to lower the activation barrier for crystal nucleation.[181] Here, the seed layer was deposited by magnetron sputtering (see Experimental Section), and the dependence of seeded-glass transmissivity on the thickness of seed layer was examined by UV-Vis spectroscopy. Figure 2.1b shows that the substrate transmittance gradually decreases as the thickness of the seed layer increases, indicating that the seed layer should be as thin as possible in order to minimize both the parasitic absorption and reflection. With the refractive index of ZnO on the order of 2.0,[182] the reflection of incident light at the air-ZnO interface is expected to be greater than that at the air-glass interface. For example, in glass coated with a 50 nm seed layer (Figure 2.1b, orange curve), 10% (avg.) loss in transmittance is detected in the visible region (400-800 nm), while the transmittance drops by *ca.* 50% in the UV region, thus significantly reducing the number of photons transmitted to the active layer of any solar cell in this portion of the spectrum. In contrast, when the seed layer thickness approaches 5 nm (Figure 2.1b, red curve), the transmissivity of the ZnO-coated glass is nearly equivalent to that of glass alone across the full spectrum (300-800 nm), with a minimal transmittance loss near the band gap of ZnO. Meanwhile, the seed layer

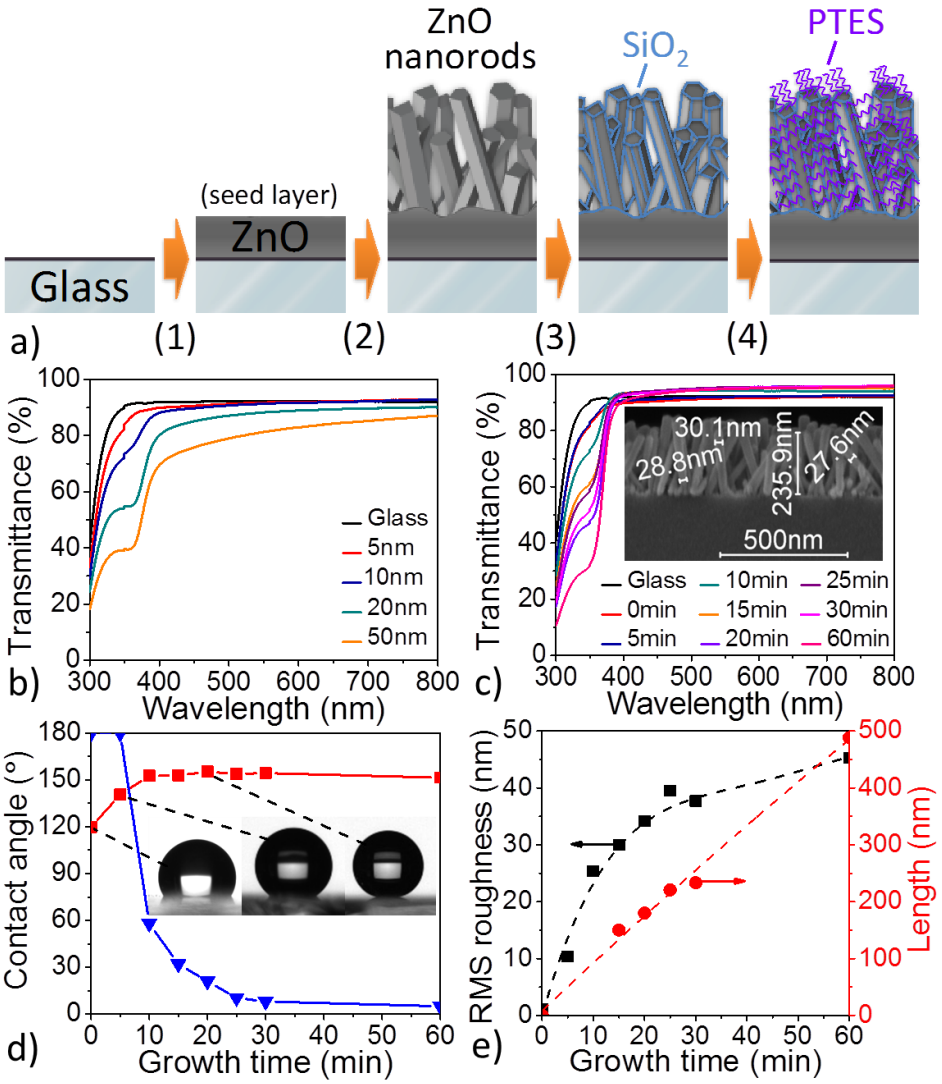

Figure 2.1: (a) Schematic description of the preparation of superhydrophobic SiO_2-coated ZnO nanorod arrays on glass (PTES= perfluorodecyltriethoxysilane). (b) Transmittance spectra of ZnO seed layers of various thicknesses (c) Transmittance spectra of ZnO nanorod arrays grown on 5 nm ZnO seed layer with different growth times. Inset: SEM cross-section of ZnO nanorods obtained after 25 min. (d) Evolution of the static contact (■) and sliding (▼) angles of PTES-treated ZnO nanorod arrays grown on 5 nm ZnO seed layer for various growth times. Inset: Photograph of a 2 µL water droplet placed on selected PTES-treated ZnO nanorod arrays. (e) Evolution of the surface roughness (RMS) (■) and average nanorod length (by SEM) (●) in relation to the ZnO-nanorod growth time.

should be sufficiently stable, that is, thick enough, to allow effective and homogenous ZnO nanorod crystal growth by the hydrothermal approach.[183] Experimentally, we found that a thickness of a few nanometers is required. We thus set the seed layer thickness at 5 nm in all following steps.

To develop a superhydrophobic coating with the highest possible level of transparency, a tradeoff between sufficient surface roughness and excessive scattering caused by overly long ZnO nanorods must be found. Figure 2.1c shows the evolution of the substrate transmittance as a function of the time allowed for crystal growth upon the seed layer (Figure 2.1a, step 2), and indicates a continuous loss of optical transmittance in the UV region as longer nanorods are formed. Interestingly, beyond 10 min of nanocrystal growth, the ZnO-coated glass substrate becomes more optically transmissive

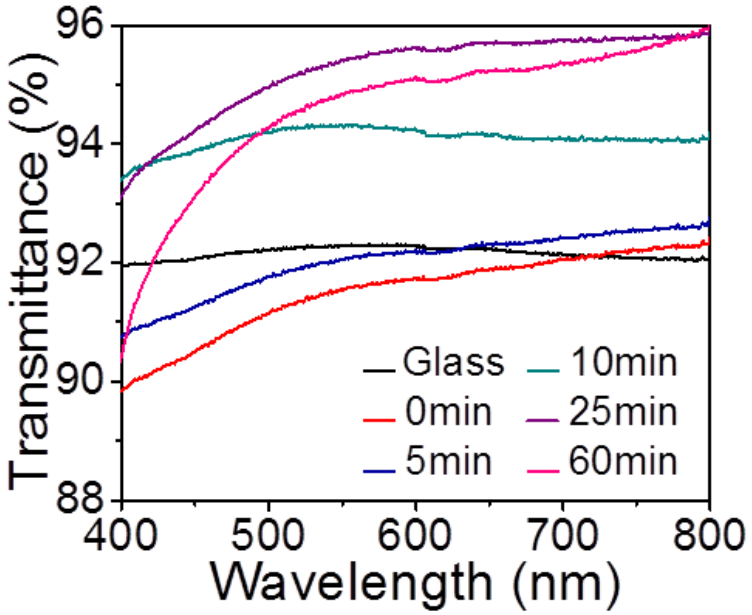

Figure 2.2: Enlarged transmittance spectra of ZnO nanorod arrays (non PTES-treated) grown on a 5 nm seed layer with different growth times.

than bare glass in the visible region. This effect can be attributed to the graded transition of refractive index across the nanostructured coating acting as an anti-reflecting material at the interface between glass and air.[180, 184] Meanwhile, as nanocrystal growth extends to 1h, the nanorod length reaches ~ 500 nm on average

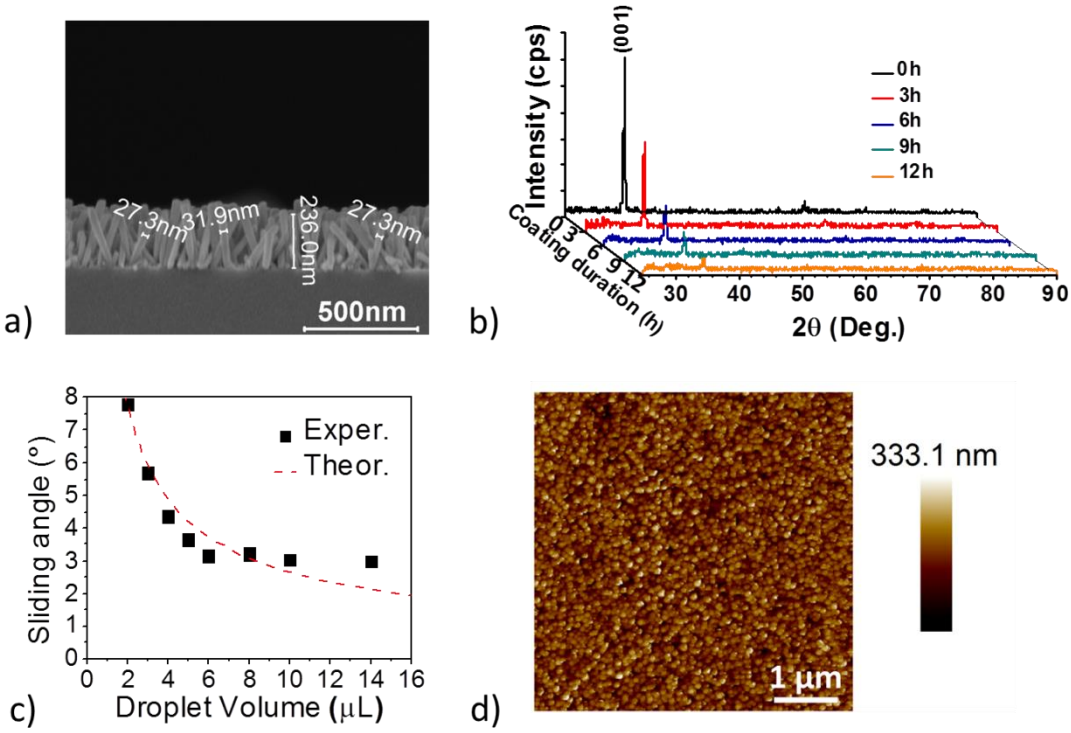

Figure 2.3: (a) Cross-section SEM image of ZnO nanorod arrays grown on a 5 nm seed layer with a growth time of 25 min. (b) X-ray diffraction patterns of ZnO nanorods (grown for 25 min on a 5 nm seed layer) with various SiO_2 deposition times (non-PTES-treated). (c) Effect of the volume of water droplets on the sliding angle (PTES-treated ZnO nanorods, grown for 25 min, on a 5 nm seed layer). (d) AFM image (5x5 μm) of ZnO nanorods grown on a 5 nm seed layer with a growth time of 25 min (non PTES-treated). Note: Imaging of the actual topography of the nanostructured surface is limited by the aspect ratio of the cantilever, yet a relative RMS roughness can be inferred from the measurement.

(Figure 2.2), thus falling in the range of visible light wavelengths and resulting in significant parasitic scattering.[123] The higher degree of visible transparency is achieved after 25 min of nanocrystal growth (Figure 2.2), as the nanorods reach a critical average length of ~ 240 nm with their diameters on the order of 30 nm (Figure 2.1c, inset, and Figure 2.3a): transmissivity values in the 93-95% range, compared with 91-92% for uncoated glass. The XRD analysis of the corresponding nanostructured glass (Figure 2.3b) shows a pronounced diffraction peak at 2θ=34.4° corresponding to the (001) crystal plane of ZnO and only a weak diffraction peak at 2θ=62.8° assignable to the (103) plane, indicating that most of the ZnO nanorods grow vertically on ZnO-seeded glass; this result is also shown qualitatively by SEM (Figure 2.1c).

It is worth noting that the surface of as-prepared ZnO nanorod arrays is hydrophilic,[116] meaning that water droplets will rapidly wet ZnO-coated glass in spite of the hierarchical roughness of the nanostructured oxide. Hydrophilic substrates exhibit small water contact angles and large sliding angles and, as such, they can easily accumulate water and dust. To circumvent the combined effect of polar hydroxyl groups at the ZnO surface and the capillary forces inducing the wettability, the nanorods are coated with a monolayer of perfluorodecyltriethoxysilane (PTES). At the ZnO nanorod surface, the PTES monolayer reduces the surface energy of the oxide,[185] and is expected to impart the superhydrophobicity. Figure 2.1d describes the superhydrophobic behavior of the perfluorinated ZnO nanorod arrays on glass as a function of the time allowed for crystal growth. While simple ZnO-seeded glass fluorinated with PTES (t=0) shows low static

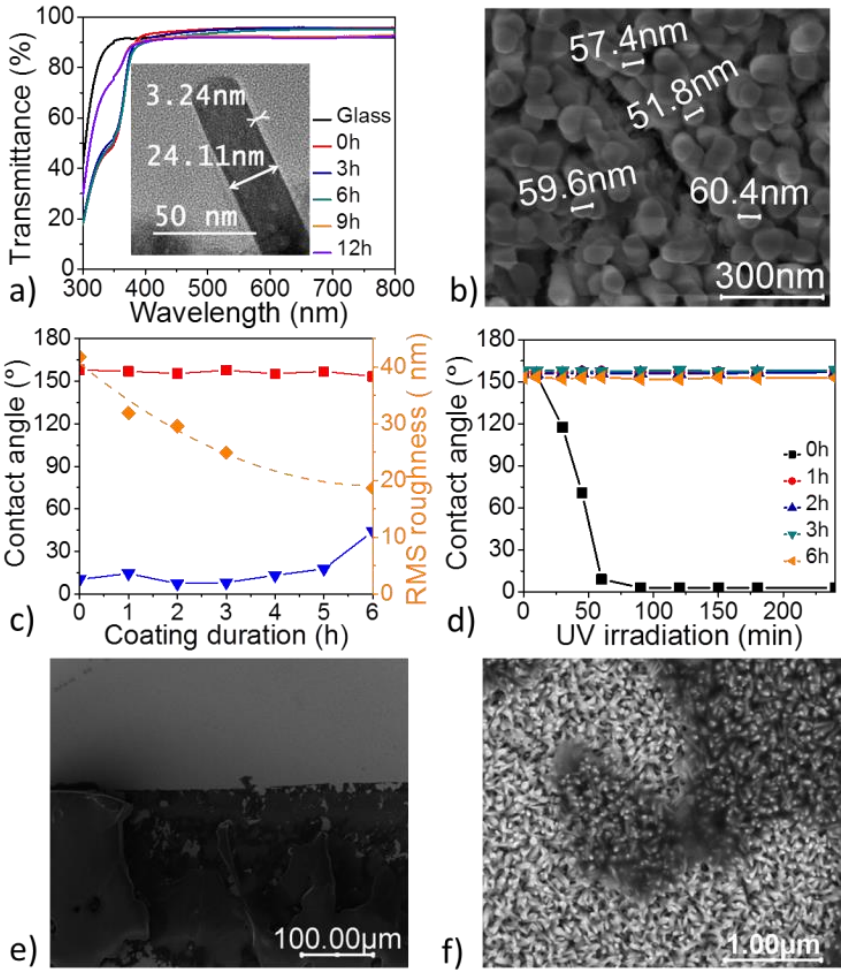

Figure 2.4: Transmittance spectra of SiO_2-coated ZnO nanorods (grown for 25 min on a 5 nm ZnO seed layer) for various SiO_2 deposition times. Inset: TEM image of SiO_2-coated ZnO obtained after 3h of SiO_2 deposition. (b) SEM image (top-view) of the SiO_2-coated ZnO obtained after 6h of SiO_2 deposition. (c) Evolution of contact angles and surface roughness (RMS) in PTES-treated SiO_2-coated ZnO nanorod arrays (grown for 25 min on 5 nm ZnO seed layer) for various SiO_2 deposition times: static contact angle (■), sliding angle (▼), surface roughness (◆). (d) Evolution of contact angles on PTES-treated SiO_2-coated ZnO nanorod arrays with UV irradiation time (365 nm, ~ 2 mW cm^{-2}) (e) SEM image of the SiO_2/ZnO nanocomposite surface after application and subsequent removal of a scotch tape pressed at 10 kPa for 1 min: the adhesive (dark region) peels off and remains bound to the nanostructured coating. (f) Magnified SEM image showing that the integrity of the nanorod arrays is retained under the bound adhesive (darker regions).

contact angle values of 120°, static contact angles greater than 150° can be reached rapidly beyond 5 min of nanocrystal growth. Meanwhile, the ZnO-nanostructured glass remains dominated by large sliding angle values greater than 20° during the first 20 min of nanocrystal growth, and it is only after about 25 min that the nanorod arrays become truly superhydrophobic, with static contact angles greater than 150° (as high as 157°, Fig. 2.1d inset) combined with markedly low sliding angles on the order of 10° and less (estimated from 2 µL water droplets). The influence of droplet size on sliding angle measurements is emphasized in Figure 2.3c. These results confirm that the surface state can be changed from Wenzel to Cassie-Baxter as the ZnO nanorods grow in length, that is, as the surface roughness increases as shown in Figure 2.1e. Figure 2.3d provides a topological depiction of the ZnO arrays after 25 min of growth by AFM from which the room mean square (RMS) roughness can be calculated. Considering both the high degree of transparency retained by the ~ 240 nm-long ZnO nanorod arrays obtained after 25 min of hydrothermal growth and their excellent superhydrophobic properties reached upon perfluorination with PTES, we used these arrays in the following steps and discussions.

While ZnO nanorods are typically prone to UV-triggered photo-oxidation reactions,[186-187] this shortcoming and the resulting gain in hydrophilicity can be circumvented by protecting the nanocrystal surface with a thin layer of UV-resistant material acting as a physical barrier.[105, 176] Here, we chose to protect the ZnO surface by a thin layer of SiO_2 (Figure 2.1a, step 3) deposited by CVD from tetraethoxysilane in the presence of

ammonia (see Experimental Section).[128] The XRD pattern of the SiO_2-coated ZnO nanorods with varying SiO_2 deposition times (t=0, 3h, 6h, 9h, 12h) is shown in Figure 2.3b, where the gradual reduction in the (001) diffraction peak intensity can be attributed to the screening of the ZnO nanorods by SiO_2. Figure 2.4a shows that layering SiO_2 on the ZnO nanorods does not further reduce the overall transmissivity of the nanostructured glass substrate. Thus, even after 6h of SiO_2 deposition at an estimated growth rate of ca. 1 nm h^{-1}, the transmittance of the coating remains on the order of 45%

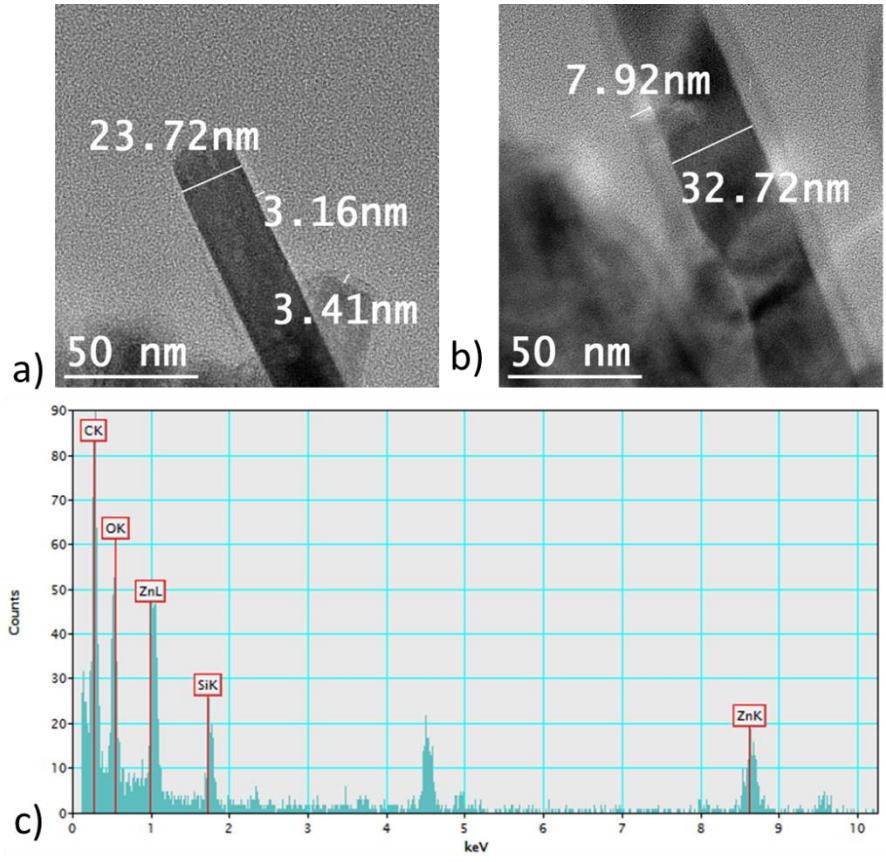

Figure 2.5: TEM image of ZnO nanorods (grown for 25min, on a 5nm seed layer) with SiO_2 deposition times of a) 3h, b) 6h, c) Energy-dispersive X-ray spectroscopy (EDX) spectrum of ZnO nanorods obtained after a SiO_2 deposition time of 6h.

(avg.) in the UV region and on the order of 93-95% across the visible region; the thickness of the SiO_2 layer deposited after 3h and 6h was determined by TEM and the imaged SiO_2-coated ZnO nanorods are shown in Figure 2.5, along with the energy-dispersive X-ray (EDX) analysis. As expected, the reflectance data shown in Figure 2.6 indicate that SiO_2-coated ZnO-nanostructured glass is less reflective (4-5%) than bare glass (8-9%). However, Figure 2.6 also indicates that the drop in the visible transmissivity of the SiO_2-coated ZnO nanorods beyond 6h of SiO_2 deposition (Figure 2.4a) can be correlated with an appreciable gain in the reflectance after the critical SiO_2 layer thickness

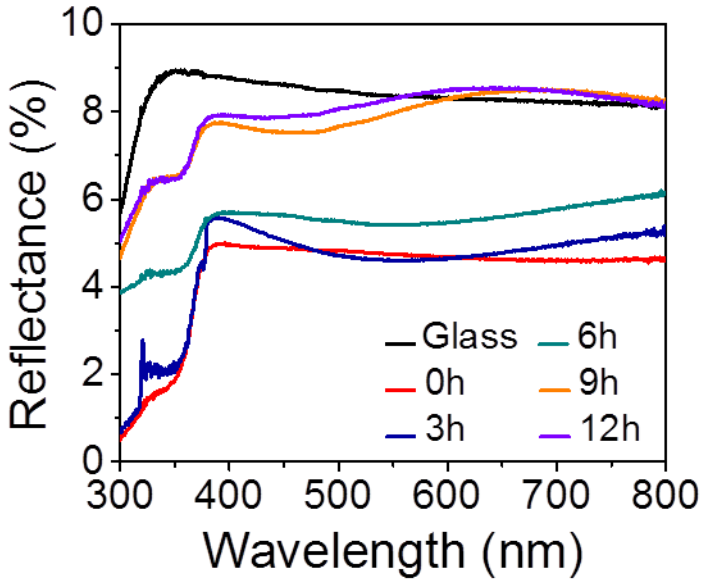

Figure 2.6: Reflectance spectra of SiO_2-coated ZnO nanorods (grown for 25 min on a 5 nm ZnO seed layer) for various SiO_2 deposition times (non-PTES-treated).

is reached. This empirical observation is in agreement with the coarsening of the ZnO nanorod diameter upon SiO_2 deposition (Figure 2.4b) and with the corresponding reduction of RMS roughness as shown in Figure 2.4c upon SiO_2 deposition. The SEM

cross-section of the SiO_2-coated ZnO nanorods shown in Figure 2.7 emphasizes the coarsening of the nanorod arrays resulting from 9h of SiO_2 deposition. In such conditions, the nanorods are almost fully bridged by SiO_2, while a rather continuous top layer of oxide starts forming, which is expected to increase the overall reflectivity of the coating. Figure 2.4c confirms that, upon perfluorination of the SiO_2 layer with PTES

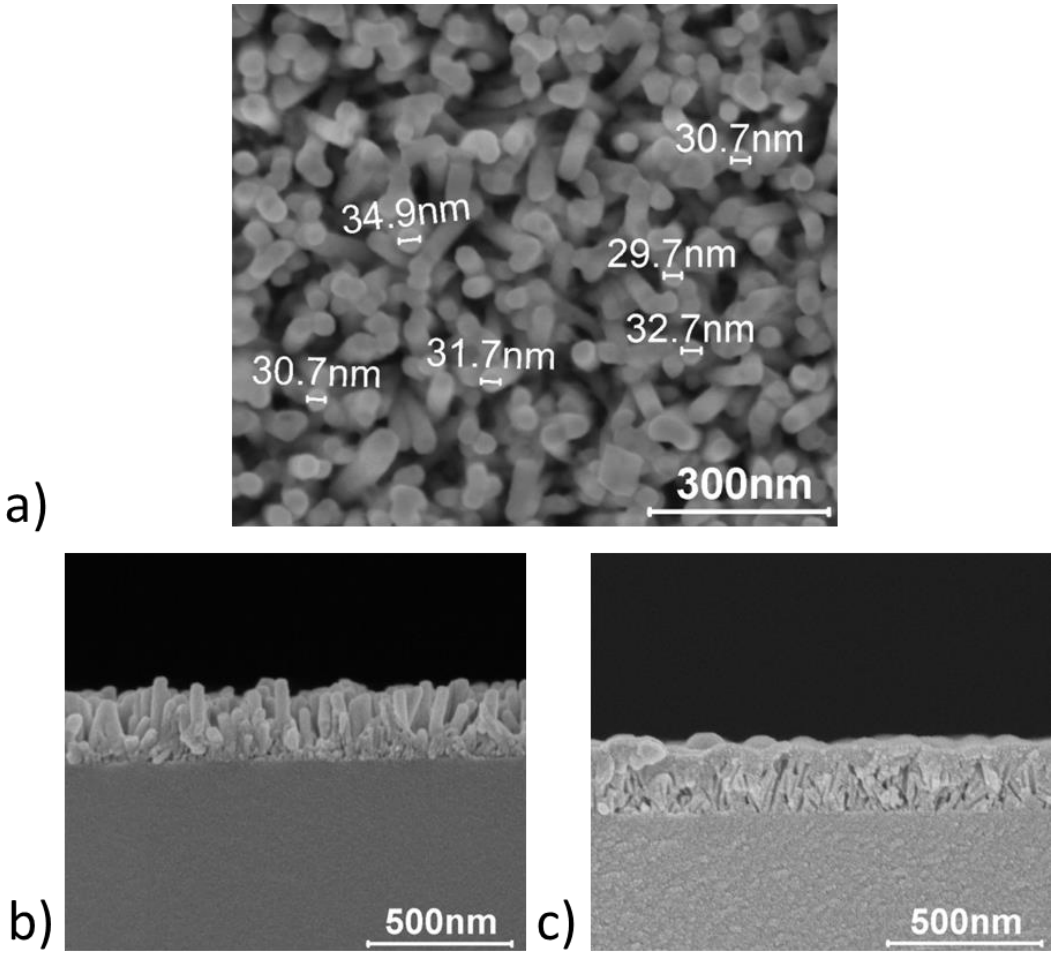

Figure 2.7: a) SEM image (top-view) of ZnO nanorods (grown for 25 min, on a 5 nm seed layer) obtained after a SiO_2 deposition time of 3h. b) Cross-section SEM image of ZnO nanorods (grown for 25 min, on a 5 nm seed layer) with SiO_2 deposition time of 3h, and c) 9h.

(Figure 2.1a, step 4), the SiO_2-coated ZnO composite becomes superhydrophobic. While the static contact angle of *ca.* 157° remains fairly constant for SiO_2 layer thicknesses in the range 1-6 nm, the sliding angle reaches values as low as *ca.* 7° (~2-3 nm) and then increases gradually when the SiO_2 layer thicknesses surpass ~6 nm. With a sliding angle larger than 40° after 6h of SiO_2 deposition (~7-8 nm), the superhydrophobicity of the nanostructured glass is compromised. This observation is consistent with the significant coarsening of the ZnO nanorod diameter upon SiO_2 deposition (Figure 2.4b). Importantly, Figure 2.4d shows that thin SiO_2 layers of *ca.* 1 nm (1h deposition) are sufficient to protect the ZnO nanorod surface and to avoid the dramatic increase in

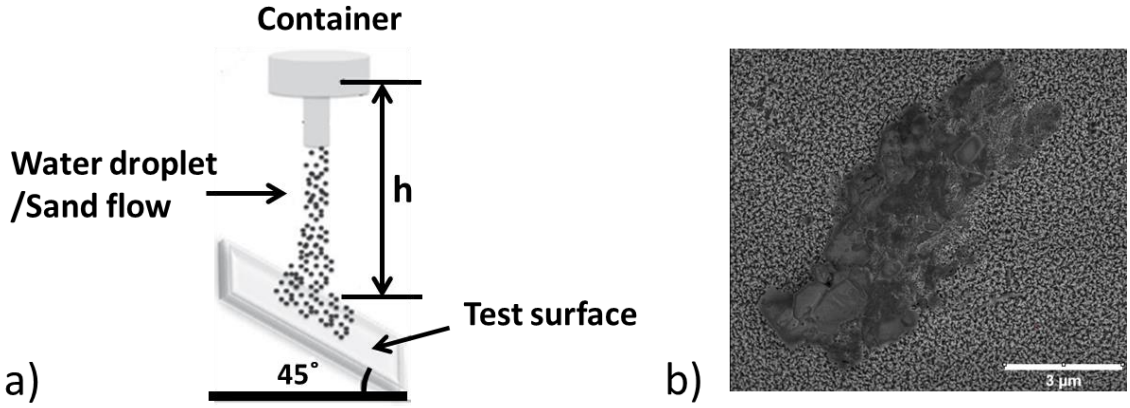

Figure 2.8: (a) Sketch of the setup used to perform water drop and sand bursting test. (b) SEM image of the surface after sand bursting test shows collapsed SiO_2-coated ZnO nanorods.

hydrophilicity caused by UV-triggered photo-oxidation reactions. In parallel, the adhesion of the SiO_2-coated ZnO nanorod arrays to glass substrate was qualitatively

assessed with a “scotch tape” experiment in which the adhesive tape was pressed at 10 kPa against the nanostructured surface for 1 min (see details in Experimental Section). Figure 2.4e shows that, upon removing the tape, the adhesive peels off from the backing material and remains bound to the SiO_2-coated ZnO nanorod arrays. The magnification of the nanostructured coating under the bound adhesive shown in Figure 2.4f confirms that the integrity of the nanorod arrays is retained. The mechanical robustness of the superhydrophobic surface was checked by the water drop and sand bursting tests (Figure 2.8a, see details in Experimental Section). In the water drop test, a high density of water droplets with an average diameter of 3.2 mm is released from 7 m above the test surface to simulate the impact of rain fall on the surface. Owing to the

Table 2-1: Summarized static water contact angle and sliding angle for PTES-treated SiO_2-coated ZnO nanorod arrays before and after the water drop test.

Sample	Static CA (˚)		Sliding angle (˚)	
	Initial	After test	Initial	After test
Silica 1h	156.9	156.4	14.5	13.5
Silica 2h	155.4	155.7	7.3	8.2
Silica 3h	157.7	157.9	8.1	8.5

air-induced deformation, the largest possible rain drop formed in nature is less than 5 mm in diameter, and the typical terminal velocity of the rain drop is in the range of 9–10 m s^{-1}.[188-189] If the water droplet is considered as a rigid sphere and the air friction force is simplified in the form of $F_{air} = C\pi r^2 \rho_{air} v^2$, in which C is the drag coefficient and has a value of 0.21 for an intermediate water droplet, r is the radius of the droplet, ρ_{air} is the

air density with a value of 1.2 kg m^{-3}. A water droplet with diameter of 3.2 mm dropped from a height of 7 m would have an end velocity of ~8.7 m s^{-1}.[189] Therefore, the performed water drop test can simulate well the impact of rainfall on the surface. The static water contact angle and sliding angle were checked before and after the water drop test, and the results are shown in Table 2.1. The indistinguishable change in characteristic angles before and after the water drop test demonstrates the stability of the transparent superhydrophobic surface in rainfall.

Besides rainfall, impact from high-speed aerosol particles in air is another frequently occurring natural event. To check the resistance of the transparent superhydrophobic surface to the impact of high speed aerosol particles, the sand bursting test was performed.

Table 2-2: Summarized static water contact angle and sliding angle for PTES-treated SiO_2-coated ZnO nanorod arrays before and after the sand bursting test.

Sample	Static CA (˚)		Sliding angle (˚)	
	Initial	After test	Initial	After test
Silica 1h	156.97	156.25	14.5	41.4
Silica 2h	155.49	155.53	7.3	33.6
Silica 3h	157.73	157.95	8.1	28.1

In this test, a continuous flow of sand grains in diameter of 200- to 500-µm hit the test surface at an angle of 45˚ from an elevated height of 10 cm, and the characteristic angles are recorded before and after the test. From the summarized results in Table 2.2, it can be clearly seen that the surface lost its superhydrophobicity after the sand bursting test. All of the water sliding angles increased to a value much higher than 10˚,

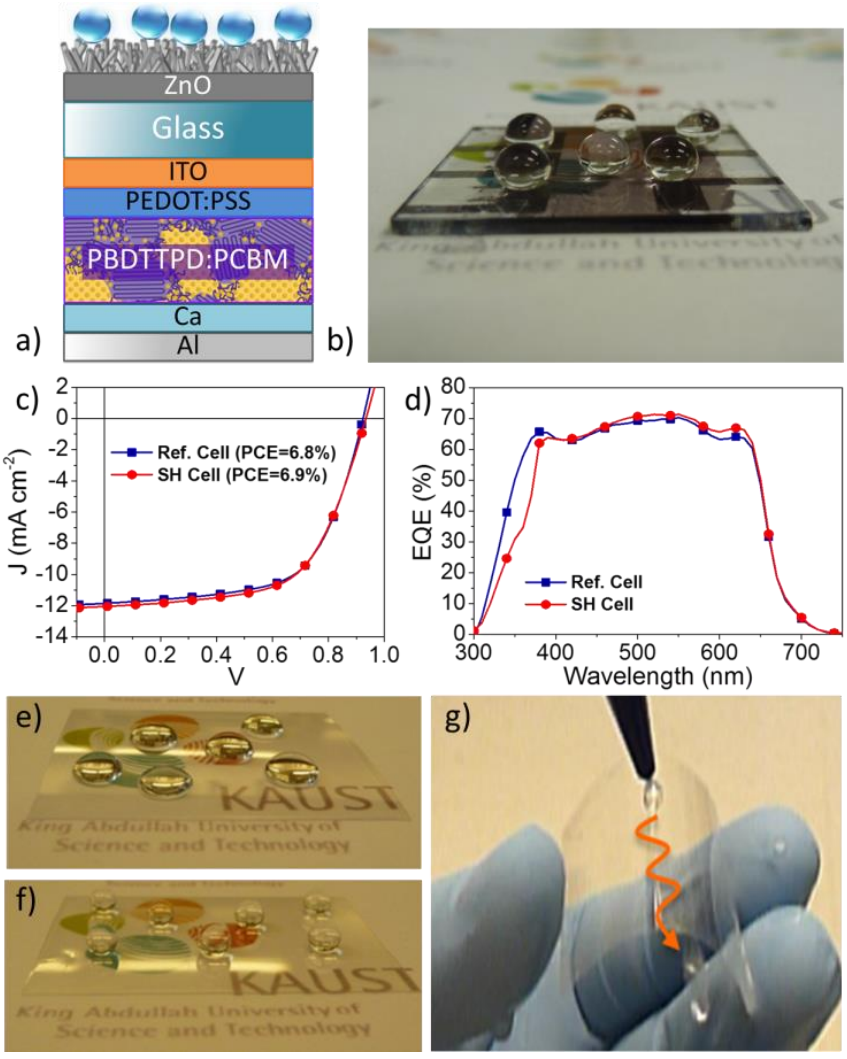

Figure 2.9: (a) Schematic of a BHJ polymer solar cell including the SiO_2/ZnO nanocomposite. (b) Water droplets positioned on the front of the superhydrophobic device remain perfectly spherical. (c) *J*-V characteristic of a superhydrophobic (SH) cell (●) superimposed on that of a bare reference (Ref.) cell (■); AM 1.5G solar illumination (100 mW cm^{-2}). (d) EQE spectra of the SH cell (●) and the Ref. Cell (■). (e) Water droplets positioned on a bare transparent sheet of PET (2x2"). (f) Droplets positioned on superhydrophobic PET (static angle: 160°). (g) PET retains its superhydrophobicity upon repeated bending (>200 times).

even though the static water contact angle is consistently higher than 150˚. The collapsed SiO_2-coated ZnO nanorods at the collision region shown in the SEM image (Figure 2.8b) reveal that the loss in superhydrophobicity is mainly caused by structural deformation under high-energy impact. Here, we note that making a mechanically durable superhydrophobic coating is a challenging task in the field and novel strategies need to be developed to improve the mechanical properties of the nanostructure.

To demonstrate the minimal impact of the presence of the superhydrophobic nanorod arrays on solar cell performance, we prepared bulk-heterojunction (BHJ) devices with the polymer donor PBDTTPD[190-192] and the fullerene acceptor $PC_{71}BM$ (see device fabrication in the Experimental Section). The configuration of the OPV device including the SiO_2/ZnO nanocomposite is shown in Figure 2.9a; Figure 2.9b shows perfectly spherical droplets positioned on the front surface of the superhydrophobic device (static angle: 157°, sliding angle: 13°). The superhydrophobic cell (red curve, circles) and bare reference cell (blue curve, squares) under AM1.5G solar illumination (100 mW cm^{-2}) (Figure 2.9c) exhibit equivalent current-voltage (*J*-V) characteristics with comparable PCEs of 6.9% and 6.8%, respectively – values comparable within the limits of experimental accuracy. In parallel, their external quantum efficiency (EQE) spectra (Figure 2.9d) show comparably broad and efficient EQE responses – with values >60% in the 370-630 nm range, and peaking at *ca.* 70% at 550 nm, which confirms the minimal impact of the presence of the superhydrophobic nanorod arrays on solar cell performance.

Ultimately, approaches to the preparation of highly transmissive superhydrophobic coatings in a sequence of low-temperature (<150°C) steps may be applicable to a variety of flexible plastics, which can serve as front cell and backing materials in the manufacture of flexible displays and solar cells. Noting that ZnO nanorod arrays can be grown hydrothermally on various plastics such as PET,[193] polydimethylsiloxane (PDMS),[194] and polyimide,[195] we considered reproducing the sequential steps used for the preparation of our SiO_2-coated ZnO superhydrophobic coating on a thin transparent sheet of PET (2x2”). Under the same experimental protocol (see details in Experimental Section), the PET surface, initially hydrophobic (Figure 2.9e), became superhydrophobic while retaining its high visible transmissivity (Figure 2.9f). On PET, the excellent static contact angle of 160°, comparable to that obtained earlier on glass (157°), was found to be relatively invariant upon repeated bending (Figure 2.9g; >200 times), a promising result in the context of future flexible thin-film device applications.

2.4 Conclusion

In summary, we have described the preparation of a highly transmissive (avg. 93-95%) and UV-resistant superhydrophobic coating based on SiO_2-coated ZnO nanorod arrays. On the one hand, we showed that the highest degree of coating transparency can be achieved upon carefully optimizing (i) the seed layer thickness and (ii) the size of the ZnO nanorods. On the other hand, we emphasize the critical dependence of the superhydrophobicity on (i) the ZnO nanorod length, (ii) the thickness of the SiO_2 layer and (iii) the presence of a UV-protective layer (here SiO_2 – only a few nm suffice) for the

ZnO nanorods. The superhydrophobic SiO_2/ZnO nanocomposite has minimal impact on solar cell device performance under AM1.5G illumination, and the sequential steps used for its preparation are applicable to both glass and plastics – thus validating the suggestion that the superhydrophobic arrays can be utilized in flexible displays and solar cells.

Chapter 3

Arrays of Hollow Silica Half-Nanospheres via the Breath Figure Approach

(Paper published in Advanced Materials Interfaces)[196]

As shown in the previous chapter, a highly transparent and UV-resistant superhydrophobic surface constructed from SiO_2-coated ZnO nanorod arrays can be integrated into PSCs to impart a self-cleaning property without degrading the figures of merit of the PSCs. However, the nanorod structure is fragile to high-energy impacting conditions. Therefore, harder construction materials, different nanostructures, and novel strategies should be developed to improve the mechanical properties of the superhydrophobic surface.

In this chapter, we show a novel methodology by which hollow silica half-nanospheres can be directly grown on the substrate to create a durable transparent superhydrophobic surface.

3.1 Introduction

A breath figure (BF) is a pattern that results from condensation on a cold surface; for example, the fog formed when a person blows on a cold window is a breath figure. Depending on the wetting characteristics of the surface, either a uniform film of liquid or an array of droplets can be formed. Because the nucleation and growth of liquid droplets that develop on de-wetting surfaces is of fundamental interest, there has been much research on the growth mechanism of BFs[197-202] since the first investigation reported by Lord Rayleigh in 1911.[203] In parallel, since BFs are simple (experienced daily), fast (formed instantly), and surface-dependent bottom-up (nucleation and growth) approaches to generating hundreds and thousands of liquid droplets on the nm and μm scales, there has been significant interest in finding key practical applications over the years.[204-206] Although BFs have long been used as an effective way of detecting oil contamination on glass down to the monolayer scale, it was only after Francǫis and coworkers showed that highly ordered and continuous honeycomb-structured films can be produced from BFs that the process began to garner broader attention across the scientific community.[206] In their report, a solution of star-shaped polystyrene was drop-cast under moist air flow, yielding a highly regular hexagonal pattern of water droplets self-assembled on the thin film of polymer solution by simple evaporative cooling. The authors showed that the imprint of water droplets can be replicated by selective precipitation of the polymer at the water/polymer solution interface. As water evaporated, arrays of hexagonally ordered and bowl-shaped or spherical pores – reminiscent of a honeycomb structure – formed throughout the hardened polymer film.

Since the pioneering work by Francǫis and coworkers, several reports have described the development of porous honeycomb-structured patterns by the BF approach on various types of materials,[207-214] and a number of important applications have emerged such as the manufacturing of highly ordered nano- and micron-sized templates,[215-217] micro lenses,[218] and superhydrophobic coatings.[219-221]

Despite significant effort to broaden the range of materials and substances that can be used to form porous honeycomb structures via the BF approach in the last decades,[216, 222-223] the lack of new findings in this area has limited pursuits of novel architectures and key applications. In this report, we describe an alternative method by which BFs can be used to produce arrays of hollow silica half-nanospheres. In our method, the nanostructured pattern of silica half-spheres is deposited on a glass substrate following a CVD protocol performed at room temperature (20°C) while the BF is formed (*i.e.*, the two processes are concomitant). During the process, the air/water interface on each water droplet provides a reactive surface for the hydrolysis of the silica precursor, resulting in the formation of a thin shell of silica around the water droplets pertaining to the BF. Upon removal of the condensed water by simple evaporation in vacuo, an array of hollow silica half-nanospheres remains on the substrate. We find that a wide size range of half-nanospheres (100-700 nm) can be formed on glass by controlling the relative rates of water condensation and hydrolysis from silica precursors (a process carried out at room temperature). In parallel, we find that the presence of surface heterogeneities evenly distributed across the substrate is a determining factor in the

formation of the BF templates achieved via our approach, whereas in conventional BF-forming approaches, the condensation of water droplets is triggered by the temperature difference at the air/substrate interface induced upon evaporative cooling of a thin film of liquid already on the substrate.[211] The scalability of our process is demonstrated on glass substrates as large as 7.5 cm x 3 cm onto which continuous arrays of hollow silica half-nanospheres are produced (the scale is limited only by the dimensions of the CVD chamber). With their high specific surfaces, low volumetric density values, and low refractive indices, hollow nanostructures find use in a wide range of applications, including photonics and optoelectronics,[224-225] surface catalysis,[226] and transparent nanostructured coatings (*e.g.,* superhydrophobic, anti-fouling).[128] We expect that our method of forming arrays of hollow half-nanospheres via the BF approach will be applicable to various other oxides and a broad range of substrates including large-area flexible plastics.

3.2 Experimental Section

Materials: Zinc nitrate hexahydrate ($Zn(NO3)_2 \cdot 6H2O$, 98%) was purchased from Fisher Chemicals. Hexamethylenetetramine ($(CH2)_6N_4$, 99%) and ammonium hydroxide (NH_4OH, 20% in water) were purchased from Acros. Acetone, isopropanol, chloroform, chlorobenzene, 1-chloronaphthalene, tetraethyl orthosilicate (TEOS) ($Si(OC_2H_5)_4$, 98%), 1H,1H,2H,2H-Perfluorooctyltriethoxysilane (PTES) (98%), and 1H,1H,2H,2H-Perfluorododecyltrichlorosilane (PTCS) (97%) were purchased from Aldrich. Extran 300 detergent was purchased from EMD. All of the chemicals were used as received without

further purification, unless otherwise mentioned. Milli-Q water (DI water) with a resistivity >18.0 MΩ·cm was used throughout the substrate cleaning steps. The glass slides were purchased from VWR (VistavisionTM), the fused silica slides were purchased from Antek Optics, and the silicon wafers were purchased from Luva system. Inc.

Substrate cleaning and hydration/dehydration pre-treatments: All bare glass slides were examined via short-wavelength UV light in order to differentiate between the “air-side” surface and the “tin-side” surface (inherent to the glass-making process), and the “air-side” surface was systematically used in all experiments. The glass slides, and the fused silica and silicon (with thermal oxidized layers of ca. 200 nm) substrates were thoroughly scrubbed with a diluted solution of Extran 300 detergent, and were then immersed in a sonication bath of diluted Extran 300 for 20 min (Branson 5510) to remove all organic residues. Next, the substrates were rinsed under flowing deionized water for 5 min and sonicated for 20 min in acetone and isopropanol baths. The substrates were immersed in isopropanol and left in the solvent for no more than two days before use. All of the substrates were dried under nitrogen flow before use. Hydration of the glass slides was carried out by i) immersing of the substrates in DI water, and ii) heating the substrates immersed in DI water to 85°C for a period of 24 h. Dehydration of the glass slides was carried out by heating the substrates at 500°C for a period of 3 h (under atmospheric conditions).

Synthesis of silica nanoparticles: 0.5 M TEOS solution diluted in ethanol and 0.5 M ammonia in ethanol prepared by diluting 20% ammonia solution in ethanol was first

prepared. The particle synthesis was initiated by mixing equal volumes of the prepared TEOS and ammonia solution with stirring at room temperature. The reaction was last for one day to ensure complete condensation of the precursor.

PTCS vapor deposition step: The vapor deposition of PTCS was carried out in a deposition chamber placed under inert atmosphere in a glovebox filled with nitrogen (H_2O < 0.1 ppm) in order to exclude the possibility that moisture affects the process. A deposition chamber (chamber diameter: 15.3 cm, height: 7.6 cm) equipped with a temperature-control stage, pressure-control valves and a flowmeter was used for the PTCS deposition step. The inside of the chamber was thoroughly cleaned with solvents between experiments. Before each deposition, the chamber was set under vacuum and pre-heated to the desired temperature for 2 h to remove any residual trace of moisture. Clean substrates with no pre-treatment were placed in a closed petri dish and annealed at 120°C for 2h in air and were then transferred to the glovebox (within 1 min). Hydrated glass substrates (85°C in DI water for 24h) were dried under nitrogen flow and quickly transferred into the glovebox (within 1 min). Dehydrated glass substrates (500°C for a period of 3 h in air) were taken out of the oven at ca. 120°C and quickly transferred into the glovebox (within 1 min). The substrates were then placed on the heating stage of the deposition chamber inside the glovebox and left on the stage for ca. 3 min before the PTCS deposition step. Next, a vial filled (Fisher Scientific, Product NO. 14-955-330, 20 mL) with PTCS (200 µL) was placed in the center of the deposition chamber and the chamber was rapidly evacuated and set under reduced pressure (ca. 130 Torr reached in

ca. 40 s, evacuation rate was controlled by flowmeter), thus initiating the deposition process. Upon reaching the desired PTCS deposition time, the chamber was slowly vented over ca. 4 min, and the substrates were taken out of the glovebox for the next deposition step. Post-deposition cleaning process was done by immersing the PTCS modified substrates in ethanol and sonicated for 1 h.

TEOS vapor deposition step: The substrates were placed in a second deposition chamber (chamber diameter: 10 cm, height: 12 cm) on a stage between two vessels containing tetraethoxysilane (TEOS, 1 mL) and an aqueous solution of ammonium hydroxide (20% w/v, source of ammonia, 1 mL), respectively. The chamber was then slowly evacuated over ca. 3 min to reach a reduced pressure of ca. 100 Torr, and the pressure valve was closed and the substrates were exposed to the water, TEOS, and ammonia vapors for the desired TEOS hydrolysis time. Upon reaching the desired TEOS hydrolysis time, the pressure was reduced back to its initially set value in the chamber (ca. 100 Torr, for ca. 3 min) to remove the vapor contents from the chamber. The chamber was vented, and the substrates were taken out of the chamber. All of the procedures were processed at room temperature (20°C). Note: A TEOS deposition time of 3 h was found necessary to form arrays of hollow silica half-nanospheres with a concentrated solution of ammonium hydroxide (20% w/v), while a TEOS deposition time of 6 h was found necessary to form arrays of hollow silica half-nanospheres with a diluted solution of ammonium hydroxide (2.5% w/v).

Preparation of transparent superhydrophobic surface from hollow silica half-nanospheres: Substrate with grown hollow silica half-nanospheres in size of ~ 700 nm was used. The substrate was immersed in 0.1 M HCl solution for 1 min to be positively charged, and then rinsed with DI water. After that, the charged substrate was immersed in the prepared silica nanoparticle solution for 1 min to attach the silica nanoparticles on the surface of the half-nanospheres following by rinse with DI water. The rinsed substrate was then placed at the center of a petri dish, and PTES in ethanol (1%, v/v, 2 mL) was drop-cast in places across the petri dish, around the substrate. Water (2 mL) was also carefully drop-cast around the substrate so as to induce a moist atmosphere. The petri dish was then covered and the closed vessel was placed in an oven and heated to 140°C for 1 h under atmospheric conditions. Finally, the hydrophobilized substrate was carefully rinsed with acetone and further sonicated in acetone for 5 min to remove unreacted PTES precursors.

Preparation of the superhydrophobic array of PTES-modified ZnO nanorods: A 5 nm seed layer of ZnO was sputtered on pre-cleaned glass slides (Equipment Support Co., Cambridge, England). Next, the substrates were suspended with the seed layer face down in a vessel filled with an aqueous solution of zinc nitrate hexahydrate (0.025 M) and hexamethylenetetramine (0.025 M) at 90°C. After 1 h, the substrates were removed from the hydrothermal bath and thoroughly rinsed under flowing DI water. The resulting ZnO-nanostructured substrates were placed at the center of a petri dish, and PTES in ethanol (1%, v/v, 2 mL) was drop-cast in places across the petri dish, around the

substrate. Water (2 mL) was also carefully drop-cast around the substrate so as to induce a moist atmosphere. The petri dish was then covered and the closed vessel was placed in an oven and heated to 140°C for 1 h under atmospheric conditions. Finally, the ZnO-nanostructured substrates were carefully rinsed with acetone and further sonicated in acetone for 5 min to remove unreacted PTES precursors. The resulting superhydrophobic substrates showed static water contact angles of ca. 160°.

Optical, morphology and nanoindentation characterization: Optical transmittance measurements were performed with a Cary 6000i UV-Vis-NIR spectrophotometer under normal incidence. AFM characterization was performed with a Dimension Icon scanning probe microscope (BRUKER) in the tapping mode, and an antimony-doped Si cantilever with a spring constant of 42 N/m (TESPA, Veeco) was used for the analysis; the standard radius of the tip was 8 nm. Particle analysis of PTCS aggregates was carried out by processing the AFM images with the offline data processing software NanoScope Analysis from Bruker. Nanoindentation was performed with Dimension Icon scanning probe microscope (BRUKER) working in nanoindentation mode, a hand-crafted high force diamond cantilever with a spring constant of 150 N/m was used (DNISP). The deflection sensitivity was determined by collecting force plot on silicon substrate. The morphology of the surface was first imaged in tapping mode, and then the cantilever was located on top of a well-shaped sphere by repeatedly zooming in. During the force measurements, the substrate was repeatedly moving up and down, and the change of cantilever deflection signal was recorded with the height position of the scanner. From

the deflection sensitivity and spring constant, the cantilever deflection signal was converted into force and the load/unload force vs indentation depth curve was obtained. By fitting the linear part of the load/unload force curve with Hertz model, the Young's modulus of the silica shell was extracted. SEM characterization was performed with a FEI Nova Nano 630 equipped with a through-lens detector; the acceleration voltage was tuned to 1-5 kV, spot size: 0.5-1.5, working distance: 1-3 mm. In the cross-section SEM characterizations, Pt was sputtered on the sample to compress the charging effects (deposition time: 25 s; current intensity: 15 mA). Particle analysis including particle area distribution, average particle area, and particle-to-glass coverage was carried out by analyzing the SEM images with the Java-based image processing program ImangJ 1.47v (National Institutes of Health, USA). TEM characterization was carried out with a Titan CT operating at an accelerating voltage of 120 kV. TEM sample preparation: the hollow silica half-nanospheres were lifted off from the substrates and were dispersed in ethanol before being solution cast on the TEM grid (Cu-300CN, Grid-Tech).

3.3 Results and discussion

The protocol established to form arrays of hollow silica half-nanospheres via the BF approach involves three steps (Figure 3.1a). First, the surface of the glass substrate is modified and made hydrophobic by depositing a thin layer of perfluorooctyltrichlorosilane (PTCS) under reduced pressure – this step is aimed at facilitating the formation of the BF (Figure 3.1a, step 1).[198] Second, the PTCS-coated

glass substrate is placed into a deposition chamber with separate ammonium and tetraethyl orthosilicate (TEOS) sources, and the setup is evacuated (Figure 3.1a, step 2). In this closed chamber under reduced pressure, the aqueous ammonium and TEOS solutions release water, ammonia and TEOS vapors. Compared with TEOS (boiling point: 166°C, molecular weight: 208.33 g/mol), water has a lower boiling point, and high water vapor pressures can be reached rapidly in the closed chamber. As a result, water condenses on the PTCS-modified glass substrate before the TEOS counterpart. In the presence of ammonia vapors, the TEOS precursor then undergoes hydrolysis at the air/water interface. As shown in Figures 3.1b and 3.1c, the outcome of this *in-situ* hydrolysis step depends on the morphology of the deposited PTCS film: while PTCS-modified glass subsequently subjected to a post-deposition cleaning process (see Experimental Section) shows low RMS roughness values characteristic of a smooth surface (Figure 3.2a; RMS= 1.73 nm) and is not amenable to the development of nanostructured patterns via the BF approach (Figure 3.1b), the “as-cast” PTCS-modified glass shows the presence of PTCS aggregates evenly distributed across the substrate (Fig. 3.2b; RMS= 4.33 nm) and can yield arrays of water droplets enfolded in thin shells of silica (Figure 3.1c). Here, we note that, as predicted by nucleation theory, water condensation does not occur on perfectly smooth surfaces unless the temperature difference between the vapor and the solid surface reaches *ca.* 25 K.[198] In the last step, the deposition chamber is set to a higher vacuum and the water template (BF) is stripped, yielding a dense array of hollow silica half-nanospheres on the PTCS-modified glass substrate (Figure 3.1a, step 3).

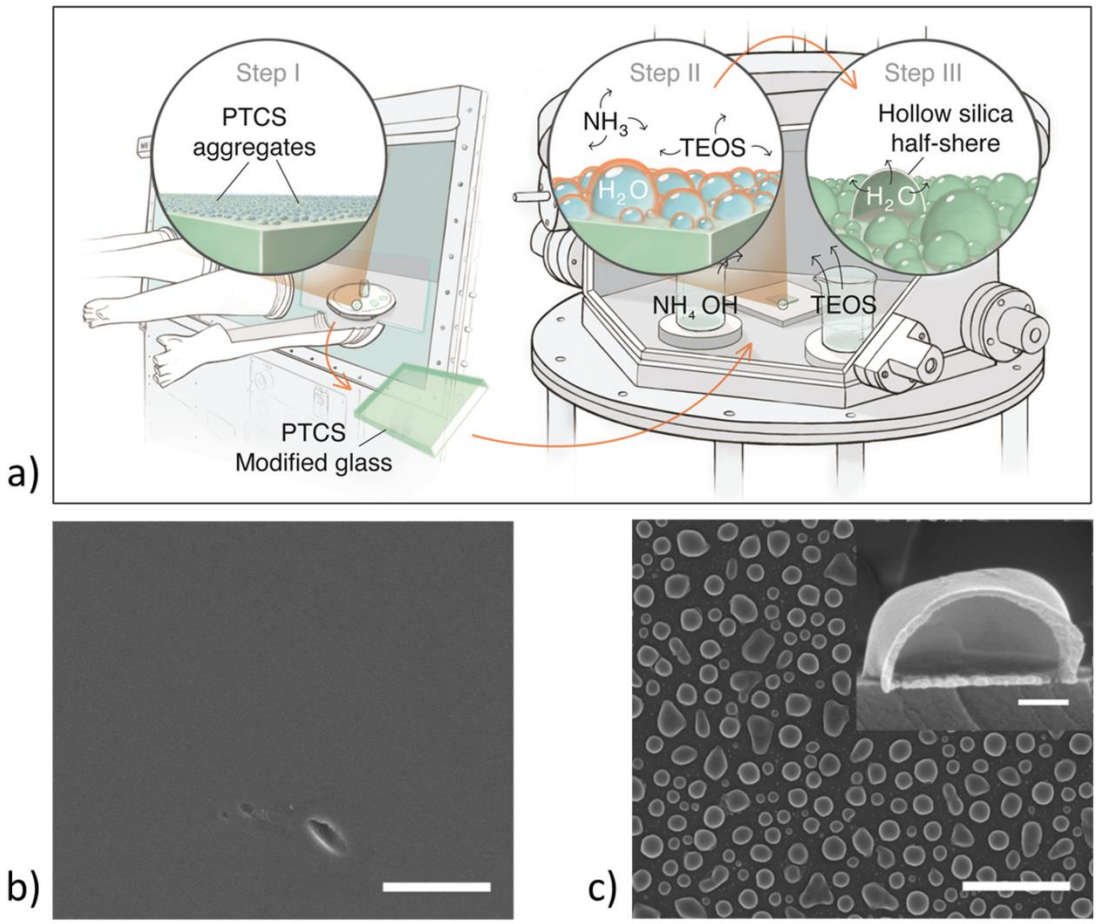

Figure 3.1: (a) Schematic illustration of the stepwise process of forming hollow silica half-nanospheres via the BF approach on PTCS-modified glass substrates (PTCS = perfluorooctyltrichlorosilane, TEOS = tetraethyl orthosilicate). (b) SEM image of a PTCS-modified glass substrate subsequently subjected to a post-deposition cleaning process (see Experimental Section), before exposure to an atmosphere saturated with water, ammonia (from a 20% w/v ammonium hydroxide aqueous solution) and TEOS vapors (3 h, room temperature, under *ca.* 100 Torr): the substrate is not amenable to the development of nanostructured patterns via the BF approach. Scale bar: 2 µm. (c) SEM image of an "as-cast" PTCS-modified glass (presence of PTCS aggregates) after exposure to the same TEOS precursor under the same conditions: arrays of silica "nanodomes" can be observed across the substrate. Scale bar: 2 µm. Inset: Magnified cross-sectional SEM image of one of the silica "nanodomes", emphasizing the hollow nature of the nanostructures; Scale bar: 150 nm.

As stated in previous studies,[227-230] the PTCS aggregates shown in Figure 3.2b to be evenly distributed across the glass substrate may result from the self-polymerization of

PTCS monomers induced during the vapor-deposition of the precursor, and they may only be physisorbed on the surface of the substrate. The vapor deposition of PTCS was performed under inert atmosphere (N_2) inside a glovebox (H_2O< 0.1 ppm) in order to exclude the possibility that moisture would affect the process. Under these conditions, well-dispersed PTCS aggregates were formed on the surface after 1 h of deposition at 90°C under reduced pressure (*ca.* 130 Torr) (Figure 3.2b). Although a variety of organosilanes have been reported to form spherical aggregates on various surfaces,[227-230] none of the reported precursors has been found to develop the aggregate assemblies with the narrow size-distribution depicted in Figure 3.2b (31.4±5.46 nm). Such regularity in size and coverage may be the result of the specific set of experimental conditions used, but could also stem from the nature and surface composition of the substrate itself as organosilane precursors are known to bind to surfaces via hydroxyl groups. In contrast to most of the reported work in which silicon substrates with a native oxidized layer are used,[231-232] our first set of experiments was performed on soda lime glass. In order to probe the effects of surface type and composition on the deposition of PTCS from the vapor phase, PTCS was deposited on several substrates – fused silica, silicon substrate with a thermally oxidized layer, borosilicate glass, and soda lime glass – following a 1 h vapor-deposition step at 90°C (parallel depositions in the same chamber), and the resulting morphologies were systematically examined by AFM. Different morphologies (*i.e.,* aggregate distributions and sizes) were found on different substrates, including a smooth surface on fused silica (Figure 3.3b), well-dispersed

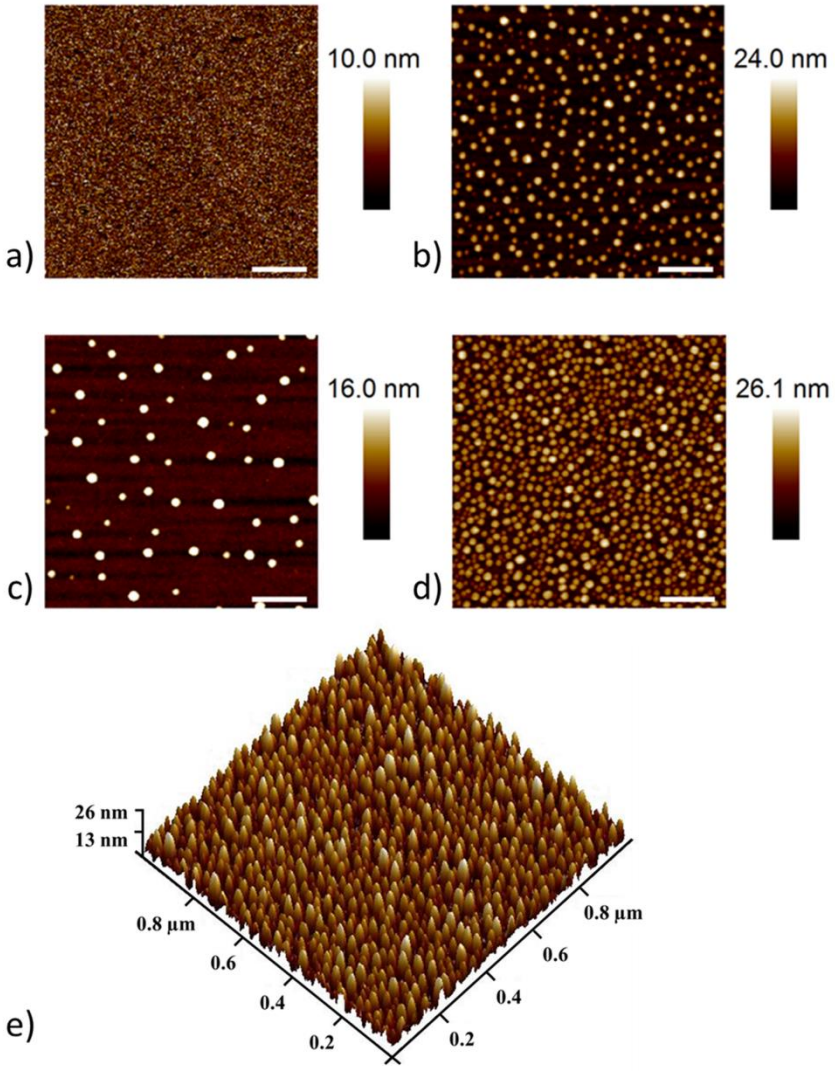

Figure 3.2: AFM images (1x1 µm) of (a) PTCS-modified glass after extended sonication in ethanol (1 h; see Experimental Section), (b) "as-cast" PTCS-modified glass composed of a continuous and dense pattern of PTCS aggregates (pattern obtained after 1 h of vapor deposition of PTCS at 90°C under a pressure of *ca.* 130 Torr), (c) "as-cast" PTCS-modified glass with aggregates formed on a hydrated glass substrate, (d) "as-cast" PTCS-modified glass with aggregates formed on a dehydrated glass substrate (see substrate preparation in Experimental Section), and (e) three-dimensional AFM image (1x1 µm) of the "as-cast" PTCS-modified glass with aggregates formed on a dehydrated glass substrate. Scale bar (a-d): 200 nm.

aggregates (*ca.* 27 μm^{-2}) with average heights of *ca.* 5 nm on the silicon substrate (Figure 3.3c), more densely distributed aggregates (*ca.* 87 μm^{-2}) with average heights of

ca. 7 nm on borosilicate glass (Figure 3.3d), and even higher densities of aggregates (*ca.* 290 μm^{-2}) with average heights of *ca.* 15 nm on soda lime glass (Figure 3.2b). Overall, these results show that the morphologies resulting from the deposition of PTCS from the vapor phase are surface dependent. It is also worth noting that the smooth morphology obtained on fused silica contrasts with the patterns of aggregates of different sizes formed on the different types of substrates, and that these empirical

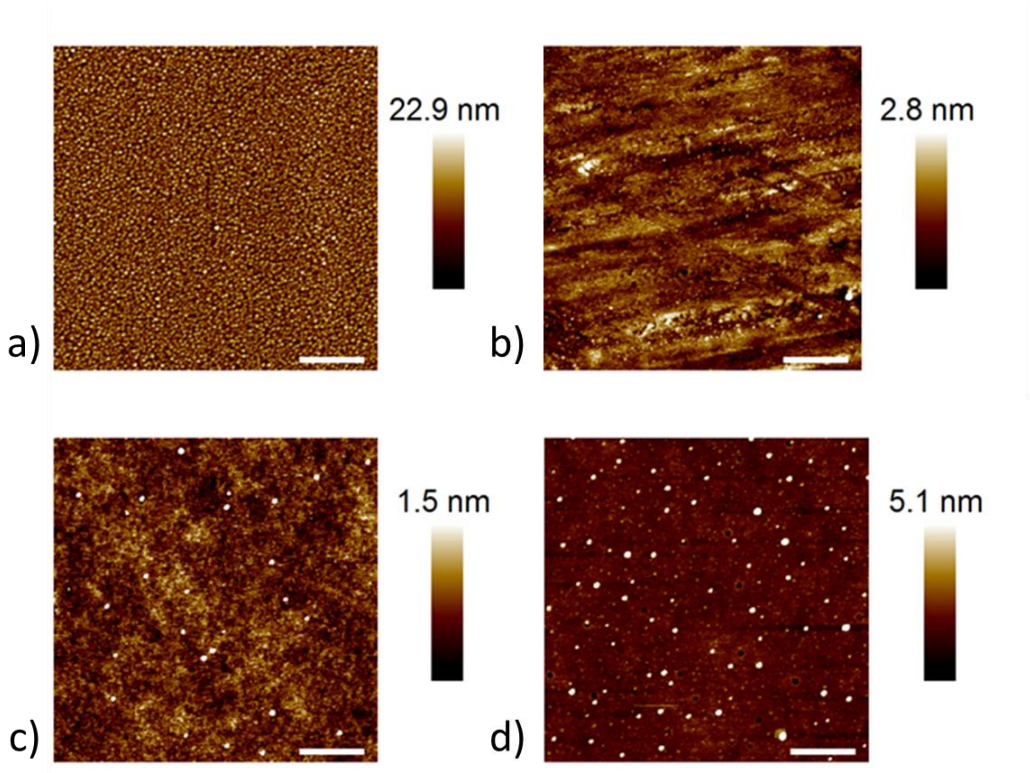

Figure 3.3: (a) AFM image (3x3 µm) of "as-cast" PTCS-modified glass composed of a continuous and dense pattern of PTCS aggregates formed on a dehydrated glass substrate (pattern obtained after 1 h of vapor deposition of PTCS at 90°C under a pressure of ca. 130 Torr); Scale bar: 600 nm. (b-d) AFM images (1x1 µm) of various PTCS-modified substrates (patterns obtained after 1 h of vapor deposition of PTCS at 90°C under a pressure of ca. 130 Torr): (b) fused silica, (c) silicon substrate with ca. 200 nm thermally growth oxidized layer, (d) borosilicate glass substrate; Scale bar (b-d): 200 nm.

observations point to a “nucleation-and-growth” mechanism sensitive to the substrate surface, ruling out the assumption of physisorbed aggregates formed in the vapor phase. We also noted that the same PTCS aggregates can form at the back of the substrates – a surface area that is not readily accessible to PTCS aggregates that would form from the vapor phase. This parallel observation further suggests that the PTCS aggregates are more likely to form directly on the vapor/glass surface.

The effect of surface hydroxyl groups was probed by first examining a soda lime glass substrate hydrated by heating the substrate in deionized water at 85°C for 24 h and second a soda lime glass substrate dehydrated at 500°C for 3 h.[231-232] PTCS aggregates formed upon a 1 h vapor-deposition step at 90°C on the hydrated and dehydrated substrates (parallel depositions in the same chamber) showed very distinct distribution patterns, as illustrated in Figures 3.2c and 3.2d. The hydrated substrate led to the development of well-dispersed aggregates (*ca.* 59 μm^{-2}) (Figure 3.2c) with average heights of *ca.* 15 nm, while the dehydrated one promoted the formation of densely distributed aggregates (*ca.* 798 μm^{-2}) with comparable average heights of *ca.* 15 nm (Figure 3.2d). It is also worth noting that the hydrated glass that was subsequently dehydrated also led to the formation of densely distributed aggregates, and *vice versa*. While the interplay between surface hydroxyl groups and the development of PTCS aggregates may be explained in terms of surface energy and remains a matter of discussion, these results clearly emphasize the requirement for a thorough surface treatment (*i.e.,* hydration or dehydration) before the PTCS vapor-deposition step in

order to yield reproducible patterns of PTCS aggregates on glass substrates. The uniformity of the resulting assemblies of PTCS aggregates on dehydrated glass is emphasized in Figures 3.2e and 3.3a (AFM image, 3x3 µm). In light of these empirical observations, and considering the net propensity of thermally annealed substrates to promote the development of densely-distributed PTCS aggregates, we used dehydrated glass in all following experiments, unless otherwise mentioned.

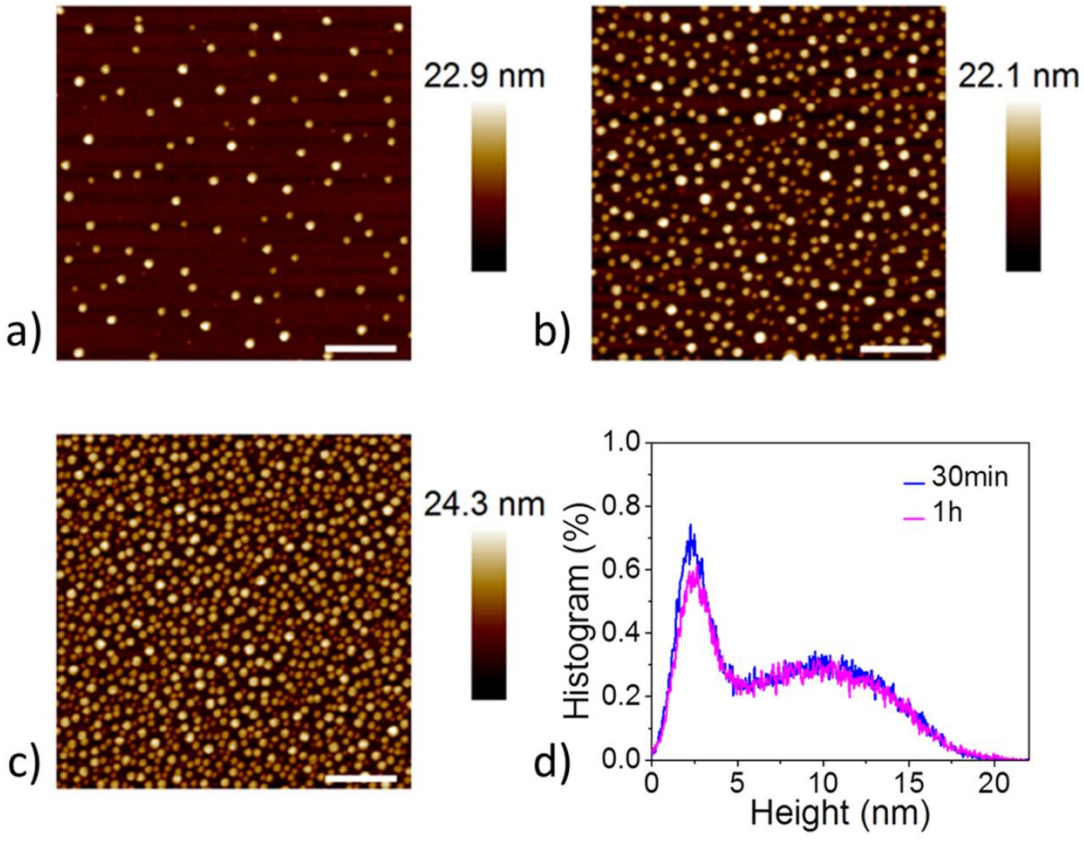

Figure 3.4: AFM images (1x1 µm) of distinct patterns of PTCS aggregates obtained on a dehydrated glass substrate after (a) 5 min, (b) 10 min, or (c) 30 min of vapor deposition of PTCS at 90°C under a reduced pressure of ca. 130 Torr. Scale bar (a-c): 200 nm. (d) Height histograms associated with PTCS vapor-deposition steps of 30 min and 1 h at 90°C.

The growth process of PTCS aggregates on glass was inspected by systematic AFM imaging of the patterns produced by vapor deposition steps of 5 min (Figure 3.4a), 10 min (Figure 3.4b), 30 min (Figure 3.4c), and 1 h (Figure 3.2d) on several substrates placed in the deposition chamber (sequential depositions) at 90°C under reduced pressure (*ca.* 130 Torr). Figure 3.4 depicts the rapid kinetics of aggregate formation, with aggregate densities of *ca.* 107 μm^{-2} achieved after only 5 min of PTCS deposition from the vapor phase. The density of aggregates then increased by a factor of 5 in the following 5 min to reach aggregate densities of *ca.* 494 μm^{-2} after 10 min of PTCS deposition. Higher aggregate densities of *ca.* 754 μm^{-2} could be reached after 30 min, leveling off at *ca.* 798 μm^{-2} after 1 h of PTCS deposition. Surprisingly, the aggregate size did not change significantly as a function of deposition time, and the particle size distributions remained relatively narrow and comparable between substrates: 23.3±6.6 nm after 5 min, 23.0±7.2 nm after 10 min, 21.8±8.3 nm after 30 min, and 22.6±9.7 nm after 1 h. These results suggest that both kinetic and thermodynamic considerations factor in the formation of PTCS aggregates, and may rapidly limit the size of the developing aggregates via two competing actions: 1) the frequency of attachment of the organosilane precursor at the specific conditions of temperature, pressure and precursor concentration in the vapor phase set during the deposition step, and 2) the formation of new stable aggregates (dependent on the surface free energy). Figure 3.4d shows the height histograms of the PTCS aggregate patterns obtained after the 30 min and 1 h deposition steps and account for the aggregate size distributions across the substrates (expressed in % of the total number of heterogeneities scanned by the AFM

tip) as a function of the aggregate height profile. With the radius of the AFM tip in the size range of the scanned aggregates, height analyses provide a more accurate description of the size distribution of the patterns compared with width analyses. Here, both height histograms include a sharp distribution of small-sized features (<5 nm on avg.) associated with the glass roughness and a broader distribution of larger features (>5 nm on avg.) pertaining to the PTCS aggregate patterns. These two histograms are

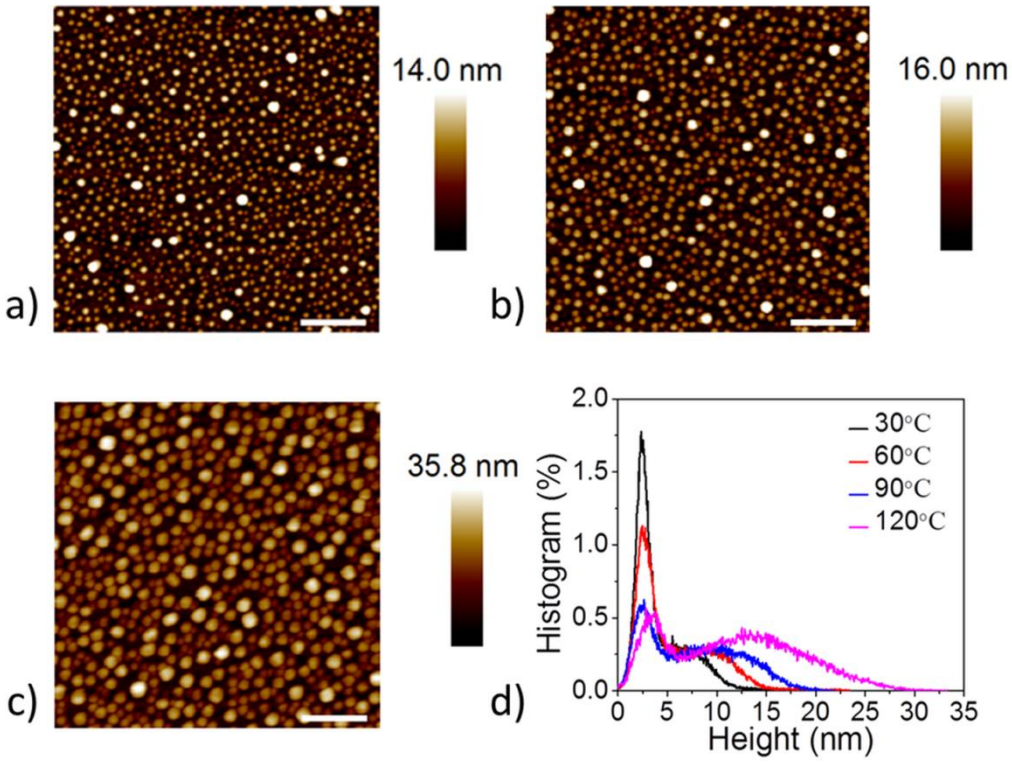

Figure 3.5: AFM images (1x1 µm) of distinct patterns of PTCS aggregates obtained on a dehydrated glass substrate after 1 h of vapor deposition of PTCS at (a) 30°C, (b) 60°C, and (c) 120°C under a reduced pressure of ca. 130 Torr. Scale bar (a-c): 200 nm. (d) Height histograms associated with PTCS vapor-deposition steps of 1 h at various temperatures ranging from 30°C to 120°C, in 30°C steps.

very comparable, indicating equivalent pattern compositions: relative densities of aggregates per size, size distribution and relative aggregate-to-glass coverage (inferred from the relative ratio of the two main peaks in each histogram) and in turn indicating that a critical density value of PTCS aggregates is achieved in 30 min.

The dependence of temperature on the growth of PTCS aggregates on glass was also examined by systematic AFM imaging of the patterns produced by vapor deposition steps of 1 h on several substrates (sequential depositions) at 30°C (Figure 3.5a), 60°C (Figure 3.5b), and 120°C (Figure 3.5c) under reduced pressure (*ca.* 130 Torr). As illustrated in Figure 3.5, the vapor deposition of PTCS at lower temperatures – 30°C and 60°C – yields patterns of smaller-sized aggregates with average heights of *ca.* 5 nm and *ca.* 7 nm, respectively, and narrower aggregate size distributions (16.4±5.7 nm and 19.2±7.0 nm, respectively), compared with the large-sized aggregates with average heights of *ca.* 18 nm and broader size distributions (28.2±12.6 nm) obtained at 120°C. The corresponding aggregate densities achieved after the 1 h PTCS deposition step are *ca.* 1026 μm^{-2} at 30°C, *ca.* 815/μm^2 at 60°C, and *ca.* 473 μm^{-2} at 120°C. The net increase in the average aggregate size and related decrease in aggregate densities across the glass with increasing temperature can be linked to the higher surface diffusion rates of the organosilane precursor expected at higher temperature. Figure 3.5d shows the height histograms of the PTCS aggregate patterns obtained upon 1 h deposition steps at 30°C, 60°C, 90°C and 120°C and emphasizes the significant shift in the average aggregate size towards larger size values with increasing deposition temperature. The histogram

also shows the corresponding increase in relative aggregate-to-glass coverage (inferred from the relative ratio of the two main peaks in each histogram).

As illustrated in Figure 3.1a, following the surface modification step via vapor deposition of PTCS, the glass substrate is placed into a second deposition chamber (see details in Experimental Section) along with an aqueous solution of ammonium hydroxide (20% w/v, source of ammonia) and the tetraethyl orthosilicate (TEOS) precursor at room temperature (20 °C). The pressure in the chamber is then reduced (*ca.* 100 Torr). In the presence of PTCS aggregates distributed across the glass surface and acting as "nucleation" sites, water droplets can easily condense and form a BF on the glass in spite of the absence of a temperature difference at the air/substrate interface. Upon exposure to the moist atmosphere saturated in water, ammonia and TEOS vapors for 1 h, the PTCS-modified glass substrate goes from initially transparent to translucent, indicating that water droplets have formed on the substrate – a process expected to be accompanied by hydrolysis of the TEOS precursor in the presence of ammonia at the air/water interface along with formation of a thin shell of silica (SiO_2) around individual water droplets. In the following few hours (1-6 h), the pressure within the chamber is reduced back to its initially set value (*ca.* 100 Torr) to remove the vapor contents from the chamber, and the translucent glass substrates become transparent again, suggesting that the water droplet volumes are also removed. As shown in Figure 3.6a, SEM imaging of the corresponding substrates (initially modified via PTCS deposition at 120°C for 1 h under *ca.* 130 Torr) shows arrays of randomly distributed silica "nanodomes". Figures

3.6b shows the SEM cross-section of the arrays and indicates that the silica "nanodomes" formed on PTCS-modified glass are hollow, as would be expected upon removing the water droplet volumes during the chamber evacuation step. Such arrays are referred to as "arrays of hollow silica half-nanospheres" in all following experiments.

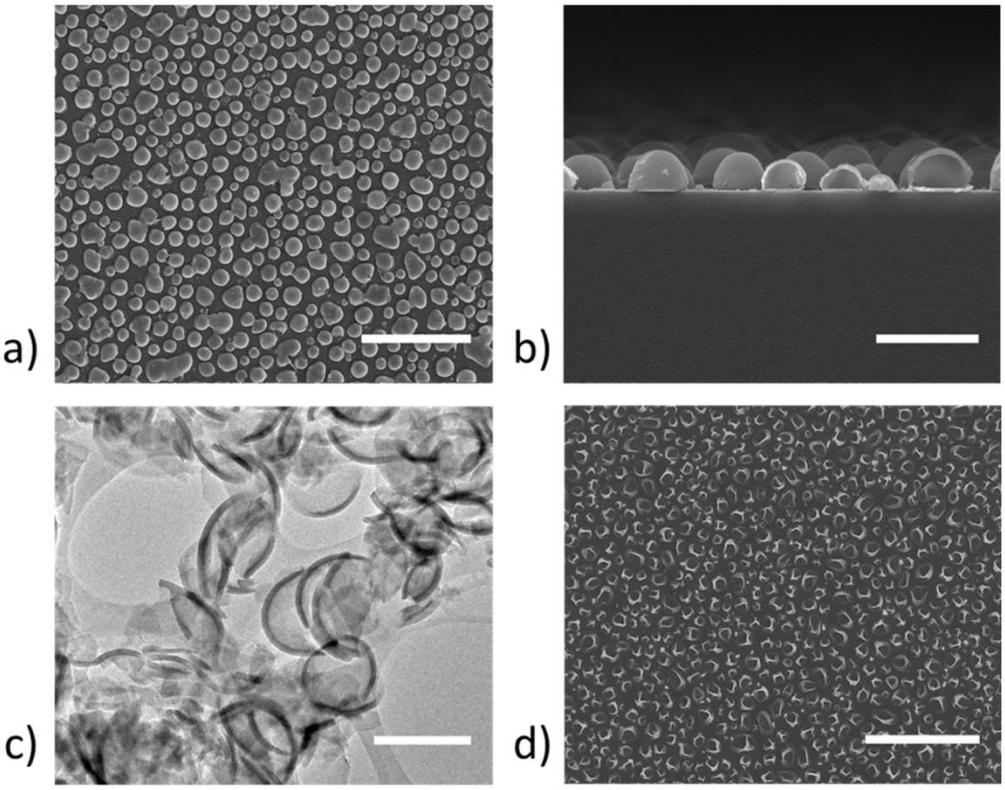

Figure 3.6: (a) SEM image of an array of hollow silica half-nanospheres formed on a dehydrated and PTCS-modified glass substrate (deposited at 120°C for 1 h, under ca. 130 Torr) upon 3 h exposure (room temperature, under ca. 100 Torr) to an atmosphere saturated in water, ammonia (from a 20% w/v ammonium hydroxide aqueous solution) and TEOS vapors, resulting in the hydrolysis of the TEOS precursor and in the formation of a thin shell of silica (SiO_2) around individual water droplets. Scale bar: 4 µm. (b) Cross-sectional SEM image of the same array of hollow silica half-nanospheres. Scale bar: 1 µm. (c) TEM image of the hollow silica half-nanospheres lifted off of the PTCS-modified glass substrate. Scale bar: 600 nm. (d) SEM image of an array of hollow silica half-nanospheres formed on PTCS-modified glass substrate prepared following the same protocol as described in (a) and subjected to TEOS hydrolysis for only 1 h (20% w/v ammonium hydroxide solution, room temperature, under ca. 100 Torr). Scale bar: 4 µm.

Figure 3.6c shows several half-nanospheres lifted off the PTCS-modified glass and imaged by TEM (see details in Experimental Section), indicating that the nanostructures possess a uniformly thin silica shell of *ca.* 30 nm thickness. Figure 3.6d depicts an array of partially collapsed silica half-nanospheres obtained upon a short hydrolysis step of only 1 h and emphasizes the requirement for longer TEOS deposition steps in order to form nanostructures that are sufficiently thick to maintain their integrity during the chamber evacuation process. The particle analysis (Figure 3.7) associated with Figure 3.6a shows a relatively broad particle size distribution with a mean surface area of *ca.* 0.259 μm^2 and a relative particle-to-glass coverage of *ca.* 57%. Earlier work on the

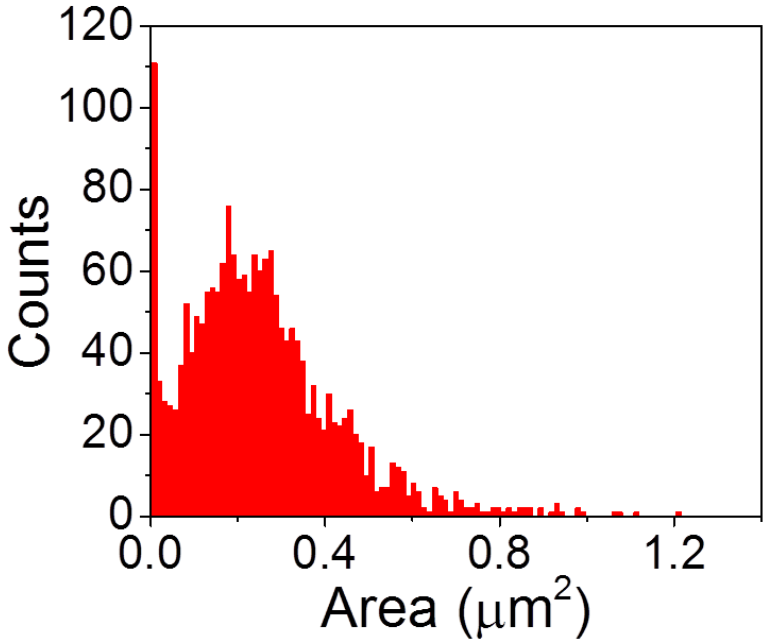

Figure 3.7: Area distribution map of silica half-nanospheres formed on a dehydrated and PTCS-modified glass substrate (deposited at 120°C for 1 h, under ca. 130 Torr) upon a 3 h exposure (room temperature, under ca. 100 Torr) to an atmosphere saturated in water, ammonia (from a 20% w/v ammonium hydroxide aqueous solution) and TEOS vapors.

temperature gradient-induced BF process[201] (as opposed to the PTCS aggregate-promoted approach discussed throughout our study) has shown that the relative particle-to-glass coverage of condensing water droplets on glass gradually increases in the early stages and levels off at *ca.* 57% after tens of seconds (scaling stage). This coverage estimate in the scaling regime (where the pattern characteristics, including particle size distributions and surface coverage, become independent of particle size), originally reported for water droplets of tens of microns,[201] is consistent with the relative particle-to-glass coverage inferred from the particle analysis pertaining to the array of half-nanospheres shown in Figure 3.6a, albeit with water droplet-templated feature sizes on the order of only 500 nm. In our experimental protocol, the high particle-to-glass coverage achieved with sub-micron sized water droplet templates could be the result of the PTCS aggregate-promoted BF approach used to develop and rapidly immobilize the pattern of water droplets formed on the glass substrate. We also note that, among all of the techniques known to date for the study of water condensation processes,[233-237] our experimental protocol provides a powerful tool for ex-situ analyses of water condensation in the very early stages.

We now turn to examining the parameters that govern the average size and the particle-to-glass coverage values associated with the formation of arrays of hollow silica half-nanospheres on PTCS-modified glass. The SEM images in Figures 3.8a, 3.9a and 3.9b compare the patterns of silica half-nanospheres obtained from various PTCS-modified glass substrates produced at 30°C, 60°C and 90°C, respectively. Given that the size and

density of PTCS aggregates distributed on glass substrates depend upon the deposition temperature (see Figure 3.5), each substrate yields a different pattern of silica half-nanospheres under fixed conditions of TEOS hydrolysis (3h, 20% w/v ammonium hydroxide

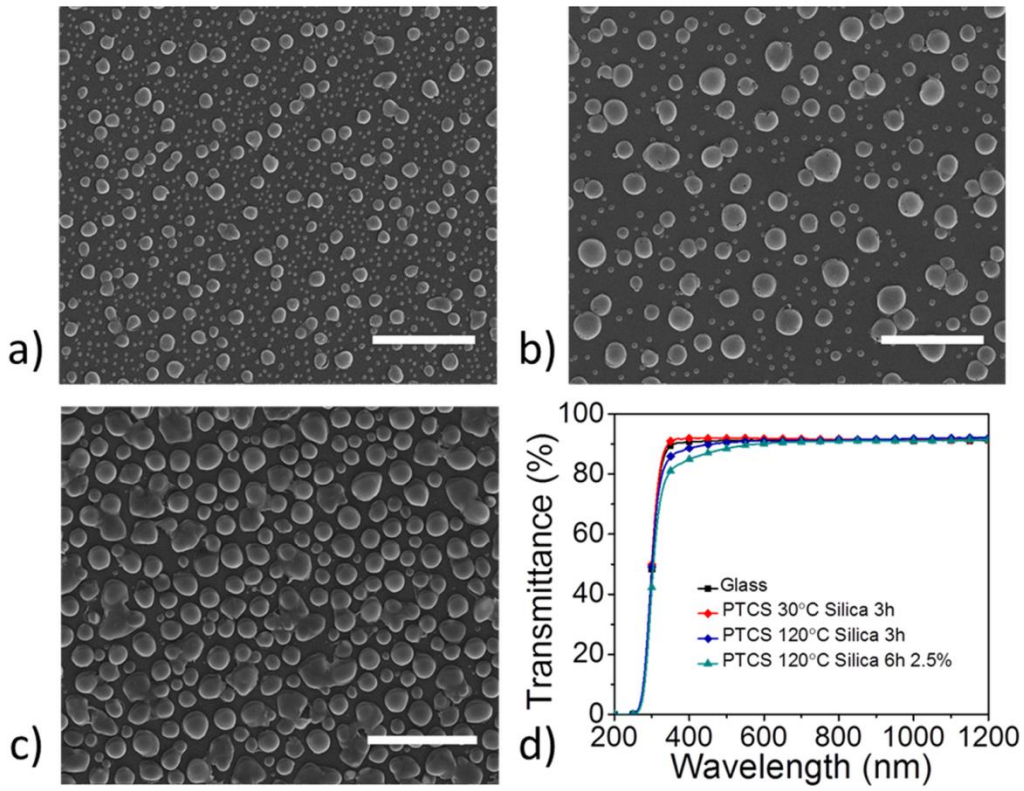

Figure 3.8: SEM images of several arrays of hollow silica half-nanospheres formed on dehydrated and PTCS-modified glass substrates and upon various TEOS hydrolysis conditions: (a) PTCS-modified glass: 1 h PTCS deposition at 30°C and under ca. 130 Torr / TEOS hydrolysis step: 3 h exposure (room temperature, under ca. 100 Torr) to an atmosphere saturated in water, ammonia (20% w/v ammonium hydroxide solution) and TEOS vapors. Scale bar: 1 µm; (b) PTCS-modified glass: 1 h PTCS deposition at 30°C and under ca. 130 Torr / TEOS hydrolysis step: 6 h exposure (room temperature, under ca. 100 Torr) to an atmosphere saturated in water, ammonia (diluted ammonium solution: 2.5%) and TEOS vapors. Scale bar: 1 µm; (c) PTCS-modified glass: 1 h PTCS deposition at 120°C and under ca. 130 Torr / TEOS hydrolysis step: 6 h exposure (room temperature, under ca. 100 Torr) to an atmosphere saturated in water, ammonia (diluted ammonium hydroxide solution: 2.5%) and TEOS vapors. Scale bar: 4 µm; (d) UV-Vis-NIR transmittance spectra of selected PTCS-modified and nanostructured glass substrates.

solution, room temperature, under *ca.* 100 Torr), and it can be observed that patterns of increasingly large PTCS aggregates tend to yield arrays of increasingly large half-nanospheres.

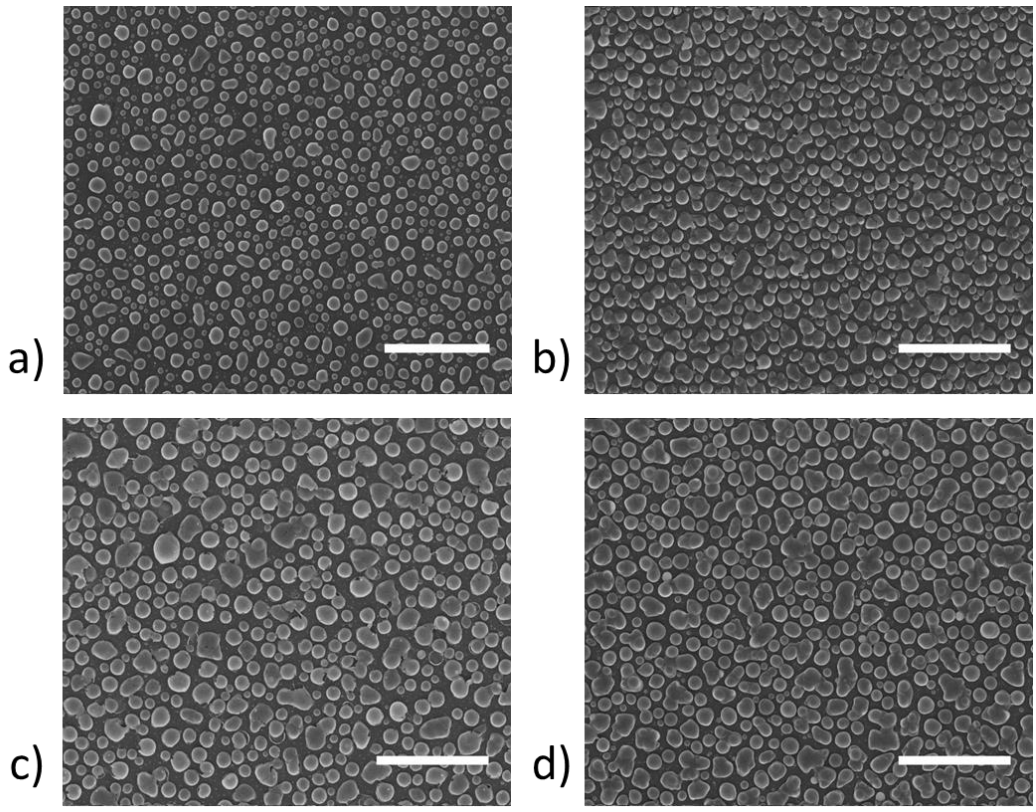

Figure 3.9: SEM images of several arrays of hollow silica half-nanospheres formed on dehydrated and PTCS-modified glass substrates and upon various TEOS hydrolysis conditions: (a) PTCS-modified glass: 1 h PTCS deposition at 60°C and under ca. 130 Torr / TEOS hydrolysis step: 3 h exposure (room temperature, under ca. 100 Torr) to an atmosphere saturated in water, ammonia (20% w/v ammonium hydroxide solution) and TEOS vapors. Scale bar: 2 µm; (b) PTCS-modified glass: 1 h PTCS deposition at 90°C and under ca. 130 Torr / TEOS hydrolysis step: 3 h exposure (room temperature, under ca. 100 Torr) to an atmosphere saturated in water, ammonia (20% w/v ammonium hydroxide solution) and TEOS vapors. Scale bar: 4 µm; (c) PTCS-modified glass: 1 h PTCS deposition at 60°C and under ca. 130 Torr / TEOS hydrolysis step: 6 h exposure (room temperature, under ca. 100 Torr) to an atmosphere saturated in water, ammonia (diluted ammonium hydroxide solution: 2.5%) and TEOS vapors. Scale bar: 2 µm; (d) PTCS-modified glass: 1 h PTCS deposition at 90°C and under ca. 130 Torr / TEOS hydrolysis step: 6 h exposure (room temperature, under ca. 100 Torr) to an atmosphere

saturated in water, ammonia (diluted ammonium hydroxide solution: 2.5%) and TEOS vapors. Scale bar: 4 μm.

In parallel, the particle-to-glass coverage increases as follows: *ca.* 26% on PTCS-modified glass produced at 30°C (Figure 3.8a), *ca.* 41.2% (mean surface area of *ca.* 0.026 μm^2) on PTCS-modified glass produced at 60°C (Figure 3.9a), and *ca.* 63.2% (mean surface area of *ca.* 0.133 μm^2) on PTCS-modified glass produced at 90°C (Figure 3.9b). In a parallel attempt to control the size of the silica half-nanospheres by changing the TEOS hydrolysis conditions under set PTCS-modified substrate parameters (1 h, 30°C, under *ca.* 130 Torr), we examined the effect of partial pressure in the ammonia precursor in the vapor phase by diluting the concentration of the aqueous ammonium hydroxide solution to only 2.5% w/v (here, we note that a longer TEOS hydrolysis time of 6 h is required to achieve nanostructures that are sufficiently thick to maintain their integrity during the chamber evacuation process, see Figures 3.6a and 3.6d). Comparing the SEM images in Figure 3.8a and 3.8b reveals that larger-sized silica half-nanospheres can be produced from the diluted ammonium precursor solution – an experimental result that emphasizes the importance of reaching a critical concentration of ammonia at the water droplet/air interface in order to effectively catalyze the TEOS hydrolysis step and immobilize individual water droplets in thin shells of SiO_2 at the early stages of condensation. Importantly, this alternative approach provides another means of controlling the size of the silica half-nanospheres independently of the substrate parameters. The SEM images in Figures 3.8b, 3.9c, 3.9d and 3.8c compare the patterns of silica half-nanospheres obtained from various PTCS-modified glass substrates

produced at 30°C, 60°C, 90°C, and 120°C, respectively, and with a lower partial pressure in the ammonia precursor (diluted ammonium hydroxide solution: 2.5% w/v) during the TEOS hydrolysis step. Here again, each substrate yields a different pattern of silica half-nanospheres under the fixed conditions of TEOS hydrolysis (6 h, 2.5% w/v ammonium hydroxide solution, room temperature, under *ca.* 100 Torr), and it can be observed that patterns of increasingly large PTCS aggregates tend to yield arrays of increasingly large half-nanospheres. In parallel, the particle-to-glass coverage increases as follows: *ca.* 27.3% on PTCS-modified glass produced at 30°C (Figure 3.8b), *ca.* 57.4% (mean surface area of *ca.* 0.063 μm^2) on PTCS-modified glass produced at 60°C (Figure 3.9c), *ca.* 63.6% (mean surface area of *ca.* 0.222 μm^2) on PTCS-modified glass produced at 90°C (Figure, 3.9d), and *ca.* 61.4% (mean surface area of *ca.* 0.481 μm^2) on PTCS-modified glass produced at 120°C (Figure 3.8c).

The UV-Vis-NIR transmittance spectra shown in Figure 3.8d indicates that the arrays of hollow silica half-nanospheres obtained from various PTCS-modified glass substrates affect the optical absorption of glass to a negligible extent. The minimal optical footprint of the nanostructured patterns can be explained on the basis of the thinness of the SiO_2 thin shells (20-30 nm) formed concurrently around the water droplets during the BF process. It is worth noting, however, that larger hollow silica half-nanospheres induce a slight decrease in the 300-600 nm wavelength range, likely due to enhanced Mie scattering as the size characteristics of the nanostructured pattern approach the wavelength of visible light. The excellent optical transmittance of the nanostructured

glass substrates suggests that the arrays of hollow silica half-nanospheres obtained via the BF approach will be amenable to a wide range of applications for which surface engineering and light management strategies are important parameters, including optoelectronic and photonic thin-film devices and light-harvesting modules. Specifically, we show that these hollow silica half-nanospheres can be used to construct transparent superhydrophobic surfaces. Benefit from decreased back scattering efficiency and increased light transport mean free path arise from the hollow nature,[129] and up to

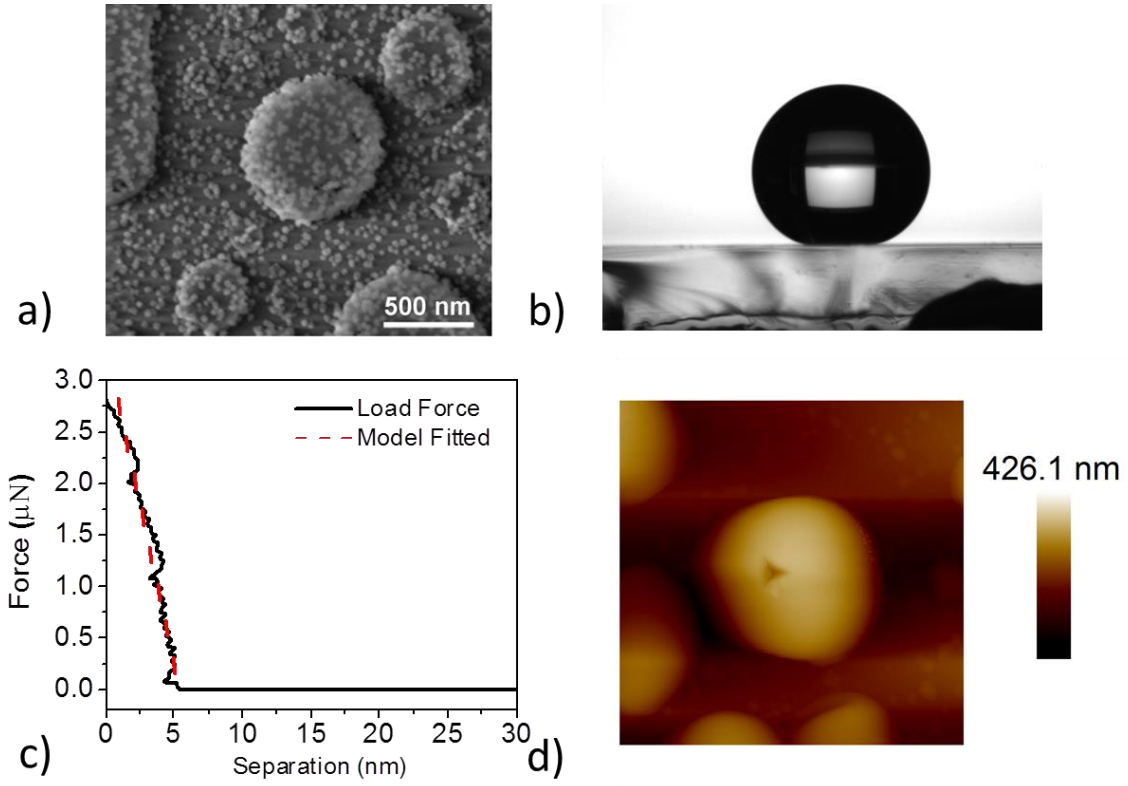

Figure 3.10: (a) SEM image of hollow silica half-nanosphere attached with 40 nm silica nanoparticles. (b) Photo of water droplet positioned on the transparent superhydrophobic surface. (c) Load force recorded during the nanoindentation process and fitted with Hertz model. (d) Deformation formed on the half-nanosphere.

micrometer sized roughness can be achieved with relatively high transparency, yielding a good compromise between superhydrophobicity and transparency without significant loss in surface roughness. Therefore, glass coated with hollow silica half-nanospheres of ~700 nm in diameter was used to obtain a hierarchical structured surface by electrostatically attaching 40-nm silica nanoparticles on the surface (Figure 3.10a, see details in Experimental Section). By modifying the surface of the resulting hierarchical structure with PTES, a transparent superhydrophobic surface with a static water contact angle of 155˚ (Figure 3.10b) and a sliding angle of 9˚ was achieved.

To check the mechanical property of the hollow silica half-nanosphere, nanoindentation characterization was performed by AFM. By fitting the linear part of the recorded load–force curve with the Hertz model, a Young's modulus of ~52 GPa was extracted (Figure 3.10c). Clear deformation was observed when the applied force exceeded the endure limitation of the half-nanosphere (Figure 3.10d). With the decent mechanical property of silica and the "direct-grown" protocol, the hollow half-nanosphere imparted transparent superhydrophobic surface is expected to yield improved mechanical properties. Considering large-scale applications, we also note that the patterns of silica half-nanospheres described throughout this work have been found to be continuous, homogenous and consistent between experiments. Our attempts to produce the same arrays on larger glass substrates (7.5 cm x 3 cm, scale limited only by the dimensions of the CVD chamber) have shown the same level of consistency.

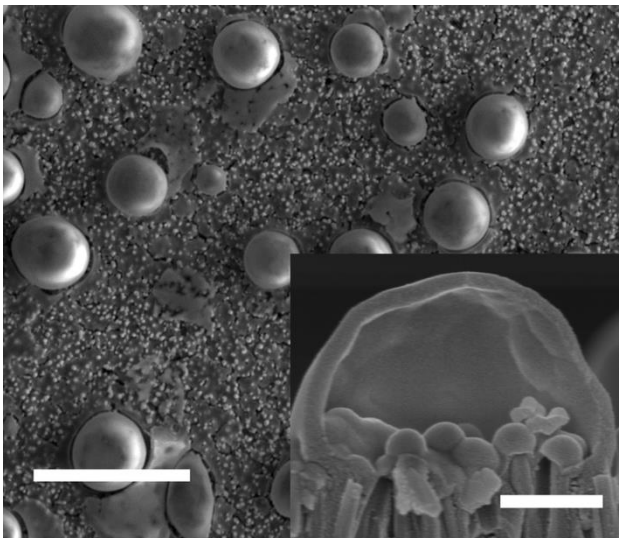

Figure 3.11: SEM image of an assembly of hollow silica half-nanospheres formed on a superhydrophobic array of perfluorodecyltriethoxysilane (PTES)-modified ZnO nanorods; Scale bar: 5 µm. Inset: Magnified cross-sectional SEM image of one of the apparent silica "nanodomes", emphasizing the hollow nature of the nanostructures; Scale bar: 500 nm.

Finally, to demonstrate that this approach to nanostructuring surfaces with hollow half-nanospheres can be applicable to a broader range of surfaces, including highly nanostructured substrates, we produced BF-templated arrays of hollow silica half-nanospheres on a superhydrophobic surface composed of ZnO nanorods. The SEM images in Figure 3.11 show the perfluorodecyltriethoxysilane (PTES)-modified ZnO nanorod arrays[157] onto which a pattern of hollow silica half-nanospheres has been induced (see details in Experimental Section). The SEM cross-section in the inset of Figure 3.11 confirms that the apparent silica "nanodomes" formed on PTES-modified ZnO nanorods are hollow, as expected from our prior observations of arrays of hollow silica half-nanospheres formed on various PTCS-modified glass substrates. Here, we note that it was not necessary to modify the PTES-functionalized ZnO nanorod arrays

further with PTCS aggregates, because of the highly nanostructured and hydrophobic nature of the substrate used, promoting the BF process.

3.4 Conclusion and Perspectives

In summary, we have shown how arrays of hollow silica half-nanospheres can be produced on various substrates via the BF approach. In our approach, forming the hollow nanostructured assemblies on glass substrates requires that the glass be modified with PTCS aggregates evenly distributed across the glass surface, and we discussed how PTCS aggregate size and density as well as aggregate-to-glass coverage influence the development of the BF-templated arrays of hollow silica half-nanospheres, including the size of the half-nanospheres. As the hollow nanostructured assemblies are produced in a concurrent BF process and hydrolysis step under a saturated atmosphere of TEOS precursor and ammonia vapors, the size of the half-nanospheres also depends on the local concentration of ammonia at the water droplet/air interface. A critical local concentration of ammonia is important to catalyze the TEOS hydrolysis step and immobilize individual water droplets in thin shells of silica at the early stages of condensation. Importantly, this second approach provides another means of controlling the size of the silica half-nanospheres independently of the substrate parameters.

Arrays of hollow silica half-nanospheres obtained via the BF approach may be amenable to a wide range of applications for which surface engineering and light management strategies are important parameters, such as optoelectronics, photonic devices and light-harvesting modules. In parallel, we note that condensation processes are of

fundamental interest, and that among all of the techniques known to date, our experimental protocol may provide a powerful tool for the ex-situ analyses of condensation in the very early stages. Future work will emphasize approaches that can improve the uniformity and periodicity of the hollow nanostructured assemblies on various surfaces and will examine the possibility to form arrays of half-nanospheres with functional metal oxides amenable to charge storage and solar energy conversion processes.

Chapter 4

Homo-Tandem Polymer Solar Cells with V_{OC} > 1.8 V for Efficient PV-driven Water Splitting

(Manuscript submitted to Advanced Materials)

4.1 Introduction

Bulk heterojunction (BHJ) polymer solar cells (PSCs) are set to deliver lightweight, mechanically flexible, solution-processable photovoltaic (PV) modules that could ultimately be produced via large-area, high-throughput and cost-efficient printing techniques.[9-10, 12, 172, 190, 238-239] For these reasons, PSCs are emerging as a promising alternative to their inorganic counterparts in the context of renewable energy generation. Considerable advances in the exploitation of new design principles and materials,[41, 59, 190, 240-242] optimization of BHJ morphology,[60, 243-246] better light management and improved interface materials,[61, 64, 66, 247-250] have launched power conversion efficiencies of single-junction PSCs past the 10% milestone. Despite rapidly increasing PCE values, the modest EQE of the photoactive layers remains one of the

major challenges towards improving the overall PCE and transitioning PSCs to the marketplace. Limited by optical interference effects and relatively modest carrier mobilities (10^{-3}-10^{-5} $cm^2(Vs)^{-1}$), optimum photoactive layer thicknesses for polymer-fullerene BHJ systems are in the range of 100-130 nm, resulting in incomplete light absorption in the visible spectrum (only 60-80% of incident photons are usually absorbed).[133-135] Multi-junction PSCs can circumvent some of these challenges by combining several subcells in series without the use of non-optimal, thick active layers. With the appropriate set of recombination layers and interlayer/electrode materials (and layer thicknesses),[148, 251-256] multi-junction PSCs absorb light more effectively and can yield PCEs >11%.[144, 148, 257] If enabled by PV modules, the conversion of solar energy to chemical energy – effectively stored, transported and used upon demand – provides a promising solution to the challenge of intermittent solar-to-electricity supply.[67, 150-151] PV-driven electrochemical water splitting produces hydrogen and oxygen fuels by dissociating water, while converting and storing solar energy with water as the only byproduct. While PV-driven electrochemical water splitting with solar-to-fuel efficiencies (η) >18% has been achieved in recent years with AlGaAs/Si tandem solar cells,[155] high production costs are currently limiting the transition of this concept to the large-scale, PV-driven production of chemical fuels. Because PSCs have the potential for large-area, high-throughput, cost-effective manufacturing, their use as PV modules to assist the electrochemical water splitting process could significantly reduce the costs of solar conversion to chemical energy.

In principle, a standard cell potential of 1.23 V is required for the dissociation of water under ambient conditions (25˚C); however, overpotentials due to reaction kinetics raise this threshold to 1.4–1.9 V.[67] To date, neither single-junction nor tandem high-efficiency (PCE >5%) PSC devices have provided sufficient open-circuit voltage (V_{OC}) to attain this 1.4-1.9 V threshold at their maximum power points.[145, 191, 255, 257-264] This high operating voltage can, however, be achieved with triple-junction PSC modules. For example, Janssen and coworkers recently demonstrated an estimated solar-to-fuel efficiency of ~ 3.1% with a triple-junction PSC composed of a high-bandgap polymer subcell stacked with two low-bandgap subcells of the same polymer (PCE 5.3%).[156] Because in multi-junction PSCs the photocurrent is limited by the lowest current among the photoactive layers, which is determined by the fraction and energy of photons available for each layer, stacking more subcells gradually decreases the overall photocurrent of the multi-junction PSC. As a result, in a PV-driven electrochemical cell, a higher voltage may not be able to compensate for a low photocurrent and thus, solar-to-fuel conversion efficiency may be reduced. Therefore, tandem PSCs composed of subcells that employ wide-bandgap polymers are inherently fit for PV-driven water splitting applications: a high photocurrent can be achieved while simple tandem PSC modules may have sufficient operating potential to drive the water splitting process.

In this report, we demonstrate high-voltage tandem and triple-junction PSCs by using one of the highest-V_{OC}, high-efficiency (PCE>7.5%; single cell) polymer donors in BHJs with fullerenes (e.g., $PC_{71}BM$), namely poly(benzo[1,2-*b*:4,5-*b'*]dithiophene–thieno[3,4-

c]pyrrole-4,6-dione)[133, 191-192, 245-246, 265-271] (PBDTTPD). While the efficiency of PBDTTPD-based single-junction PSCs is limited by incomplete optical absorption, we show that homo-tandem PSCs with MoO_3/ultrathin Al/ZnO intermediate recombination layers can achieve higher PCE values. As PCEs improve from 7.7% (single cell) to 8.35% for homo-tandem PSCs, the concurrent V_{OC} increase from 0.92V (single cell) to 1.84V enables the dissociation of water in an electrochemical cell with an estimated solar-to-fuel conversion efficiency of ~ 6%.

4.2 Experimental Section

4.2.1 Materials and Synthesis

Materials: Acetone, isopropanol, chloroform, methanol, chlorobenzene, 1-chloronaphthalene, zinc acetate dehydrate (⩾99.0%) and potassium hydroxide (⩾85%) (KOH) were purchased from Sigma-Aldrich. (6,6)-phenyl-C71-butyric acid methyl ester ($PC_{71}BM$) was purchased from Nano-C. Poly(3,4-ethylenedioxythiophene):poly(styrenesulfonate), namely PEDOT:PSS (Clevios™ P VP AI 4083) was purchased from Heraeus. Extran 300 detergent was purchased from EMD. All chemicals were used as received without further purification. Milli-Q water with a resistivity of >18.0 MΩ·cm was used. The polymer donor, poly(benzo[1,2-*b*:4,5-*b'*]dithiophene–thieno[3,4-*c*]pyrrole-4,6-dione) (PBDTTPD), was synthesized in our laboratories.

ZnO Nanoparticle Synthesis: ZnO nanoparticles were prepared using the sol-gel method described in prior published work.[272] The synthesis was carried out in a 500 mL round

bottom flask immersed in an oil bath. In general, zinc acetate dihydrate (2.95 g) was dissolved in methanol (125 mL) and heated at 60 °C; a solution of KOH (1.48 g) in methanol (65 mL) was added in 10 min to the zinc acetate dihydrate solution under vigorous stirring. With addition of KOH solution, the mixed solution became cloudy as zinc hydroxides formed, but became translucent ~ 5 min after complete addition of KOH. After ~1.5 h, the nanoparticles started to precipitate and the solution became turbid. The reaction was stopped after 2 h and 15 min and the solution was left to precipitate overnight. Thereafter, as much of the supernatant liquor as possible was removed, and the bottom precipitate was re-dispersed in 120 mL of methanol and decanted into four centrifuge tubes. After centrifuging at 4300 rpm, the supernatant was discarded and the nanoparticles were rinsed with fresh methanol. This centrifugation and rinsing step was repeated two more times, and the nanoparticles obtained were finally dispersed in methanol to form a 10 mg mL^{-1} solution. The solution was sonicated for 10 min each time before the spin-coating process.

4.2.2 Solar Cell Device Fabrication and Characterization

Substrate preparation: The solar cells were prepared on glass substrates with tin-doped indium oxide (ITO, 15 Ω sq^{-1}) patterned on the surface. The substrates were first scrubbed with diluted Extran 300 detergent solution to remove organic residues and then immersed in an ultrasonic bath of diluted Extran 300 for 15 min. Next, the samples were rinsed in flowing deionized water for 5 min and sonicated (Branson 5510) for 15 min each in successive baths of acetone and isopropanol. After a final 5 min rinse in

flowing deionized water, the samples were dried with pressurized nitrogen before being exposed to a UV-ozone plasma for 15 min. An aqueous solution of PEDOT:PSS (Clevios P VP AI 4083) was spin-cast at 4,000 rpm onto the substrates and baked at 140°C for 15 min. Immediately after baking the substrates, the samples were then transferred into a dry nitrogen glovebox (<3 ppm O_2) for active layer deposition.

Blend solution preparation: The blend solution was prepared in the glovebox using the PBDTTPD polymer donor and the $PC_{71}BM$ acceptor. The PBDTTPD polymer and $PC_{71}BM$ were dissolved in chlorobenzene containing 5% (by volume) of 1-chloronaphthalene (CN) additive, and the solutions were stirred overnight at 115°C. Optimized devices were prepared using a polymer:$PC_{71}BM$ ratio of 1:1.5 (by weight) with a concentration of 20 mg mL^{-1}.

Single-junction devices: The active layers were spin-cast on PEDOT:PSS-coated ITO substrates from the prepared blend solution at 90°C using a programmable spin coater from Specialty Coating Systems (Model G3P-8); various spin-coating speeds were used to get the required thickness. The samples were dried at room temperature for 1 h and then placed in a thermal evaporator for evaporation of a 7-nm layer of calcium at 0.3 Å s^{-1} and 120-nm layer of aluminum electrodes at 5 Å s^{-1} at a pressure less than $1x10^{-6}$ Torr. Following electrode deposition, samples underwent *J-V* testing.

Homo-tandem and triple-junction devices: After spin coating the first active layer, the samples were allowed to stay in a vacuum for 10 min to remove any residual solvent and then ZnO nanoparticles were spin-coated on top. Next, the samples were placed in

a thermal evaporator, a 1-nm layer of Al was evaporated at 0.3 Å s^{-1}, and a 16-nm layer of MoO_3 was evaporated at 0.3 Å s^{-1}; the next active layer was spin-coated. The same procedure was repeated for the triple-junction device. Next, the samples were placed in a thermal evaporator for evaporation of a 7-nm layer of calcium at 0.3 Å s^{-1} and a 120-nm layer of aluminum electrodes at 5 Å s^{-1} at a pressure less than $1x10^{-6}$ Torr.

Characterization of *J*-V, EQE and IQE: *J*-V measurements of solar cells were performed in a glovebox with a Keithley 2400 source meter and an Oriel Sol3A Class AAA solar simulator calibrated to 1 sun at AM1.5 G with a KG-5 silicon reference cell certified by Newport. EQE measurements were performed at a zero bias by illuminating the device with monochromatic light supplied from a Xenon arc lamp in combination with a dual-grating monochromator. The number of incident photons on the sample was calculated for each wavelength by using a silicon photodiode calibrated by NIST. After obtaining the EQE of the device, active layer absorption was calculated by subtracting the parasitic electrode absorptions simulated by transfer matrix modeling and the total device reflectance characterized by a Cary 6000i UV-Vis-NIR spectrophotometer equipped with an integration sphere. The IQE of the devices was inferred from the measured EQE of the devices and the calculated active layer absorption.

Optical characterizations: Optical transmittance measurements were performed with a Cary 6000i UV-Vis-NIR spectrophotometer under normal incidence. The reflectance measurements were performed using the same spectrophotometer equipped with an integration sphere. Optical characterization of the active layer was performed by an

ellipsometer and UV-Vis spectrometer equipped with an integrating sphere. Multi-sample analysis was used to extract a reliable refractive index of the active layer from the ellipsometer characterization. In general, Si substrates with different thicknesses of oxidized layers (from 2nm to <150 nm) were cleaned following the same steps as those for cleaning ITO substrates. The blended solution was spin-coated on top of the cleaned Si substrates, and the samples were characterized by an ellipsometer under various incident angles (Woollam M2000 spectroscopic ellipsometer). The obtained ellipsometric angles for each sample were fitted at the same time by a point-to-point model, where the same optical constants were assumed for all active layers. The Kramers-Kronig (KK) consistency was verified using the WVASE32 software. Extinction coefficients were extracted from the absorption of the active layer obtained from the integrating sphere, and film thickness was investigated by atomic force microscopy (AFM, Dimension Icon).

PV-driven Water Splitting Study: A platinum wire and nickel foam were used as cathode and anode for water electrolysis, respectively. The cathode and anode of the solar cell were connected to their corresponding electrodes via standard wires, and the solar cell was illuminated by a solar simulator (Peccell Technologies, PEC-L15) to mimic 100 mW cm^{-2} AM1.5G illumination. Two Keithley source meters were used to record the current and voltage generated by the solar cell when the depth of electrodes was varied inside the 1 M NaOH electrolyte cell.

4.3 Results and Discussion

Figure 4.1a shows the chemical structures of PBDTTPD and $PC_{71}BM$ used in the multi-junction PSC device assembly; Figures 4.1b and 4.1c show the device configurations of the homo-tandem and triple-junction PSCs examined in this study. The highly transparent

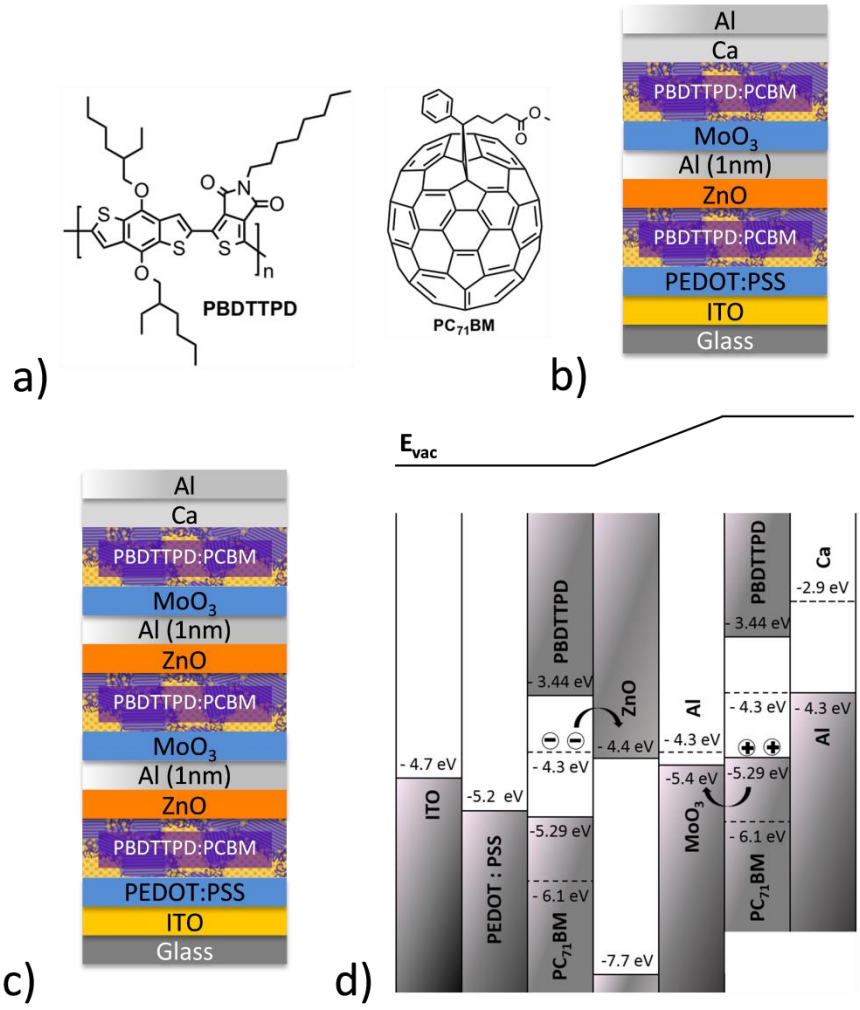

Figure 4.1: (a) Molecular structures of the polymer donor PBDTTPD and the fullerene acceptor $PC_{71}BM$ used in the multi-junction PSC devices. (b) Schematic homo-tandem device architecture. (c) Schematic triple-junction device architecture. (d) Simplified energy diagram of the homo-tandem PSC device architecture.

metal-oxide intermediate recombination layer that connects the PBDTTPD subcells in series consists of a sol-gel-derived ZnO electron transport layer (~20 nm) and a thermally evaporated MoO_3 hole transport layer (~16 nm). An ultra-thin evaporated layer of Al (~1 nm) improves the electric contact and provides additional recombination sites between the two metal-oxide layers.[252, 273] Figure 4.1d shows the schematic energy diagram for the homo-tandem PSC device.

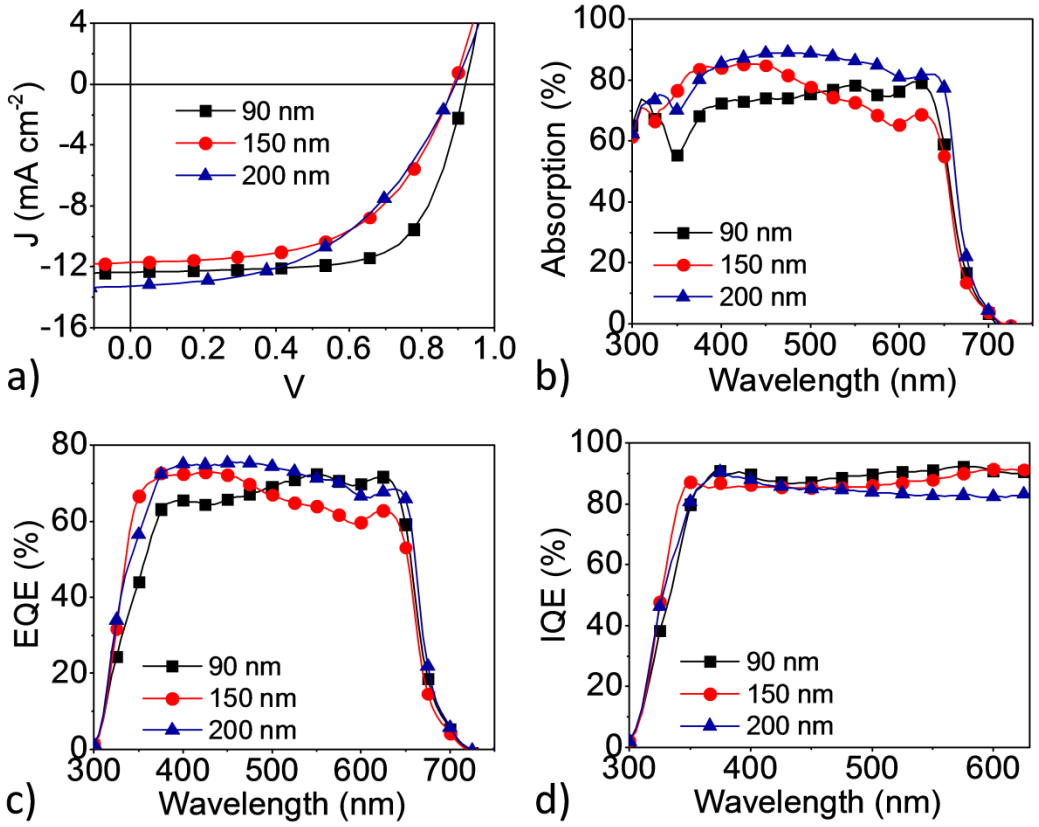

Figure 4.2: Single-junction PBDTTPD:$PC_{71}BM$ device performance with different active layer thicknesses: (a) *J*-V curves; (b) absorption spectra of the active layers; (c) external quantum efficiency (EQE); and (d) calculated internal quantum efficiency (IQE).

We began by investigating the PV performance of single-junction PBDTTPD:$PC_{71}BM$ PSCs with the standard device structure ITO/PEDOT:PSS/PBDTTPD:$PC_{71}BM$/Ca/Al (control devices). Figure 4.2a shows the *J-V* curve for single-junction PSCs with various active layer thicknesses under 100 mW cm^{-2} AM1.5G illumination, and Table 4.1 summarizes the results. Single-junction PBDTTPD:$PC_{71}BM$ devices reach PCEs as high as 7.75% at optimized active layer thicknesses of ~ 90 nm, fill-factors (FF) of 68%, V_{OC} values of 0.92 V and short-circuit currents (J_{SC}) of 12.37 mA cm^{-2}. We note, however, that the J_{SC} for optimized PBDTTPD single-junction PSCs does not match the maximum achievable current density of ~ 19 mA cm^{-2} that is obtained from integration of the photon flux under AM1.5G irradiation from 300 nm to 680 nm by assuming a 100% EQE device (see

Table 4-1: Single-junction PBDTTPD:$PC_{71}BM$ device performance with different active layer thicknesses.[a,b]

Active layer thickness	V_{OC}	J_{SC}	FF	Avg. PCE	Max. PCE
[nm]	[V]	[mA cm^{-2}]	[%]	[%]	[%]
90	0.92	12.37	68.14	7.46	7.75
150	0.88	11.73	55.90	5.74	5.81
200	0.89	13.27	49.02	5.64	5.80

[a] Average values across 10 devices (device area: 0.1 cm^2).
[b] Additional device statistics, including standard deviations, are shown in Figure 4.8.

Figure 4.3a). Because the internal quantum efficiency (IQE) for single-junction PBDTTPD solar cells at optimum active layer thickness is >90% (Figure 4.2d), the lower empirical J_{SC} results mainly from incomplete light absorption caused by limited active layer thickness, surface reflection and parasitic absorption. The spectral absorption of the single-junction PSC devices has been extracted from the total reflection spectrum (R) of

the devices by 100-R with subtraction of parasitic electrode absorptions, employing transfer matrix modeling,[274-275] and the results are shown in Figure 4.2b. Less than 80% of visible light is absorbed when the single-junction PSC device is at its optimized ~ 90-nm thickness. In single-junction PSC devices, the most straightforward approach to maximizing the absorption of the active layer, with the goal of increasing the device J_{SC}, is to increase active layer thickness. However, the existence of a pronounced interference effect in the active layer (Figure 4.3b) causes a significant reduction in absorption in the longer-wavelength region (>500 nm) if the active layer thickness departs from its optimized point (even upon slight increases), resulting in a drop in J_{SC}. Overall, single-junction PBDTTPD devices achieve lower PCEs when the active layer thickness is increased from 90 nm to 150 nm (Figure 4.2; Table 4.1), accompanied by a

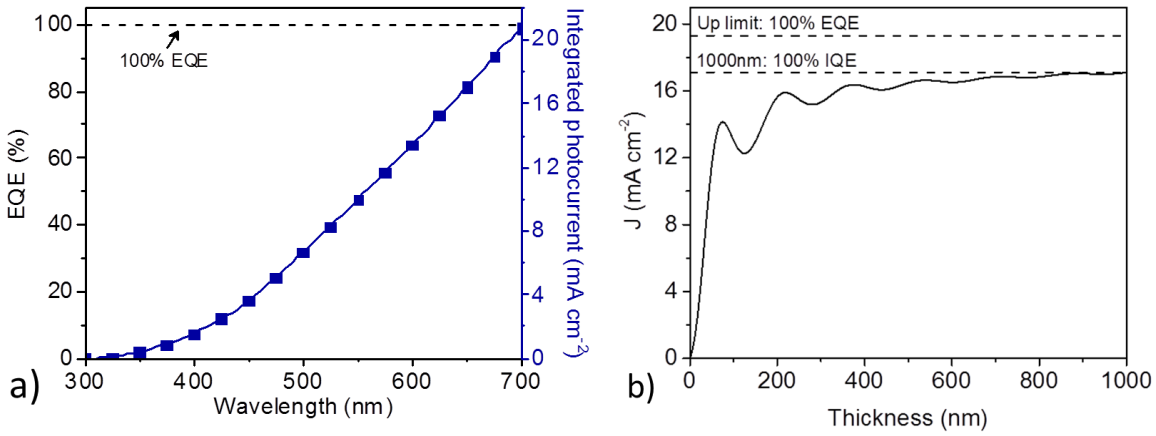

Figure 4.3: (a) Integrated photocurrent for AM1.5G irradiation from 300 nm to 680 nm by assuming a 100% EQE device. (b) Simulated short current vs. active layer thickness by assuming a 100% IQE device. The waveform of the curve illustrates the strong interference effect inside the active layer.

significant degradation in FF to 55% and a drop of J_{SC} from 12.4 mA cm^{-2} to 11.7 mA cm^{-2}. Comparing the spectral absorption of single-junction PSC devices with 90-nm and 150-nm active layers (Figure 4.2b), the thicker layer shows a more pronounced spectral absorption in the shorter-wavelength region (<500 nm; >80% photons absorbed) and reduced absorption in the longer-wavelength region (>500 nm; <75% photons absorbed). Because the photon flux density under AM1.5G illumination is more intense in the longer-wavelength region, the more pronounced absorption in the shorter-wavelength range does not compensate for the loss associated with the reduced absorption in the longer-wavelength region, and as a result, the total photocurrent produced by the single-junction PSC device is slightly reduced. As shown in Figure 4.3b, the J_{SC} of single-junction PSCs can increase further in relation to active layer thickness when the active layer is markedly thicker than its optimum value. For example, by increasing the active layer thickness to 200 nm, the J_{SC} increases to 13.2 mA cm^{-2}, which represents a 6.4% enhancement compared to 12.4 mA cm^{-2} in the optimized device. In parallel, the mean active layer absorbance reaches ~ 85% with a peak absorption at 88%. We note, however, that the corresponding single-junction PBDTTPD device (200-nm thick active layer) shows a significantly lower FF of 49%, and in turn, a considerably lower PCE of 5.8%. The significant degradation in FF with increased active-layer thickness results from higher yields of bimolecular charge carrier recombination in the thicker active layers, commonly linked to ineffective carrier extraction in the absence of a sufficient built-in electric field in thicker-than-optimal devices[133] and to the modest

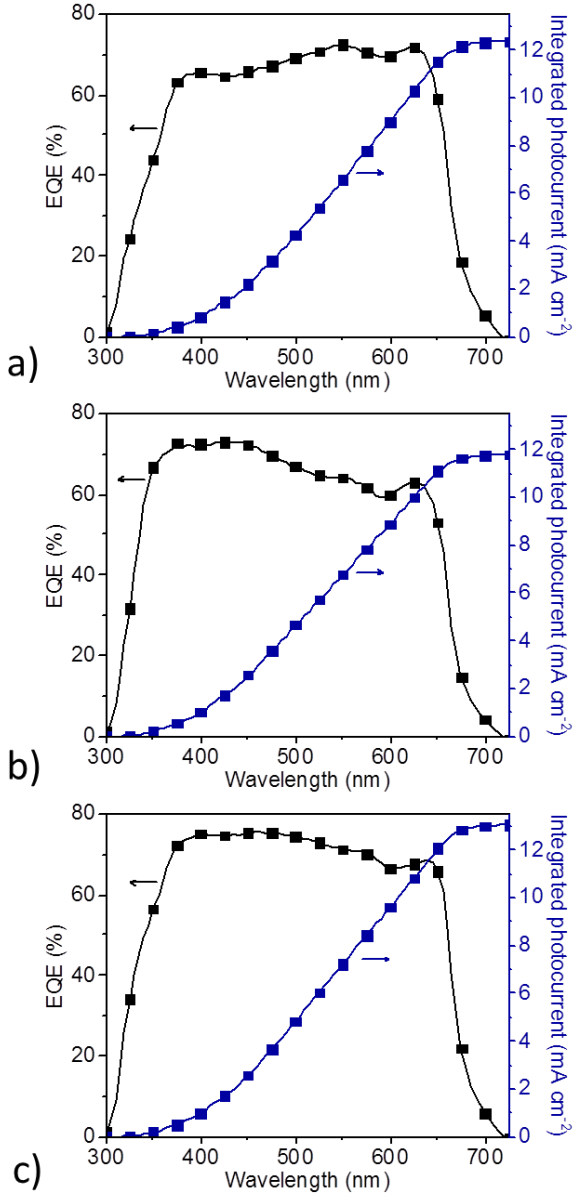

Figure 4.4: External quantum efficiency and corresponding integrated photocurrent for a single junction PBDTTPD:$PC_{71}BM$ device with active layer in thicknesses of (a) 90 nm, (b) 150 nm and (c) 200 nm.

hole mobilities of the polymer donors.[276] The EQE of the single-junction PSC devices was also measured to confirm the variations of J_{SC} with active layer thickness. Figure 4.4 shows that the photocurrents integrated from the experimental EQEs are in agreement

(±0.2 mA cm^{-2}, ±1.5%) with the J_{SC} values reported in Table 4.1. As shown in Figure 4.2c, a single-junction device with a 90-nm active layer has an average EQE of ~ 67% in the visible range, peaking to 72% at 550 nm. Meanwhile, single-junction devices with thicker active layers follow a similar trend with visible changes in the absorption spectrum. Figure 4.2c also shows that single-junction PSC devices with 200-nm active layers produce more photocurrent than those with 90-nm active layers. The IQE of single-junction PSCs with different active layer thicknesses was calculated based on the absorption spectrum of the active layer shown in Figure 4.2b and on the experimental EQE shown in Figure 4.2c; Figure 4.2d shows the IQE for the single-junction PSC devices. At the optimized active layer thickness of 90 nm, the single-junction PBDTTPD device shows an average IQE of ~ 90% across most of the visible spectrum, but with an active layer of 200 nm, the IQE decreases to ~ 83%, confirming that the carrier recombination yields increase and that carrier extraction at short-circuit is less effective in the thicker active layer. In short, improving light absorption by increasing active layer thickness in single-junction PBDTTPD devices is not an effective approach to improving the overall PCE. However, the construction of multi-junction PSCs composed of several identical PBDTTPD subcells with optimum, relatively thin active layers may provide a strategy to enhance light absorption while preserving the high charge carrier extraction efficiency and fill factor in each subcell to ultimately improve the PCE.

Homo-tandem PSCs constructed from two identical PBDTTPD subcells were first investigated for their ability to improve the PCE achieved with single-junction PSC devices.

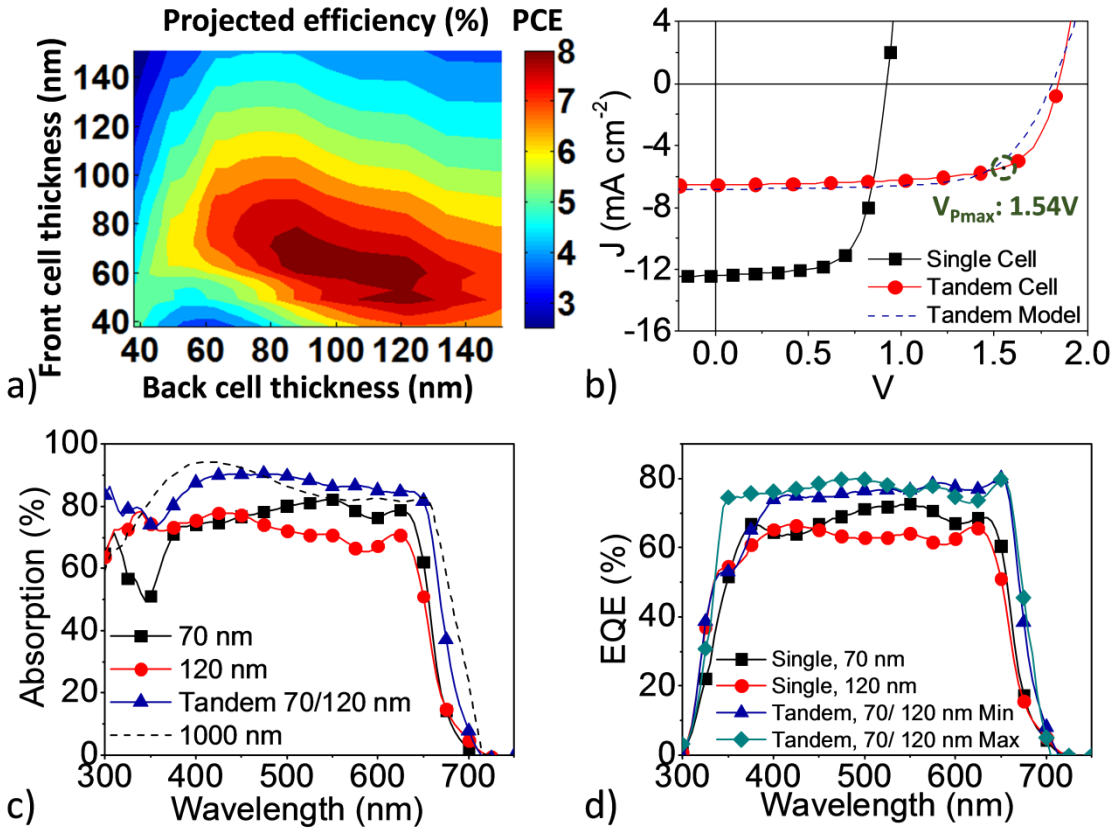

Figure 4.5: (a) Power conversion efficiency (PCE) of homo-tandem PSCs predicted from optical and electrical modeling. (b) *J*-V curves of optimized single-junction and homo-tandem PSCs superimposed with that predicted from optical and electrical modeling for the homo-tandem device with an optimized subcell thickness combination (70-nm front cell, and a 120-nm back cell). (c) Absorption of a single-junction PSC device with 70-nm and 120-nm active layers, a control single-junction PSC device with an "unrealistically" thick active layer of 1,000 nm (simulated via transfer matrix modeling), and an optimized homo-tandem solar cell with a 70-nm front cell and a 120-nm back cell. (d) EQE of single-junction devices with 70-nm and 120-nm active layers along with their calculated "total EQEs" for the optimized tandem device inferred from the spectral absorption and IQE of the combined subcells (Note: the minimum total EQE is calculated by multiplying the spectral absorption of the tandem device with the IQE derived for a 120 nm single-junction device; the maximum total EQE is calculated by multiplying the spectral absorption of the tandem device with the IQE derived for a 70 nm single-junction device).

Figure 4.1b shows a breakdown of the layers used to construct the device structure—ITO/PEDOT:PSS/PBDTTPD:$PC_{71}BM$/ZnO/Al/MoO_3/PBDTTPD:$PC_{71}BM$/Ca/Al. Combined optical and electrical modeling was used to predict the optimal combination of active

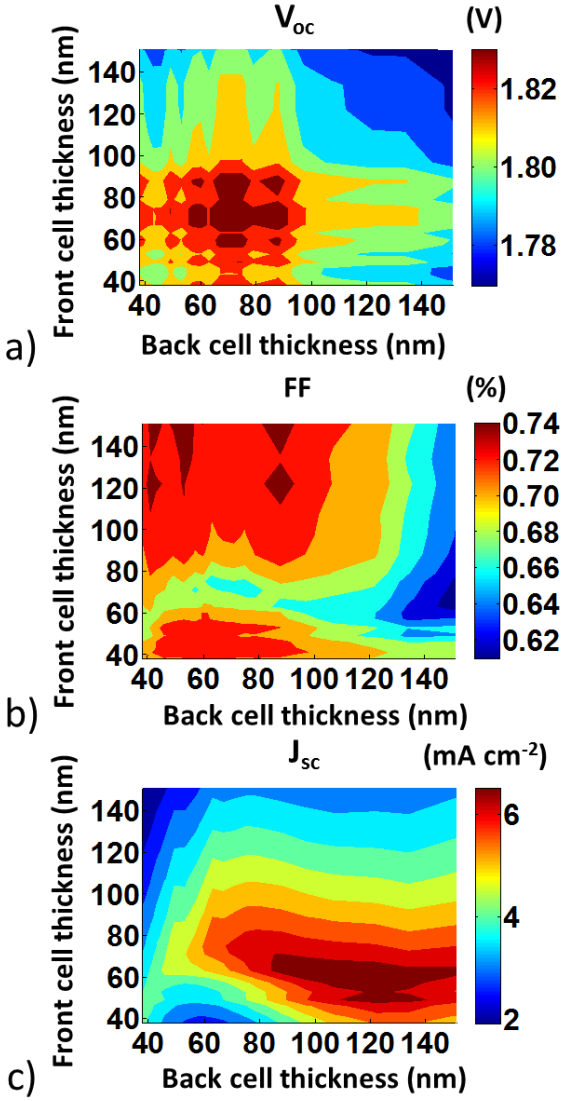

Figure 4.6: Predicted figures of merit for a PBDTTPD:$PC_{71}BM$ homo-tandem solar cell from combined optical and electrical modeling (a) V_{OC}, (b) FF and (c) J_{SC}.

layer thickness for the front and back subcells (see details in the Experimental Section);[255, 277-278] Figures 4.5a and 4.6 describe the modeling analyses, emphasizing the specific subcell thickness combinations amenable to the best tandem PCEs. Naturally, the two identical subcells in a homo-tandem solar cell have overlapping absorption. Because there is an exponential decrease in transmitted light intensity with increasing active layer thickness (aside from interference effects), an accurate description of the optical parameters (n, k) of the active layer is necessary to produce accurate modeling results for the tandem device. To achieve this, optical characterization of the active layer was done via ellipsometry and UV-Vis spectrometry (instrument equipped with an integrating sphere). Multi-sample analysis was used to extract a reliable refractive index for the active layer via ellipsometry (see details in the Experimental Section).[279-281] Because highly absorptive films are not well characterized by reflection ellipsometry,[280, 282] the extinction coefficient was extracted from consideration of the absorption of the active layer obtained from the integrating sphere and the film thickness estimate obtained from several AFM measurements. Combining the optical parameters of the active layer in the transfer matrix model, we produced the transmission, reflection and absorption spectra for BHJ active layers coated on glass. Comparing the computed spectra to those obtained experimentally via UV-Vis spectrometry (Figure 4.7), we find that the experimental and modeling results correlate well, confirming the reliability of the optical parameters extracted for the PBDTTPD-based BHJ films. In these combined optical and electrical modeling analyses, the electronic properties of the tandem subcells

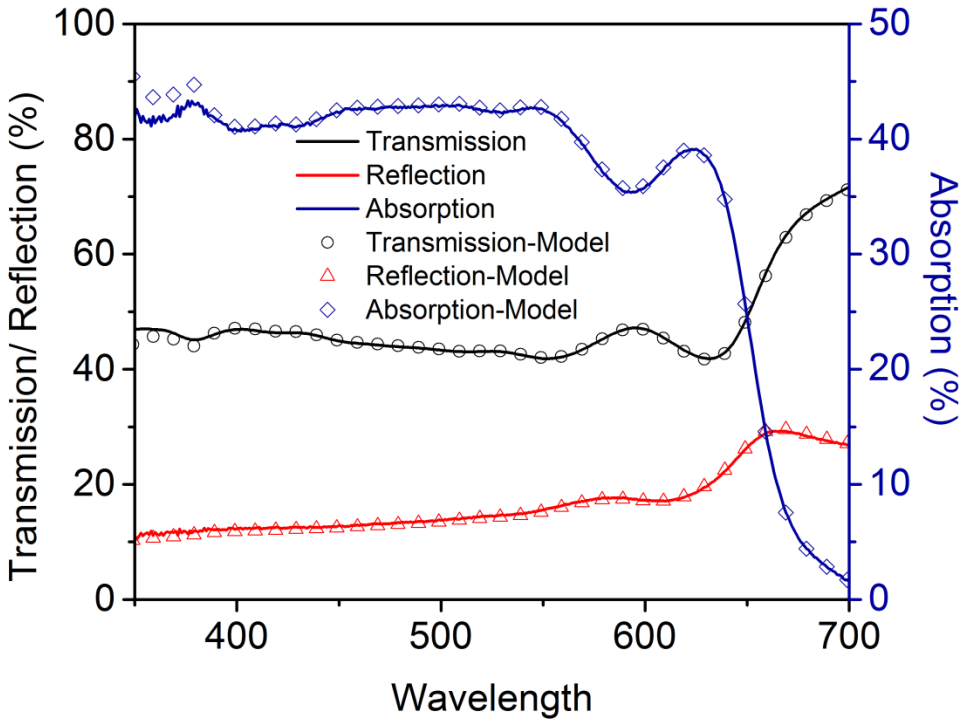

Figure 4.7: Transmission, reflection and absorption spectra measured by UV-Vis spectrometer for a 68-nm PBDTTPD:$PC_{71}BM$ photoactive layer spin-coated on glass. Transmission, reflection and absorption spectra obtained from transfer-matrix modeling are also present to show the consistency between experimental and modeling results.

(for a set active layer thickness), including the IQE and the shape of the *J-V* characteristics, are assumed to be consistent with those experimentally measured in the single-junction PSC devices. In Figures 4.5c and 4.5d, we represent the measured absorption and EQE characteristics for two single-junction PSC devices with set active layer thicknesses of 70 nm and 120 nm; the model indicates that front and back cells with those thickness values are amenable to the highest expected tandem PCEs (Figure 4.5a and 4.6). The expected photocurrent produced by the combined subcells in the homo-tandem device was obtained from optical modeling using transfer matrix

formalism: the photocurrent generated by each subcell can be calculated knowing the IQE and the simulated single-cell photocurrent (for a set active layer thickness); after compensating for the measured *J-V* characteristics of the single-junction devices with the calculated photocurrent in subcells, the *J-V* characteristics of the subcells can be effectively extrapolated. Using Kirchhoff's laws, and assuming no losses at the recombination contact, the *J-V* characteristics for the homo-tandem PSCs can be inferred for specific thickness combinations. Following this approach for multiple subcell thickness combinations, as shown in Figure 4.5a, our combined optical and electrical modeling analyses predict PCEs >8.0% for various subcell thickness combinations: in general, favorable subcell combinations are 60-80 nm for the front cell and 90-130 nm for the back cell; the details of the predicted V_{OC}, J_{SC} and FFs for the PBDTTPD-based homo-tandem PSCs are shown in Figure 4.6.

Table 4-2: PV performance figures for the constructed and predicted (via combined optical and electrical modeling) homo-tandem and triple-junction PSCs with optimized subcell thickness combinations.[a,b]

PBDTTPD	V_{OC}	J_{SC}	FF	Avg. PCE	Max. PCE
Device	[V]	[mA cm^{-2}]	[%]	[%]	[%]
Tandem Cell	1.84	6.54	69.3	8.13	8.35
Tandem Model	1.81	6.82	67.5		8.35
Triple Cell	2.75	3.95	68.15	7.27	7.42
Triple Model	2.71	4.59	65.8		8.21

[a] Average values across 10 devices (device area: 0.1 cm^2).
[b] Additional device statistics, including standard deviations, are provided in Figure 4.8.

Homo-tandem PSCs were constructed with optimal subcell thickness combinations chosen in the ranges established from the combined optical and electrical modeling analyses: those with PCEs >8.0% under 100 mW cm^{-2} AM1.5G illumination. All constructed homo-tandem PSC devices were found to achieve PCE values >8.0%, in agreement with the modeling analyses. Using a thickness combination of 70 nm for the front cell and 120 nm for the back cell, a champion homo-tandem device PCE value of 8.35% was obtained—a result consistent with the predicted PCE for this specific combination of subcell thicknesses; the experimental *J-V* curves for the constructed homo-tandem PSCs and those predicted by the model are superimposed in Figure 4.5b, and the figures of merit of the corresponding homo-tandem device are presented in Table 4.2 for comparison. The experimental results show that the constructed homo-tandem PSCs combine high FF (69.3% vs 67.5% predicted by the model) and V_{OC} (1.84V vs 1.81V) values, and a slightly lower J_{SC} (6.54 mA cm^{-2} vs 6.82 mA cm^{-2}) value. With PCEs >8% and a V_{OC} >1.8V, tandems composed of identical PBDTTPD subcells are the highest-efficiency, high-voltage tandem PSCs reported to date.[145, 255, 257, 264, 283] Other groups have observed slightly higher experimental FF values;[255, 284-285] although here, experimental and predicted values remain in good agreement. Despite some modest differences between experimental and modeling results,[286] the figures of merit for the constructed homo-tandem PSCs remain well aligned with the predicted values. Importantly, the high FF of ca. 70% achieved in the constructed homo-tandem PSC and the V_{OC} value of 1.84V corresponding to the sum of two single-junction device V_{OC}s

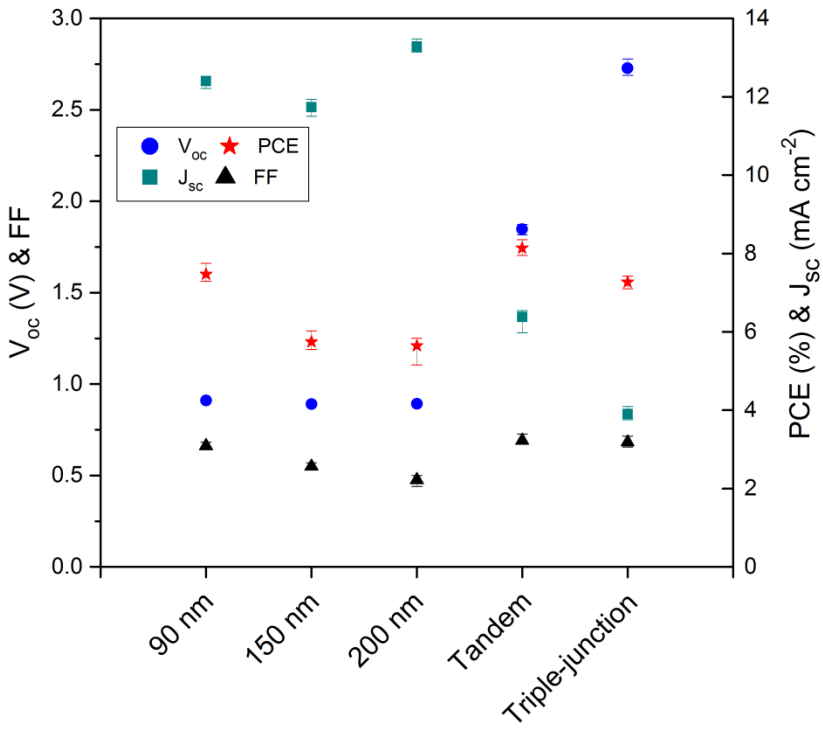

Figure 4.8: Statistical PV performance for single-junction, tandem and triple-junction PBDTTPD devices. For each result, the markers denote the average values and the error bars show the standard deviation across 10 devices.

(0.92+0.92=1.84V) indicate that the sol-gel ZnO/ultra-thin Al/MoO_3 intermediate recombination layer serves as an excellent connection layer between the two identical PBDTTPD subcells of the homo-tandem device, efficiently preventing parasitic losses at the recombination contact. The homo-tandem PSCs achieve a 0.6% increase in PCE over their optimized single-junction device counterparts (8.35% vs. 7.75%, respectively), confirming that the construction of multi-junction PSCs composed of several identical PBDTTPD subcells with optimum, relatively thin active layers is an effective approach to improving the overall PCE. J_{SC} values in the homo-tandem device are higher than half of those for an optimized 90-nm single-junction device and are responsible for the

improved PCE (see Tables 4.1 and 4.2); in parallel, the V_{OC} is exactly double that of the homo-tandem device. The experimental J_{SC} of the homo-tandem is 6.54 mA cm^{-2}, while half of the experimental J_{SC} of an optimized 90-nm single-junction PSC device is ~6.2 mA cm^{-2}, corresponding to a ~0.34 mA cm^{-2} increment in photocurrent (J_{SC} increased by 5.4%). Here, the J_{SC} increase can be explained by the enhanced light absorption induced by the subcells connected in series, with no significant impact on the efficiency of charge-carrier extraction across the homo-tandem device. To confirm that the homo-tandem PSC device absorbs light more effectively, its spectral absorption was inferred via the same method described earlier for the single-junction PSC device. Figure 4.5c shows the spectral absorption of single-junction PSC devices with active layer thicknesses equivalent to those of the front and back cells of the champion homo-tandem PSC (70 nm and 120 nm, respectively). The homo-tandem device shows a 5–10% improvement in light absorption (averaged across the visible spectrum) compared to single-junction PSC devices with either 70-nm or 120-nm active layers, confirming the benefits of using a homo-tandem device architecture with optimized subcell thicknesses.

Because the constructed homo-tandem PSCs have two identical subcells exactly overlapped in absorption, the EQE of each subcell cannot be independently characterized for each of the subcells via light bias analyses, and therefore, we estimated the “total EQE” to further confirm the improvement in light absorption in the homo-tandem device. To estimate the “total EQE” of the homo-tandem PSC, the overall

spectral absorption of the homo-tandem device was multiplied by the IQEs inferred for single-junction PSC devices with active layer thicknesses equal to those used in the tandem front and back cells (70 nm and 120 nm, respectively);[146, 148] these results are presented in Figure 4.5d together with the measured EQE of the control single-junction PSC devices. Following this approach, we provide the upper and lower limits of the estimated "total EQE" for the homo-tandem PSC device. In the control single-junction PSC devices, the experimental EQE remains <70% across the visible spectrum, but interestingly, an EQE of over 75% is estimated for the homo-tandem device, which is consistent with the idea that the homo-tandem device absorbs light more effectively across the visible range.

Next, we examined the potential for further PCE increments via a triple-junction PSC device approach, using the same ZnO/Al/MoO_3 interconnection layer between the three subcells. Figure 4.1c illustrates the triple-junction device configuration adopted for this purpose—ITO/PEDOT:PSS/PBDTTPD:PC_{71}BM/ZnO/Al/MoO_3/PBDTTPD:PC_{71}BM//ZnO/Al/ MoO_3/PBDTTPD:PC_{71}BM/Ca/Al. Following the same approach as depicted for the homo-tandem PSCs, we first examined the expected PV performance of the triple-junction devices using combined optical and electrical modeling (Figure 4.9a and Figure 4.10). The model predicts PCEs as high as 8.21% for a triple-junction PSC composed of a 50-nm front cell, a 65-nm middle cell and a 120-nm back cell. We then constructed the corresponding triple-junction device, demonstrating a champion device with a PCE of 7.42%, FF of 68.15%, J_{SC} of 3.95 mA cm^{-2} and a remarkably high V_{OC} of 2.75V, which is the

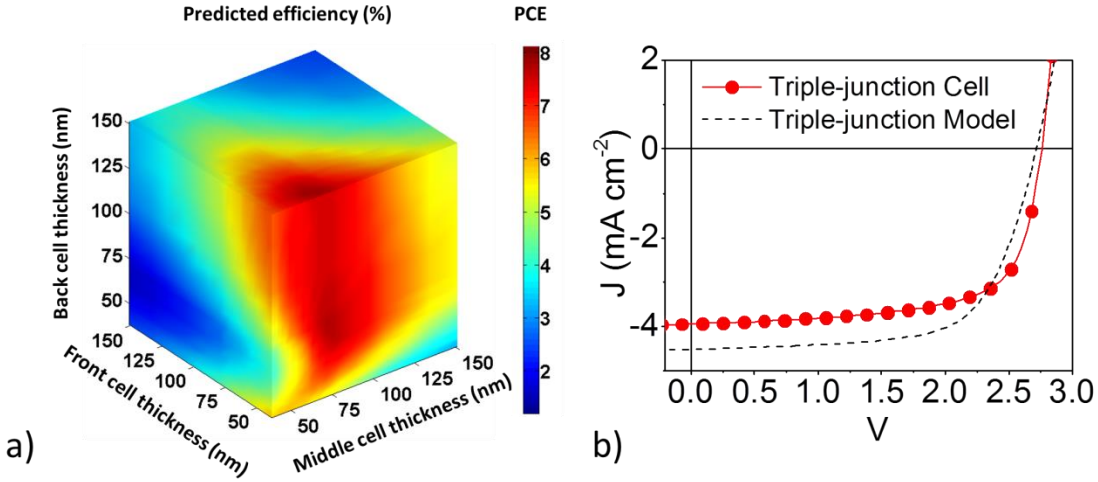

Figure 4.9: (a) PCE of triple-junction PSCs predicted from combined optical and electrical modeling. (b) *J*-V curves of constructed and model predicted triple-junction PSC with an optimized thickness combination (50-nm front cell, a 65-nm middle cell and a 120-nm back cell).

largest V_{OC} achieved with a triple-junction PSC device to date. The *J-V* curves for the constructed and predicted triple-junction PSCs are shown in Figure 4.9b; the figures of merit collected from the experimental data are compared to those obtained from the model in Table 4.2. Here, we note that neither predicted nor experimental results indicate that the PBDTTPD triple-junction device can be amenable to higher PCEs than those of the homo-tandem PSCs. To support this result, Figure 4.5c compares the spectral absorption for a control single-junction PSC device with an "unrealistically" thick active layer of 1,000 nm (simulated via transfer matrix modeling) to the overall spectral absorption in the champion homo-tandem PSC device of 8.35% PCE. From this simple comparison, we can see that the overall spectral absorption of the homo-tandem PSC is similar to that of the 1,000-nm simulated, control single-junction PSC, indicating that the

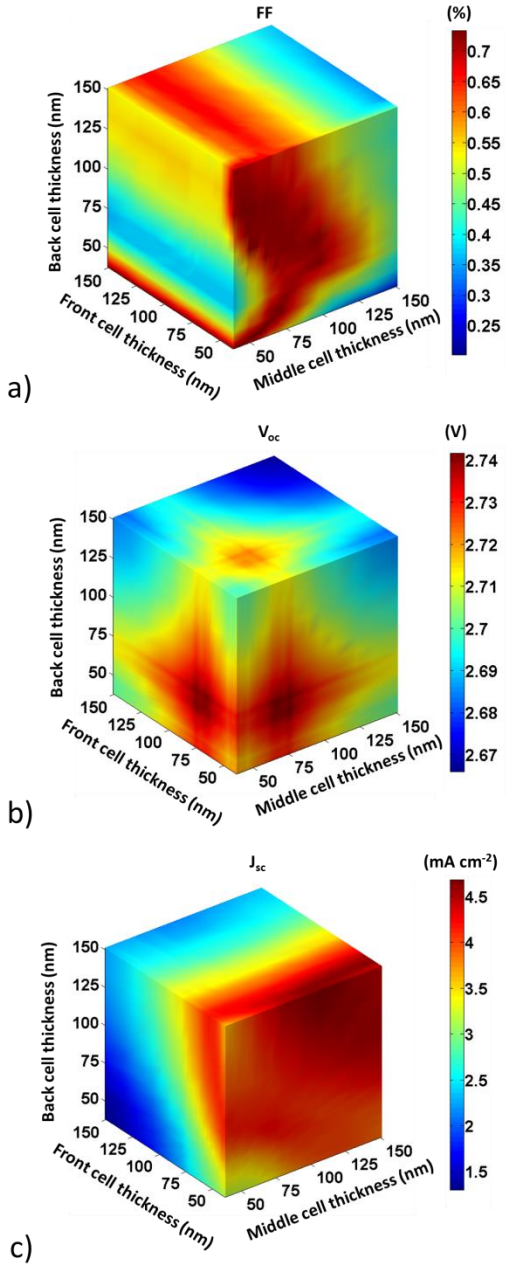

Figure 4.10: Predicted figures of merit for a PBDTTPD:$PC_{71}BM$ triple-junction solar cell from combined optical and electrical modeling (a) V_{OC}, (b) FF and (c) J_{SC}.

upper limit of light absorption is nearly achieved in the optimized homo-tandem device. The near-complete absorption achieved with the homo-tandem PSC leaves only limited leeway to further increase absorption by the addition of a third subcell, and the second

recombination layer in the triple-junction PSC device is likely to result in additional parasitic absorption and limit overall device efficiency.

As depicted in Figure 4.5b, PBDTTPD homo-tandem PSCs yield high operating voltages of 1.54 V at their maximum power point, providing sufficient potential for the dissociation of water and the evolution of hydrogen and oxygen in a standard electrochemical cell; combined with a current density of 5.4 mA cm^{-2}, homo-tandem PSCs can be expected to yield respectable solar-to-hydrogen conversion efficiencies (η).

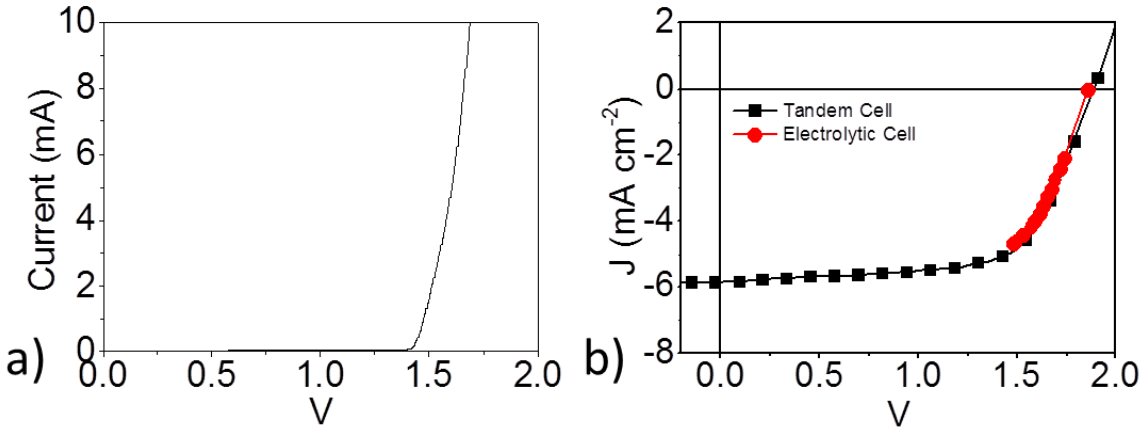

Figure 4.11: (a) Overall I-V characteristics of water splitting in the two-electrode cell configuration used in this study for demonstration; a platinum wire and nickel foam are used as cathode and anode for water electrolysis, respectively, with a 1 M NaOH solution as the electrolyte. (b) *J*-V curves of the homo-tandem solar cell measured using a water electrolysis cell with different surface area ratios of the solar cell and the water splitting electrodes using a source measurement unit.

Using platinum and nickel foam as hydrogen and oxygen evolution electrodes, a potential of ~ 1.5 V is required for electrochemical water splitting in a 1 M NaOH aqueous solution (Figure 4.11a), which is within reach of the maximum power point of the homo-tandem PSC device (1.54 V). We then connected our homo-tandem PSC to an

electrochemical cell, immersing the platinum and nickel foam electrodes in a 1 M NaOH electrolyte solution (Figure 4.12a). When the homo-tandem PSC is irradiated by 100 mW cm^{-2} AM1.5G illumination, the evolution of hydrogen from the platinum electrode can easily be observed, demonstrating that PBDTTPD homo-tandem PSCs can effectively split water. It has been shown that the operating voltage of the solar cell driving the water dissociation can be changed by varying the surface area ratio of the solar cell and the water splitting electrodes, such that the *J-V* characteristics of the solar cell match those of the electrochemical cell more favorably (Figure 4.11b).[155-156] Based on these

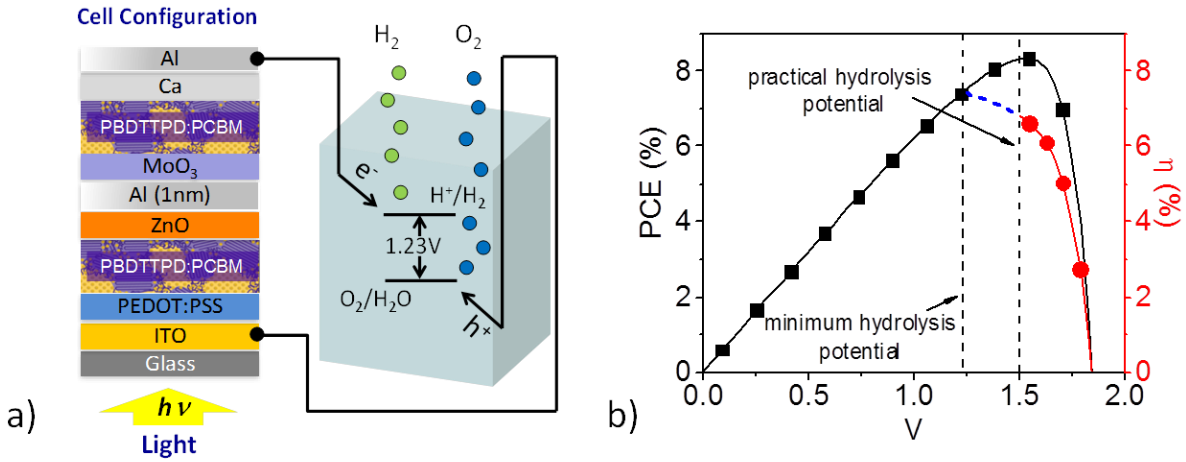

Figure 4.12: (a) Schematic PV-driven electrochemical water splitting study. (b) PCE of the homo-tandem PSC (measured via source-measurement unit) and estimated solar-to-hydrogen conversion efficiency (η) at various operating voltages.

empirical considerations and assuming a reasonable faradaic efficiency of 90% for the water splitting cell used in this study,[152] the solar-to-hydrogen conversion efficiency can be estimated as $\eta = PCE_{solar\ cell} \times (E^{0}_{H2O}/V_{solar\ cell}) \times 90\%$ and plotted versus the operating voltage of the homo-tandem solar cell (Figure 4.12b); as shown in Figure 4.12b,

PBDTTPD homo-tandem PSCs can be used to achieve solar-to-hydrogen conversion efficiencies of 6.1% at an operating voltage of 1.5 V.

4.4 Conclusion

In summary, we showed that PBDTTPD can be used to construct efficient, high-voltage (>1.8V) homo-tandem and triple-junction PSCs with MoO_3/ultrathin Al/ZnO intermediate recombination layers. Homo-tandem PSCs absorbed light more effectively and achieved higher PCE values (8.35% vs 8.3% for the model) than single-junction PSC devices (7.7%). As we examined the potential of triple-junction PSCs for further PCE increments, we found that conventional triple-junction PSCs composed of identical PBDTTPD subcells may not yield higher PCE values (7.4% vs 8.2% for the model) than their homo-tandem counterparts. With PCEs >8%, a V_{OC} >1.8V and operating voltages of ~ 1.5 V at maximum power point, PBDTTPD homo-tandem PSCs are the highest-efficiency, high-voltage tandem PSCs reported to date and these can be used in PV-driven electrochemical water splitting cells —demonstrating solar-to-fuel conversion efficiencies of ~6%.

Chapter 5

Hybrid Colloidal Quantum Dot-Polymer Bulk Heterojunction Tandem Solar Cells

(Manuscript is in preparation)

5.1 Introduction

Colloidal quantum dot (CQD) solar cells, in light of their low-cost manufacturing,[287-289] size-tunable bandgap,[290-291] and the possibility to harness "hot" electrons by multiple exciton generation,[292-296] have attracted immense interest in photovoltaic technologies[297-303] and are considered as the next-generation of photovoltaics.[304-305]

Since the early reports of Schottky-type CQD devices with a power conversion efficiency (PCE) of >1%,[306-309] tremendous efforts have been made to improve the device performance by either improving the electronic properties of the quantum dot solid[310-317] or enhancing the driving force for charge extraction with alternative device architectures.[301-303, 318-320] Among them, the depleted-heterojunction CQD (DH-CQD) device showed signification improvement in device performance by taking advantage of

a corrected light absorption position and extended depletion region to the CQD solid, with a certified efficiency of 7% PCE[297] and a world record efficiency of 8.5% PCE[300] reported for DH-CQD devices. However, keeping in mind the reported diffusion length in the range of 10–100 nm for CQD solids[321-322] in the quasi-neutral region and a required film thickness of ~1 μm for >90% light absorption,[323] there is still a long way to go to fully realize the ultimate potential of CQD solar cells. On the other hand, working hard to only improve the optical and electronic properties of CQDs or engineering the interface between the electrode and the CQD solids to achieve enhanced charge extraction might result in limited success. Construction of multi-junction CQD devices by stacking multi layers of CQD with complementary light absorption provides a promising way to reach a compromise between light absorption and charge extraction. Compared to single-junction solar cells, the multi-junction device structure also offers a roadmap to improve the ultimate PCE beyond the Shockley–Queisser limit.[149]

Unfortunately, CQD tandem solar cells reported by two research groups did not show impressive enhanced performance,[324-326] even though the bandgap combination of the two CQD layers is at a theoretical optimal value. The low performance mainly comes from the low fill factor (FF) (<0.5). This is not surprising, considering the layer-by-layer solution process for the CQD layer. As a result, the first processed CQD layer and the following deposited recombination layer need to go through multiple solution treatments during the deposition of the second CQD layer, increasing the risk of the under layers being affected, especially considering that the vigorous ligand exchange

process usually results in cracks in the CQD film.[327-328] On the other hand, possessing the same advantage of tuning the bandgap by molecular engineering and simple one-time spin-on principle as compare to CQD solar cells, highly efficient polymer multi-junction solar cells with FFs of 76–80% have been reported.[329] However, limited by the availability of efficient near infrared polymer materials, the efficiency of multi-junction PSCs is also facing a bottleneck. With this in mind, combining the CQD with a suitable polymer absorber to make hybrid inorganic–organic tandem solar cell can open the path to obtaining efficient devices by taking advantages from both materials.

Here we present the fabrication of hybrid inorganic–organic tandem solar cells by combining CQDs and polymers. Different device architectures were also tested with the aim to improve the PCE.[330-332]

5.2 Experimental Section

5.2.1 Materials and Synthesis

Acetone, isopropanol, chloroform, methanol, chlorobenzene, 1-chloronaphthalene, acetonitrile (ACN), 3-mercaptopropionic acid (MPA), zinc acetate dehydrate (⩾99.0%) and potassium hydroxide (⩾85%) (KOH) were purchased from Sigma-Aldrich. (6,6)-phenyl-C71-butyric acid methyl ester ($PC_{71}BM$) was purchased from Nano-C. Poly(3,4-ethylenedioxythiophene):poly(styrenesulfonate), namely PEDOT:PSS (Clevios™ P VP AI 4083) was purchased from Heraeus. TiO_2 paste ws purchased from Dyesol (18-NRT, particle size 20 nm). Extran 300 detergent was purchased from EMD. All chemicals were used as received without further purification. Milli-Q water with a resistivity of >18.0

MΩ·cm was used. The polymer donor, poly(benzo[1,2-*b*:4,5-*b'*]dithiophene–thieno[3,4-*c*]pyrrole-4,6-dione) (PBDTTPD), was synthesized in our laboratories. The oleic acid covered PbS CQD solution (50mg/ml in octane) was received from Prof. Sargent's group. ZnO nanoparticles were synthesized using the sol-gel method described in last chapter, and dispersed in methanol to form a 10 mg mL^{-1} solution. The ZnO solution was sonicated for 10 min each time before the spin-coating process.

5.2.2 Solar Cell Device Fabrication

Substrate preparation: The solar cells were prepared on glass substrates with pre-patterned fluorine-tin-oxide (FTO, 15 Ω/sq, Xin Yan LTD.) or tin-doped indium oxide (ITO, 15 Ω sq^{-1}). The substrates were first scrubbed with diluted Extran 300 detergent solution to remove organic residues and then immersed in an ultrasonic bath of diluted Extran 300 for 15 min. Next, the samples were rinsed in flowing deionized water for 5 min and sonicated (Branson 5510) for 15 min each in successive baths of acetone and isopropanol. After a final 5-min rinse in flowing deionized water, the samples were dried with pressurized nitrogen before being exposed to a UV-ozone plasma for 15 min. For ITO substrates, an aqueous solution of PEDOT:PSS (Clevios P VP AI 4083) was spin-cast at 4,000 rpm and baked at 140°C for 15 min. Immediately after baking the substrates, the samples were then transferred into a dry nitrogen glovebox (<3 ppm O_2) for active layer deposition. For FTO substrates, TiO_2 nanoparticles diluted in ethanol (1:3 by weight) were spin spin-coated on the substrate at 1,500 rpm, followed by heating at 80°C for 5 min and 500°C for 30 min on a hotplate. The TiO_2-coated substrates were

cooled to room temperature and immersed into a 120 mM $TiCl_4$ solution in DI water at 70°C for 30 min, then the substrates were rinsed with DI water and heated at 500°C for 30 min. All of the procedures for the TiO_2-coating step were carried out in ambient air conditions and the substrates were stored in the nitrogen glovebox after TiO_2 coating.

Blend solution preparation: The blend solution was prepared in the glovebox using the PBDTTPD polymer donor and the $PC_{71}BM$ acceptor. The PBDTTPD polymer and $PC_{71}BM$ were dissolved in chlorobenzene containing 5% (by volume) of 1-chloronaphthalene (CN) additive, and the solutions were stirred overnight at 115°C. Optimized devices were prepared using a polymer:$PC_{71}BM$ ratio of 1:1.5 (by weight) with a concentration of 20 mg mL^{-1}.

Conventional single-junction CQD solar cell fabrication: The CQD film was formed through layer-by-layer deposition of PbS CQDs on TiO_2 coated FTO substrate. For each layer, CQDs solution was cast onto the substrates through a 0.2-μm filter and spin-coated at 2,500 rpm for 10 s. Next, ca. 300 μl of MPA in ACN solution (1% in volume) was used to fully cover the CQD surface and kept on the surface for 3 s; the solution was then removed by spinning the sample at 2,500 rpm for 5 s. Finally, the CQD surface was rinsed by casting and spinning ACN at 2,500 rpm, and this step was repeated twice: 5 s for the first and 10 s for the second rinse. The CQD deposition procedure was repeated three times. The CQD-coated substrate was then transferred to a vacuum evaporator inside the nitrogen glovebox. The evaporator chamber was evacuated to 1×10^{-6} Torr for the deposition of 16 nm MoO_x at a rate of 0.3 Å/s, followed by 10 nm of gold (0.2

Å/s), and 80 nm of Ag (0.2 Å/s for the first 10 nm and 5 Å/s for the following 70 nm) as an electrode.

Inverted single-junction CQD solar cell fabrication: The CQD film was formed on PEDOT:PSS-coated ITO substrate in the same fashion as mentioned before. Only one layer of CQD was coated. After that, ZnO solution was spin-cast on top of the CQD film at 1,000 rpm and the whole sample was baked on a hot plate at 100°C for 10 min. The sample was then transferred to a vacuum evaporator inside the nitrogen glovebox. The evaporator chamber was evacuated to 1×10^{-6} Torr for the deposition of 7 nm Ca at a rate of 0.3 Å/s, followed by 120 nm of Al (0.2 Å/s for the first 10 nm and 5 Å/s for the following 110 nm) as an electrode.

Conventional single-junction PSC fabrication: The polymer active layer was spin-cast on PEDOT:PSS-coated ITO substrate at 800 rpm from the prepared blend solution heated at 90°C. The sample was dried at room temperature for 1 h and then transferred to a vacuum evaporator inside the nitrogen glovebox. The evaporator chamber was evacuated to 1×10^{-6} Torr for the deposition of 7 nm Ca at a rate of 0.3 Å/s, followed by 120 nm of Al (0.2 Å/s for the first 10 nm and 5 Å/s for the following 110 nm) as an electrode.

Inverted single-junction PSC fabrication: ZnO solution was spin-coated on the ITO substrate at 5,000 rpm in ambient condition and then transferred into the nitrogen glovebox. The polymer active layer was then spin-cast on the substrate at 800 rpm from the prepared blend solution heated at 90°C. The sample was dried at room temperature

for 1 h and then transferred to a vacuum evaporator inside the nitrogen glovebox. The evaporator chamber was evacuated to 1×10^{-6} Torr for the deposition of 16 nm MoO_x at a rate of 0.3 Å/s, followed by 10 nm of gold (0.2 Å/s), and 80 nm of Ag (0.2 Å/s for the first 10 nm and 5 Å/s for the following 70 nm) as an electrode.

Bottom-illuminated hybrid tandem solar cell fabrication: A conventional or inverted CQD subcell without deposition of electrode was transferred to a vacuum evaporator inside the nitrogen glovebox. The evaporator chamber was evacuated to 1×10^{-6} Torr, and then 16 nm MoO_x at a rate of 0.3 Å/s followed by 1 nm Al at a rate of 0.2 Å/s was deposited for the conventional CQD subcell, and 1 nm Al at a rate of 0.2 Å/s followed by 16 nm MoO_x at a rate of 0.3 Å/s was deposited for the inverted CQD subcell. After that, the polymer active layer was spin-cast on the sample at 800 rpm from the prepared blend solution heated at 90°C. The sample was dried at room temperature for 1 h and then transferred to a vacuum evaporator inside the nitrogen glovebox. The evaporator chamber was evacuated to 1×10^{-6} Torr. Finally, the bottom-illuminated conventional hybrid tandem solar cell was completed by deposition of 16 nm MoO_x and 80 nm of Ag as electrode, and the bottom-illuminated inverted hybrid tandem solar cell was completed by deposition of 7 nm Ca and 120 nm of Al as electrode.

Top-illuminated hybrid tandem solar cell fabrication: A conventional or inverted CQD subcell without deposition of electrode was transferred to a vacuum evaporator inside the nitrogen glovebox. The evaporator chamber was evacuated to 1×10^{-6} Torr, and then 16 nm MoO_x at a rate of 0.3 Å/s followed by 1 nm Al at a rate of 0.2 Å/s was

deposited for the conventional CQD subcell, and 1 nm Al at a rate of 0.2 Å/s followed by 16 nm MoO_x at a rate of 0.3 Å/s was deposited for the inverted CQD subcell. After that, the polymer active layer was spin-cast on the sample at 800 rpm from the prepared blend solution heated at 90°C. The sample was dried at room temperature for 1 h and the ZnO solution was spin-cast on the sample with inverted CQD subcell at 5,000 rpm. After that, the sample was transferred to a vacuum evaporator inside the nitrogen glovebox. The evaporator chamber was evacuated to 1×10^{-6} Torr. Finally, a transparent electrode with the structure of MoOx(20 nm)/Au(1 nm)/Ag(7 nm)/MoOx(20 nm)/LiF(50 nm) was deposited on top of the sample to complete the device.

Electrical and optical characterization of solar cells and thin films: *J*-V measurements of solar cells were performed in a glovebox with a Keithley 2400 source meter and an Oriel Sol3A Class AAA solar simulator calibrated to 1 sun at AM1.5 G with a KG-5 silicon reference cell certified by Newport. The absorption of the thin film was characterized by a Cary 6000i UV-Vis-NIR spectrophotometer equipped with an integration sphere. The sheet resistance of the transparent conductive electrode was measured by four-point probe.

5.3 Results and Discussion

The materials used throughout this study are shown in Figure 5.1a. A PbS quantum dot that is initially capped by oleic acid and then ligand-exchanged to 3-mercaptopropionic acid in solid-state is used for the CQD subcell. A conjugated polymer donor, poly(benzo[1,2-*b*:4,5-*b'*]dithiophene–thieno[3,4-*c*]pyrrole-4,6-dione)[133, 191-192, 245-246, 265-

[271] (PBDTTPD), in conjunction with the fullerene acceptor [6,6]-phenyl-C_{70}-butyric acid methyl ester ($PC_{71}BM$), forms the bulk heterojunction polymer subcell. The optical density spectra of the two active layers are shown in Figure 5.1b. Depending on the size of the quantum dot, the CQD active layer can have a broad tunable absorption spectrum covering from the visible to the infrared range (700–1500 nm). PbS quantum dots with first excitonic absorption at 950 nm were used in this study as they give the best device

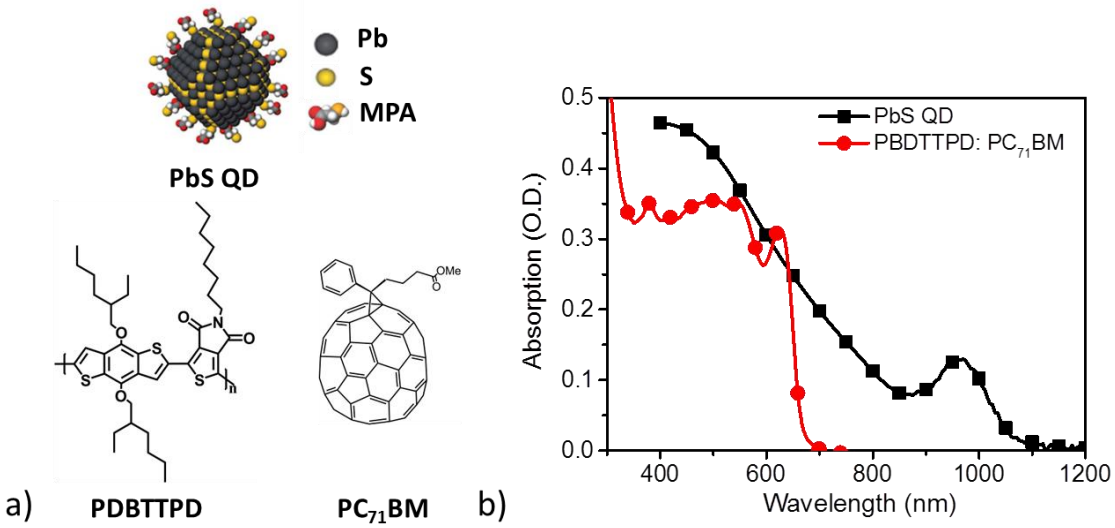

Figure 5.1: (a) Chemical structure of used materials, including a PbS quantum dot after ligand exchange, conjugated polymer donor PBDTTPD and $PC_{71}BM$ as the fullerene acceptor. (b) Optical density of PbS CQD film and PBDTTPD: $PC_{71}BM$ active layers.

performance for DH-CQD device. In addition to the satisfactory absorption in the near infrared (NIR) range, the CQD active layer also shows strong absorption in the visible range. Relatively, conjugated polymers usually show strong and sharp absorptions in the visible range. The bulk heterojunction active layer formed by blended PBDTTPD: $PC_{71}BM$

solution shows effective absorption in the range 300–700 nm and totally transmits in the NIR range.

Considering the broader absorption of CQD active layer as compared to the polymer active layer, a device structure with CQD subcell deposited on top of the polymer subcell should be adopted in the hybrid tandem device. In this way, the CQD active layer can be made thick enough to absorb most of the near infrared light transmitted from the polymer subcell. However, exposure of the polymer active layer to the common processing and ligand exchange solvent used in CQD deposition results in significant morphological roughening and degraded polymer solar cell performance, which makes the monolithic stacking of the CQD subcell on top of the polymer subcell more challenging. Hence, we first tried to integrate the hybrid tandem device by stacking the polymer subcell on top of the CQD bottom subcell.

Regarding the device configuration adopted in the CQD subcell, either the transparent conductive electrode or the reflective metal electrode can be used as the anode in the hybrid tandem device. The former would be classified as a conventional hybrid tandem, while the later would be referred to as an inverted hybrid tandem. For historical reasons, the concept of conventional and inverted device configuration is reversed for CQD solar cell and polymer solar cell. To clarify, the definition of conventional and inverted device configuration is the same for the CQD subcell and the hybrid tandem in this study, and is inverted for the polymer subcell.

The conventional hybrid tandem was first constructed with the device structure shown in Figure 5.2a. A conventional CQD subcell prepared by layer-by-layer deposition of CQD on TiO_2-coated FTO glass was jointed with a solution-processed PBDTTPD:$PC_{71}BM$ inverted polymer subcell through a thermally evaporated 16-nm MoO_x and 1-nm Al film. The MoO_x/ultra-thin Al film functions as a recombination layer that physically separates

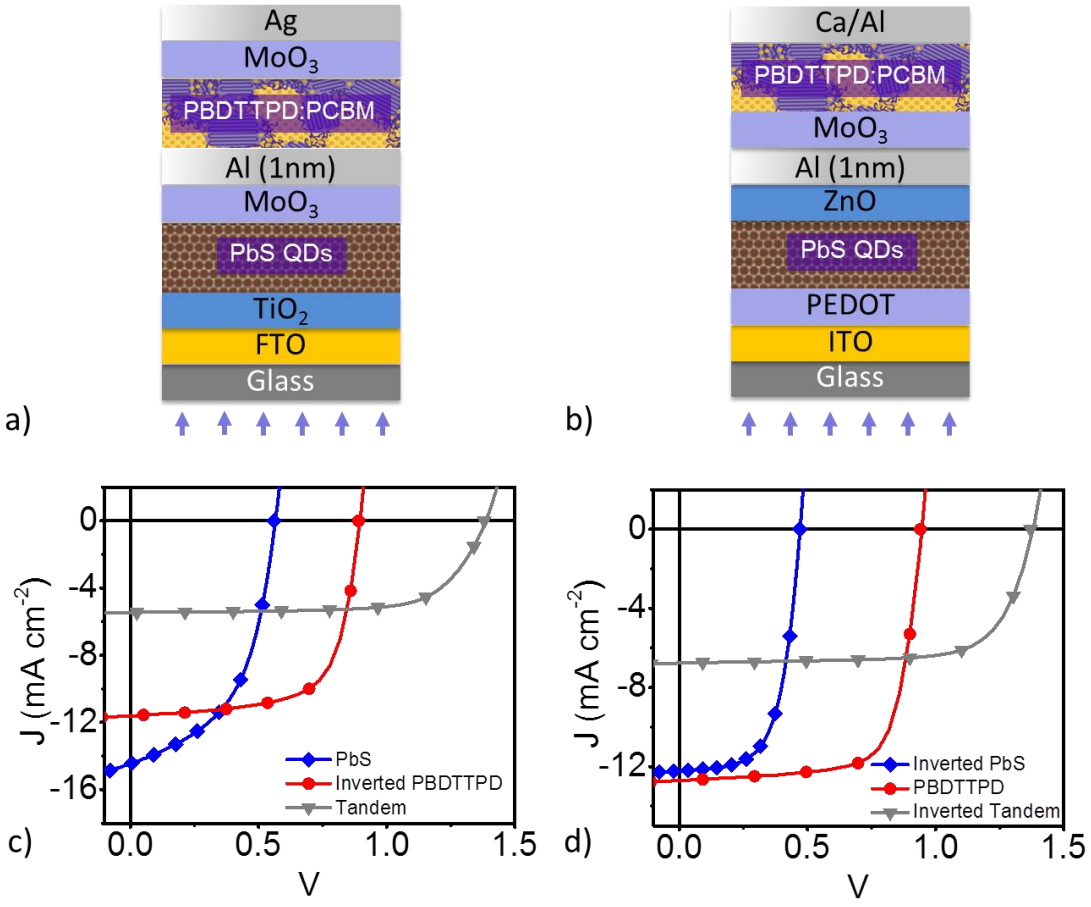

Figure 5.2: Schematic device structure for (a) bottom-illuminated conventional hybrid tandem and (b) bottom-illuminated inverted hybrid tandem. *J*-V characteristic curves of the optimized hybrid tandem devices and single-junction devices for (c) bottom-illuminated conventional hybrid tandem and (d) bottom-illuminated inverted hybrid tandem.

and electrically connects the two subcells. The device was completed by thermally evaporating 16 nm MoO_x and 80 nm Ag on top of the polymer active layer. The current–voltage (*J*–V) characteristics curve for the conventional hybrid tandem with optimized recombination of active layer thicknesses is shown in Figure 5.2c along with the performance of single-junction CQD and polymer devices. The figures of merit for hybrid tandem and single-junction devices are summarized in Table 5.1. The single-junction CQD device with an active layer thickness of 120 nm showed a short current density (J_{sc}) of 14.46 mA cm^{-2} with an open voltage (V_{oc}) of 0.56 V, and a fill factor (FF) of 50.4%, resulting in a PCE of 4.1%. The inverted PBDTTPD:PC_{71}BM single-junction device processed on a ZnO nanoparticle coated ITO glass substrate has an active layer thickness of 120 nm, and shows a J_{sc} of 11.6 mA cm^{-2} with V_{oc} of 0.89 V and FF of 67.2%. The PCE for this device was 7%. The V_{oc} of the conventional tandem reached 1.38 V, representing 95% of the sum of the V_{oc} values of the individual cells, along with an FF as high as 70.2%. This indicates an insignificant electrical loss at the connection interlayer, and that MoO_x/ultra-thin Al works as an efficient recombination layer. However, the J_{sc} for the optimized conventional hybrid tandem device is only 5.4 mA cm^{-2}, resulting in an unimpressive PCE of 5.3%. The low J_{sc} in the conventional hybrid tandem device may come from the improper light path inside the device, and an inappropriate device configuration for the PBDTTPD:PC_{71}BM polymer subcell. As the light encounters the CQD subcell after it enters the device, most of the light in the absorption range of the polymer active layer would be absorbed by the CQD active layer, leaving insufficient

light to be absorbed by the polymer subcell. This would result in a limited highest achievable J_{sc} for the whole device. The inappropriate inverted device configuration adopted in the PBDTTPD:$PC_{71}BM$ polymer subcell further limited the performance of the polymer subcell, in turn limiting the PCE of the hybrid tandem.

Compared to the challenging task of changing the light path inside the device, combining an appropriate conventional device configuration for the PBDTTPD:$PC_{71}BM$ polymer subcell with an inverted CQD subcell to construct inverted hybrid tandem provides a relatively simple strategy to improve the device performance. Hence, an inverted

Table 5-1: Summarized figures of merit for bottom-illuminated conventional and inverted hybrid tandem device, along with the performance of single-junction devices.

	Device	J_{sc}	V_{oc} (V)	FF (%)	PCE (%)
Conventional hybrid tandem	CQD	14.46	0.56	50.49	4.1
	PBDTTPD (Inverted)	11.6	0.89	67.29	7
	Tandem	5.46	1.38	70.27	5.32
Inverted hybrid tandem	CQD (Inverted)	12.2	0.47	62.0	3.57
	PBDTTPD	12.5	0.92	66.6	7.7
	Tandem (Inverted)	6.77	1.37	72.1	6.74

hybrid tandem device was constructed with the device structure shown in Figure 5.2c. In an inverted hybrid tandem device, a solution-processed PBDTTPD:$PC_{71}BM$ conventional polymer subcell is deposited on top of an inverted CQD subcell prepared by layer-by-layer deposition of CQD on a PEDOT:PSS-coated ITO glass. A combined layer of solution processed ZnO with thermally evaporated 1 nm Al and 16 nm MoO_x functions as the

recombination layer and is inserted between the two subcells. The device is completed by thermally evaporating 7 nm Ca and 120 nm Al on top of the polymer active layer. The *J*–V characteristics curve for the inverted hybrid tandem with optimized recombination of active layer thicknesses is shown in Figure 5.2d along with the performance of the single-junction polymer and inverted CQD device. The figures of merit for the hybrid tandem and single-junction devices are summarized in Table 5.1. The single junction inverted CQD device shows a J_{sc} of 12.2 mA cm^{-2} with a reduced V_{oc} of 0.47 V. The reduced V_{oc} in the inverted CQD device compared to the conventional CQD device may come from the difference in Fermi level between ZnO and TiO_2.[301] The FF of the inverted CQD device is 62% and the PCE is 3.5%. The conventional PBDTTPD:PC_{71}BM single-junction device processed on a PEDOT:PSS-coated ITO glass substrate had an active layer thickness of 90 nm, and showed a J_{sc} of 12.5 mA cm^{-2} with a V_{oc} of 0.92 V and an FF of 66.6%. The PCE for this polymer device was 7.7%. Compared to the single junction polymer device with an inverted device configuration, the conventional PBDTTPD:PC_{71}BM single-junction device shows a higher J_{sc}, which may be caused by the improved build-in potential represented by the higher V_{oc}. The V_{oc} of the inverted tandem is 1.37 V, representing over 98% of the sum of the V_{oc} values of the individual cells. The impressive FF of around 72% indicates that the electrons that flow from the CQD subcell and the holes that flow from the polymer subcell recombine efficiently at the ZnO/ultra-thin Al/MoO_x interlayer, which results in insignificant electrical losses. Benefitting from the improved charge carrier extraction in the conventional polymer subcell, the inverted hybrid tandem device shows increased J_{sc} as compare to that in the

conventional hybrid tandem, yielding a value of 6.7 mA cm^{-2}. With the increased J_{sc} and enhanced FF, the conventional hybrid tandem shows an improved PCE of 6.7%.

To continuously improve the device performance for the hybrid tandem, the problem of possessing an improper light path in the two previously mentioned hybrid tandem device structures should be solved. By replacing the reflective metal electrode with a transparent conductive electrode, the direction of light incidence can be alternated from the CQD subcell to the polymer subcell. In this way, satisfactory and complementary

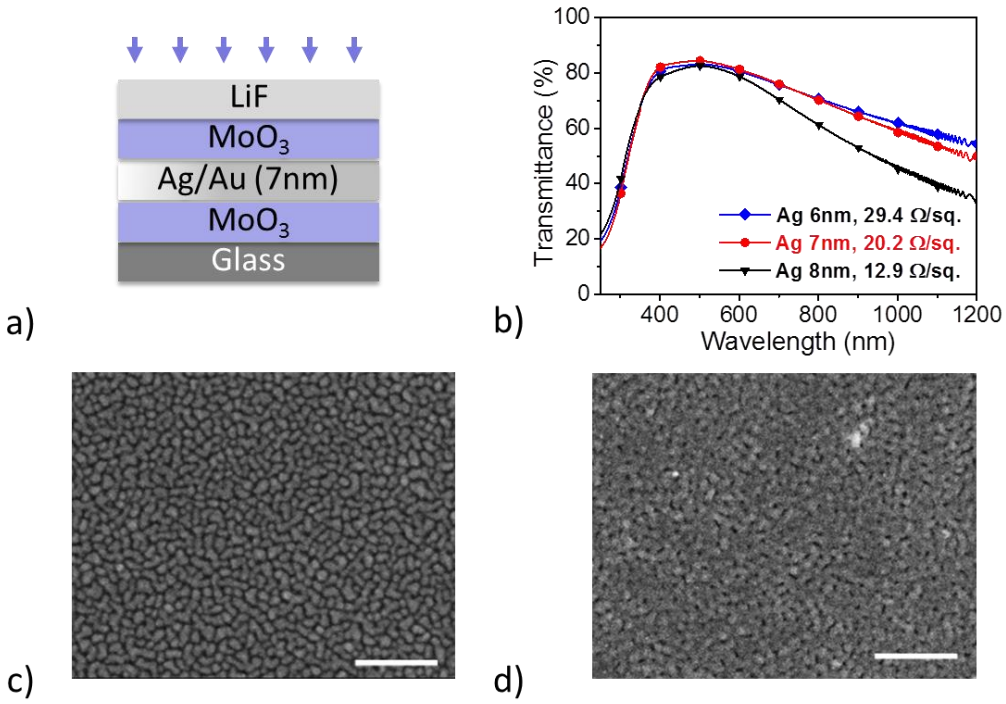

Figure 5.3: (a) Schematic description of the utilized transparent conductive electrode structure. (b) Transmittance and sheet resistance for the transparent conductive electrode with varied Ag thickness. SEM image of 7 nm Ag film deposited on MoO_x (c) without insertion of 1 nm Au and (d) with insertion of 1 nm Au.

light absorption can be achieved and the performance of the hybrid tandem can be improved. For clarification, the device structure of the polymer subcell stacked on top of the CQD subcell with light incident from the polymer side will be referred to as the “top-illuminated hybrid tandem”.

There are several ways to construct the transparent conductive electrode.[333-337] Among them, ultrathin metal (with a thickness smaller than the light penetration depth) and metal nanowires are two successful representatives. Considering the solution-processed metal nanowires may induce solvent compatibility issues, ultrathin metals that can be easily realized by using the popular thermal evaporation technique are used as the transparent conductive electrode in this study. The structure of utilized transparent conductive electrode in this study is shown in Figure 5.3a. A 20-nm MoO_x evaporated on top of glass was used as the substrate to simulate the surface conditions of the polymer subcell. Then an ultra-thin 1-nm Au was evaporated, followed by a thin layer of Ag with a thickness less than 10 nm. Another 20-nm MoO_x was deposited after that to act as a protective layer. Lastly, a 50-nm LiF with a low refractive index was deposited to reduce the light reflection at the interface. The insertion of the ultra-thin 1-nm Au elevates the surface energy of the substrate, in turn suppressing the nucleation of the deposited Ag. Therefore, a percolated Ag film was achieved at a reduced thickness, resulting in improved transparency. As compared to the electrode without the ultra-thin Au layer, the electrode with the ultra-thin Au layer indeed showed a smoother surface (Figure 5.3c and Figure 5.3d). The electrical and optical properties of the transparent conductive

electrode were checked first (Figure 5.3 b). With an optimized Ag film thickness of 7 nm, the electrode showed a peak transmittance of over 80% at 500 nm and a reduced transmittance in the near infrared region. The sheet resistance of the transparent conductive electrode with 7-nm Ag film is 20.2 Ω/sq, which is comparable to the sheet resistance of 15 Ω/sq for an ITO coated glass substrate.

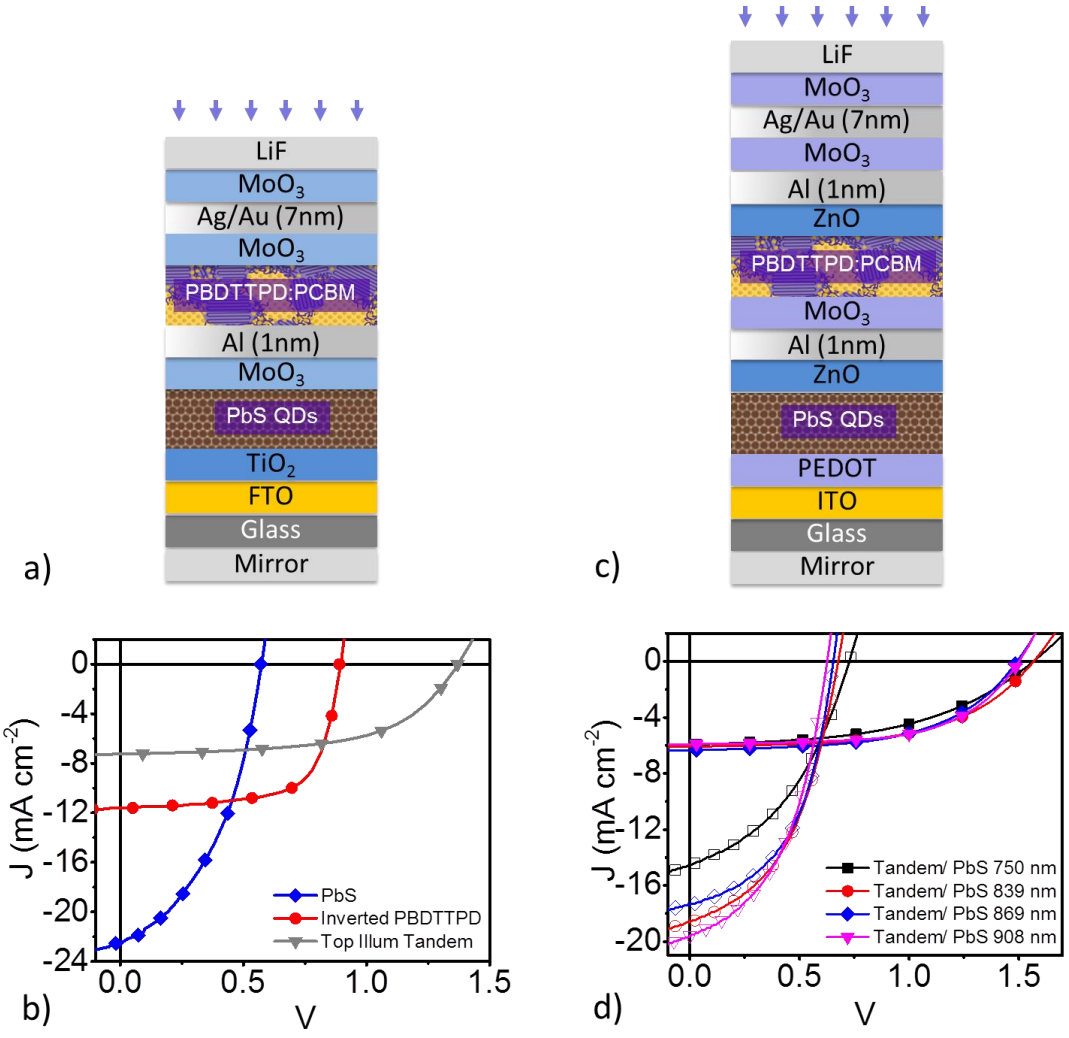

Figure 5.4: Schematic device structure for top-illuminated conventional hybrid tandem. (b) *J*-V characteristic curves of the optimized top-illuminated conventional hybrid tandem devices and single-junction devices. (c) Schematic device structure for top-illuminated inverted hybrid tandem. (d) *J*-V characteristic curves of the preliminary

constructed top-illuminated conventional hybrid tandem devices with different sized CQDs and single-junction devices.

By replacing the reflective metal electrode with the thin Ag-based transparent conductive electrode and leaving the device structure in the bottom-illuminated conventional hybrid tandem unchanged, the top-illuminated conventional hybrid tandem was constructed with the device structure shown in Figure 5.4a. The *J*-V curve for the top-illuminated conventional hybrid tandem with an optimized recombination of active layer thicknesses is shown in Figure 5.4b along with the performance of the single-junction CQD and polymer device. The figures of merit for the hybrid tandem and single-junction devices are summarized in Table 5.2. As the light is absorbed by the polymer

Table 5-2: Summarized figures of merit for top-illuminated conventional hybrid tandem device, along with the performance of single-junction devices.

Device	J_{sc}	V_{oc} (V)	FF (%)	PCE (%)
CQD	22.44	0.57	42.88	5.53
PBDTTPD	11.60	0.89	67.29	7
Tandem	7.25	1.37	57.8	5.76

subcell first, the CQD active layer can be made thicker to absorb more light. The optimized hybrid tandem was fabricated by the combination of a 180-nm CQD active layer and a 110-nm polymer active layer. With an increased CQD active layer thickness, the single-junction CQD device showed an elevated J_{sc} with a value of 22.4 mA cm^{-2}, a FF of 42%, and a PCE of 5.5%. The V_{oc} of the top-illuminated conventional hybrid tandem had similar values as the one in the bottom-illuminated device (1.37 V vs. 1.38 V, respectively), indicating that the thin Ag based transparent conductive electrode works

well in the hybrid tandem. Indeed, with alternated light incidence direction, the top-illuminated conventional hybrid tandem showed increased J_{sc} with a value of 7.2 mA cm^{-2}, a ~30% improvement compared to the bottom-illuminated one. However, the decreased FF of 57.8% limited the further enhancement of the device performance, and resulted in a PCE value of 5.7%. The low FF may result from the improper light incidence direction for the CQD subcell. In the top-illuminated conventional hybrid tandem device, the light encounters the quasi-neutral region of the CQD active first, and then the depleted space charge region formed near the CQD/TiO_2 heterojunction interface. Therefore, much more intensive charge carriers are generated in the quasi-neutral region instead of the depleted space charge region. As the extraction of charge carriers

Table 5-3: Summarized figures of merit for top-illuminated conventional hybrid tandem device with different size of CQDs, along with the performance of single-junction devices.

	CQD	J_{sc}	V_{oc} (V)	FF (%)	PCE (%)
Single junction	750 nm	14.52	0.72	40.87%	4.32%
	839 nm	18.59	0.67	45.68%	5.75%
	869 nm	17.34	0.65	49.17%	5.58%
	908 nm	21.26	0.62	44.30%	5.85%
Hybrid tandem	750 nm	5.94	1.56	47.93%	4.46%
	839 nm	6.09	1.56	54.52%	5.21%
	869 nm	6.34	1.49	54.50%	5.17%
	908 nm	5.91	1.50	59.58%	5.29%

in quasi-neutral region mainly depends on carrier diffusion, the device would show reduced FF as compared to the one with light illuminated from the side of the depleted region.[321] In order to address the improper light irradiation problem for the CQD subcell, the top-illuminated inverted hybrid tandem with inverted CQD subcell was constructed with the device structure shown in Figure 5.4c. In this device configuration, as the depleted region formed by the CQD/ZnO heterojunction is close to the polymer subcell, the device is expected to have improved performance. However, preliminary results show a PCE of 4.2% (J_{sc}: 7.26 mA cm^{-2}, V_{oc}: 1.11 V, FF: 51.9%), which may be owing to the changed surface condition for thermal deposition of the transparent conductive electrode (changed from relative smooth polymer/glass surface to a rough ZnO nanoparticle surface).

Finally, we checked the device performance for the top-illuminated conventional hybrid tandem with CQD of different sizes. The preliminary results with unoptimized active layer thicknesses are shown in Figure 5.4. The figures of merit for single-junction CQD and hybrid tandem devices are summarized in Table 5.3. As V_{oc} of the hybrid tandem was sacrificed in favor of the FF, the preliminary results did not indicate that great improvement could be achieved by using different sized CQDs.

5.4 Conclusion

In conclusion, CQD with broad absorption spectrum covering from visible to near infrared range and polymer:fullerene bulk heterojunction with strong absorption in the visible range was joined together to make a hybrid CQD–polymer tandem solar cell.

Different device architectures were proposed and tested. In the bottom-illuminated conventional hybrid tandem, the J_{sc} was limited by the improper light path and inappropriate inverted device configuration for the used polymer subcell, which resulted in an unimpressive PCE of 5.3%. Bottom-illuminated inverted hybrid tandem was then constructed to address the issue of inappropriate device configuration for the polymer subcell, and showed a 20% improvement in J_{sc} with an impressive FF of 72%, resulting in a PCE of 6.7%. This is the best performing state-of-the-art hybrid CQD-polymer tandem. To address the issue of improper light path, a thin Ag-based transparent conductive electrode was used to replace the top reflective metal electrode, and a top-illuminated hybrid tandem was constructed. Even though, 30% improvement in J_{sc} was realized in the top-illuminated conventional hybrid tandem, only a slightly higher PCE of 5.7% was obtained due to the low FF of the device. This was attributed to the improper light incidence direction for the CQD subcell. The proposed top-illuminated inverted hybrid tandem shows a preliminary PCE of 4.2%, and is still under investigation. It is ultimately expected to give better device performance.

Chapter 6

Conclusions and Future Work

6.1 Conclusions

In this dissertation, the application of nanostructured materials and multi-junction structure in PSCs has been investigated with the motivation to reduce the maintenance and production costs for PSCs. The following results were obtained.

Transparent superhydrophobic surfaces based on nanostructured materials were proposed to be integrated with PSCs to make self-cleaning PSCs with reduced maintenance costs. Two strategies were investigated to give transparent superhydrophobic surfaces. In the first strategy, solid SiO_2-coated ZnO nanorod arrays were used as a template to construct a transparent superhydrophobic surface. We show that the length of ZnO nanorods should be controlled to be under the length scale of visible light wavelength to reach a good compromise between transparency and superhydrophobicity. Through systematic optimization of the seed layer thickness, length of ZnO nanorods and thickness of the SiO_2 layer, a superhydrophobic surface with an average transmission of 93-95% was achieved. The thin layer of SiO_2 coated on the surface of the ZnO nanorods makes the superhydrophobic surface resistant to UV irradiation with no distinguishable transparency reduction. Double-sided tape and water drop tests showed that the superhydrophobic SiO_2/ZnO nanocomposite has good

adhesion strength and could survive in rainfall conditions. However, the failure in the sand bursting test suggested that the mechanical strength of the nanocomposite should be further enhanced. Integrating the superhydrophobic SiO_2/ZnO nanocomposite in PSCs imparts the self-cleaning property to PSCs with minimal degradation in the solar cell device performance. In the second strategy, hollow silica half-nanopsheres directly grown on the substrate were used as template to construct the transparent superhydrophobic surface. It was shown that by performing a concurrent BF process and hydrolysis step under a saturated atmosphere of TEOS precursor and ammonia vapors, arrays of hollow silica half-nanospheres can be directly grown on the substrate. The size of the half-nanospheres can be changed from 100 nm to 700 nm by controlling the deposition conditions. It was also shown that a transparent superhydrophobic surface can be realized using submicrometer sized silica half-nanospheres. Nanoindentation characterization showed that the Young's modulus of the hollow silica half-nanospheres was ~52 GPa. The decent mechanical property of silica and "direct-grown" protocol is expected to give improved mechanical durability for the transparent superhydrophobic surface.

Two different applications of multi-junction device structure in PSCs were also investigated. In multi-junction PSCs, we have shown that efficient homo-tandem and triple-junction PSCs can be constructed from an identical polymer absorber (PBDTTPD). Compared to single-junction PSCs in which the active layer thickness is constrained by the balance between a strong optical interference effect and relatively modest carrier

mobilities, homo-tandem PSCs with stacked identical active layers had enhanced light absorption while preserving the high charge carrier extraction efficiency, and reached higher PCE values (8.35% vs. 8.3% for the model) than single-junction PSC devices (7.7%). Combined optical and electrical modeling was also performed to simulate the multi-junction device performance, and acceptable consistency with the experimental results was demonstrated. With PCEs > 8%, V_{OC} > 1.8V and operating voltages of ~1.5 V at maximum power point, the homo-tandem PSCs constructed from PBDTTPD are the highest-efficiency high-voltage tandem PSCs reported to date. Benefitting from the high open voltage (>1.8 V) achieved in homo-tandem PSCs, OPV-driven water splitting with an estimated solar-to-fuel conversion efficiency of ~ 6% was achieved.

We also showed that the polymer subcell can be joined with a CQD subcell to construct hybrid CQD-polymer tandem devices. Different hybrid tandem device architectures were proposed and tested. In the conventional hybrid tandem, with illumination from the CQD side, the MoO_x/ultra-thin Al acts as an efficient recombination layer and results in a hybrid tandem device with a PCE of 5.3%. To improve the charge carrier extraction in the polymer subcell, an inverted hybrid tandem was constructed with a conventional polymer subcell stacked on an inverted CQD subcell. With light illuminated from the CQD side, the inverted hybrid tandem showed an increased J_{sc} and gave an improved PCE of 6.7%. A thin Ag-film-based transparent conductive electrode was used to replace the top reflective metal electrode to alter the light incidence direction in the hybrid tandem. The conventional hybrid tandem with light illumination from the polymer side

showed a 30% improvement in J_{sc}. But the decreased FF limited further enhancement in device performance and resulted in a PCE value of 5.7%.

6.2 Future work

Table 6-1: Various metal oxides achievable by low-temperature atomic layer deposition (ALD) with volatile metalorganics as precursor and H_2O as reactant.
[a]: Young's Modulus is taken from the database of National Institute of Standards and Technology (NIST)[338]

Metal Oxides	Mohs Hardness	Young's Modulus (GPa)[a]	Refractive (n)	Temperature (°C)	Precursor	Detail	Reactivity
B_2O_3				20[339]	BBr_3	H_2O	high
ZnO	4.5	30	2	40[340]	$ZnEt_2$	H_2O, FRI	
HfO_2	5.5	63	2.1	85[341]	$Hf(N(Me)_2)_4$	H_2O	
TiO_2	5.5-6.5	65	2.5	35[342]	$Ti(OiPr)_4$	H_2O	high
SiO_2	6-7	73	1.5	25[343]	TEOS	H_2O, NH_3	low
ZrO_2	8-8.5	90	2.2	25[344]	$Zr(N(Me)_2)_4$	H_2O, UV	
Al_2O_3	9	220	1.7	33[345]	TMA	H_2O	high
Diamond	10	1220	2.4				

As mentioned in the conclusion, developing a transparent supherhydrophobic surface with sufficient mechanical robustness to support low-maintenance self-cleaning PSCs is still an interesting but challenging task. Demonstration of directly grown hollow half-nanospheres via the breath figure process offers a chance to achieve a transparent superhydrophobic surface with improved mechanical properties. Similar to chemical vapor deposition of silica, most metal oxides achievable by the low-temperature vapor deposition process use volatile metalorganics as precursors and H_2O as the reactant (summarized in Table 6.1). Hence, selective hydrolysis of the metalorganic precursor at the air/water interface would result in a thin layer of metal oxide to cover the condensed water droplets. Hollow metal oxide half-nanospheres could potentially be

obtained by removing the water droplet via simple evaporation in vacuo. One of the representative metal oxides achievable by low-temperature atomic layer deposition is Al_2O_3, which has been long utilized in industry as a high dielectric material for gate oxides and to passivate semiconductor surfaces.[346-348] Compared to fused silica, which has a Mohs hardness of 7, Al_2O_3 shows a much higher Mohs hardness of 9 (compared to 10 in diamonds), which would give promising mechanical strength to the half-nanosphere structure.[349-350] Moreover, the low refractive index of Al_2O_3 (1.6–1.7) makes it a perfect candidate for constructing mechanically robust transparent superhydrophobic surfaces, which can be applied in PSCs to keep the surface clean with little maintenance. However, due to the difference in vapor pressure and reactivity of the precursor, the deposition conditions to initiate selective hydrolysis of the precursor at the air/water interface could be quite different from one to another. For example, the attempt to reach hollow half-nanosphere in TiO_2 with the same conditions we used for silica results in hydrolysis of $Ti(OiPr)_4$ before it evaporates into the space. Therefore, sophisticated deposition equipment will need to be designed to control the deposition conditions to guarantee a successful vapor deposition. Another benefit of using the sophisticated deposition equipment is that the water condensation and precursor hydrolysis process can be potentially separated to give a program-controllable size of the half-nanospheres.

Another interesting and potentially achievable outlook for the hollow half-nanosphere structure is spatial control of the position of the hollow half-nanospheres on the surface

through general surface patterning techniques. According to Volmer's classical nucleation theory, the intrinsic wettability of the surface in terms of the contact angle θ determines the free energy barrier for the formation of a liquid nucleus on a flat surface: $\Delta G = \frac{\pi \gamma_{lv} r^{*2}}{3}(2 - 3cos\theta + cos^3\theta)$, where γ_{lv} is the liquid-vapor surface energy, and r^* is the critical radius. r^* is determined from Kelvin's classical equation and mainly depends on the ratio of the environmental vapor pressure and the equilibrium vapor pressure on the flat liquid surface. Therefore, water would prefer to condense on the hydrophilic region rather than the hydrophobic region. Furthermore, the exponential correlation between the nucleation rate and the free energy barrier ($J = J_0 \exp(-\frac{\Delta G}{kT})$, where J_0 is a kinetic constant) further enhance the water condensation in the hydrophilic region. In this way, a patterned surface with alternated hydrophilic and hydrophobic regions achievable from general surface patterning techniques could result in selective water condensation in the hydrophilic region. This would allow for the spatial position of the hollow structure to be controlled (here, the hollow structure would be determined by the shape of the hydrophilic region, not only confined to be hemispheres). A schematic illustration of this is shown in Figure 6.1. Specifically, traditional photolithography/microcontact printing can be adopted to make surface patterns on the microscale, while nanoparticle lithography would be the best choice to give a simple demonstration on the nanoscale.

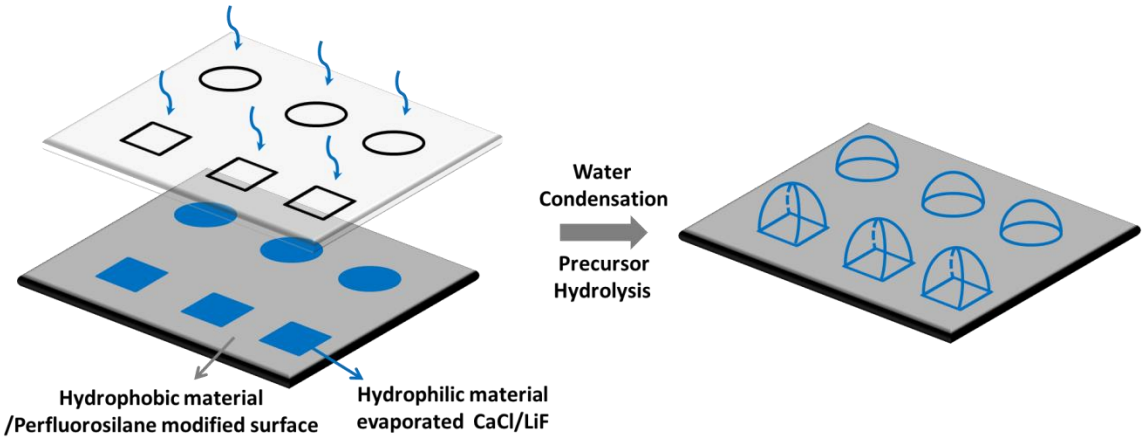

Figure 6.1: Schematic illustration for spatial control of the position of the hollow half-nanospheres on the surface.

The formed hollow structure can be also used as a template to construct nanostructured PSCs (Figure 6.2). Nanostructured PSCs or thin film a-Si:H solar cells with similar spherical structure have shown superior J_{sc} as compared to the planar device, which is attributed to the light trapping effect.[351-360] The light trapping effect can be simply explained as shown in Figure 6.3. Instead of easily escaping the device structure, as typical in planar devices, most of the light reflected at the glass/absorber interface would be reflected into the critical angle for glass/air interface (~ 41.5˚) due to the interface roughness.[131-132] The reflected light would be totally reflected at the glass/air interface and re-enter the absorber so that light would be confined within the device, leading to enhanced absorption. Furthermore, as the transmitted light at the glass/absorber interface is refracted to different angles, the light path within the device would be increased, resulting in a further enhance the light absorption. With the ability to control the size, shape and density of the hollow structure, the effect of the geometric design of the hollow structure on the light trapping efficiency in

nanostructured PSCs can be investigated.[352-354, 360] Benefitting from the relatively smooth transition from the protruding part to the flat area in the hollow structure, sharp tips-induced short circuit or non-uniform stacking of the following layers would be expected to be suppressed. This strategy may also find applications in nanostructured light emitting diodes to enhance the optical out-coupling of the device.[361-362]

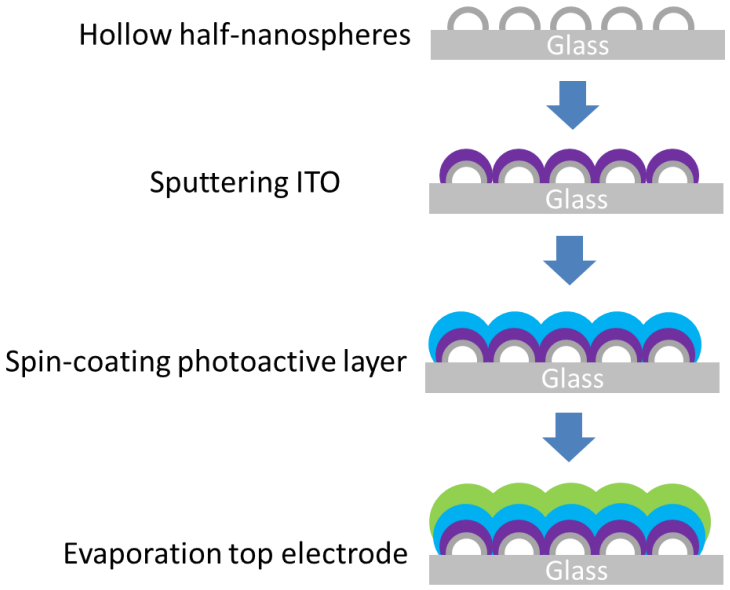

Figure 6.2: Schematic illustration of the fabrication process flow for a nanostructured PSC by using hollow half-nanosphere structure as template.

The BF approach is also believed to be a powerful way to achieve nanostructure control for favorable applications. During the development of the hollow half-nanosphere, it was observed that nanolenses can be incidentally form in defect areas. These nanolenses can sometimes self-assemble into micro-sized hollow spheres which mimic the compound eyes of insects. Even though the detailed mechanism of this formation is unknown currently, it gives us about how to use BFs to engineer nanolense structures.

Promising application of nanolenses includes high-resolution lithography,[363] near-field imaging for subdiffraction-limit resolution,[364-367] and sensitivity enhancement in detection of nanoparticles and viruses.[368-369] The development of these analytical techniques is limited due to the lack of a simple way to produce uniform sub-wavelength nanolenses.

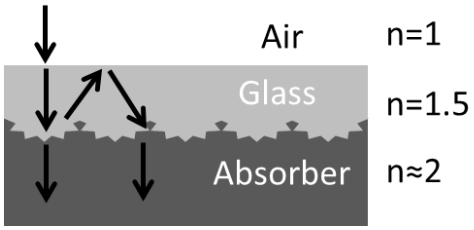

Figure 6.3: Schematic illustration of the light trapping mechanism in nanostructured PSCs.

Regarding the CQD–polymer hybrid tandem, breakthroughs reported recently for CQD solar cells give promising directions to improve the hybrid tandem device performance. With the development of perovskite passivated CQDs and realization of band alignment from ligand exchange, the charge extraction efficiency can be enhanced and the PCE of CQD solar cell was pushed up to 8.95%.[370-371] Adopting the best CQD device architecture with improved charge extraction efficiency in the CQD-polymer hybrid tandem is expected to give the best hybrid tandem device performance.

REFERENCES

1. Leahy, M., Barden, J. L., Murphy, B. T., Slater-thompson, N. & Peterson, D., In International Energy Outlook 2013.
2. Nathan, S. L., George, C., Arthur, J. N., Michael, R. W. & A., P., In Basic Research Needs for Solar Energy Utilization 2005.
3. Crabtree, G. W. & Lewis, N. S. *Phys. Today* **60,** 37-42 (2007).
4. Lewis, N. S. *Science* **315,** 798-801 (2007).
5. http://www.efficientenergysaving.co.uk/solar-irradiance-calculator.html.
6. Arnulf, J. W., In Pv status report 2014. JRC Scientific and Technical Reports: **2015**.
7. Chiang, C. K., Fincher, C. R., Park, Y. W., Heeger, A. J., Shirakawa, H., Louis, E. J., Gau, S. C. & Macdiarmid, A. G. *Phys. Rev. Lett.* **39,** 1098-1101 (1977).
8. Shirakawa, H., Louis, E. J., Macdiarmid, A. G., Chiang, C. K. & Heeger, A. J. *J. Chem. Soc., Chem. Commun.* 578-580 (1977).
9. Thompson, B. C. & Frechet, J. M. J. *Angew. Chem. Int. Edit.* **47,** 58-77 (2008).
10. Sondergaard, R., Hosel, M., Angmo, D., Larsen-Olsen, T. T. & Krebs, F. C. *Mater. Today* **15,** 36-49 (2012).
11. Li, G., Zhu, R. & Yang, Y. *Nat. Photonics* **6,** 153-161 (2012).
12. Brabec, C. J., Gowrisanker, S., Halls, J. J. M., Laird, D., Jia, S. J. & Williams, S. P. *Adv. Mater.* **22,** 3839-3856 (2010).
13. NREL Best res. Effic. http://www.nrel.gov/ncpv/images/efficiency_chart.jpg.
14. Ito, T., Shirakawa, H. & Ikeda, S. *J. Polym. Sci., Polym. Chem. Ed.* **12,** 11-20 (1974).
15. Shirakawa, H. & Ikeda, S. *J. Polym. Sci., Polym. Chem. Ed.* **12,** 929-937 (1974).
16. Ito, T., Shirakawa, H. & Ikeda, S. *J. Polym. Sci., Polym. Chem. Ed.* **13,** 1943-1950 (1975).
17. Kuhn, H. *The Journal of Chemical Physics* **17,** 1198-1212 (1949).
18. Ovchinnikov, A. A., Ukrainskiĭ, I. I. & Kventsel', G. V. *Soviet Physics Uspekhi* **15,** 575-591 (1973).
19. Chiang, C. K., Druy, M. A., Gau, S. C., Heeger, A. J., Louis, E. J., Macdiarmid, A. G., Park, Y. W. & Shirakawa, H. *J. Am. Chem. Soc.* **100,** 1013-1015 (1978).
20. Chiang, C. K., Gau, S. C., Fincher, C. R., Park, Y. W., Macdiarmid, A. G. & Heeger, A. J. *Appl. Phys. Lett.* **33,** 18-20 (1978).
21. Su, W. P., Schrieffer, J. R. & Heeger, A. J. *Phys. Rev. Lett.* **42,** 1698-1701 (1979).
22. Su, W. P., Schrieffer, J. R. & Heeger, A. J. *Phys. Rev. B* **22,** 2099-2111 (1980).
23. Takayama, H., Linliu, Y. R. & Maki, K. *Phys. Rev. B* **21,** 2388-2393 (1980).
24. Campbell, D. K. & Bishop, A. R. *Phys. Rev. B* **24,** 4859-4862 (1981).
25. Mele, E. J. & Rice, M. J. *Phys. Rev. B* **23,** 5397-5412 (1981).
26. Shacklette, L. W., Chance, R. R., Ivory, D. M., Miller, G. G. & Baughman, R. H. *Synthetic. Met.* **1,** 307-320 (1980).
27. Sheng, P. *Phys. Rev. B* **21,** 2180-2195 (1980).
28. Kivelson, S. *Phys. Rev. Lett.* **46,** 1344-1348 (1981).
29. Chance, R. R., Bredas, J. L. & Silbey, R. *Phys. Rev. B* **29,** 4491-4495 (1984).
30. Chung, T. C., Moraes, F., Flood, J. D. & Heeger, A. J. *Phys. Rev. B* **29,** 2341-2343 (1984).
31. Chung, T. C., Kaufman, J. H., Heeger, A. J. & Wudl, F. *Mol. Cryst. Liq. Cryst.* **118,** 205-215 (1985).
32. Heeger, A. J. *Polym. J.* **17,** 201-208 (1985).
33. Heeger, A. J. *Philos. Trans. R. Soc., A* **314,** 17-35 (1985).
34. Chiang, C. K., Park, Y. W., Heeger, A. J., Shirakawa, H., Louis, E. J. & Macdiarmid, A. G. *J. Chem. Phys.* **69,** 5098-5104 (1978).

35. Duke, C. B., Paton, A., Salaneck, W. R., Thomas, H. R., Plummer, E. W., Heeger, A. J. & Macdiarmid, A. G. *Chem. Phys. Lett.* **59,** 146-150 (1978).
36. Shirakawa, H., Ito, T. & Ikeda, S. *Macromol. Chem. Phys.* **179,** 1565-1573 (1978).
37. Fincher, C. R., Ozaki, M., Tanaka, M., Peebles, D., Lauchlan, L., Heeger, A. J. & Macdiarmid, A. G. *Phys. Rev. B* **20,** 1589-1602 (1979).
38. Wnek, G. E., Chien, J. C. W., Karasz, F. E. & Lillya, C. P. *Polymer* **20,** 1441-1443 (1979).
39. Ivory, D. M., Miller, G. G., Sowa, J. M., Shacklette, L. W., Chance, R. R. & Baughman, R. H. *The Journal of Chemical Physics* **71,** 1506-1507 (1979).
40. Roncali, J. *Chem. Rev.* **92,** 711-738 (1992).
41. Cheng, Y. J., Yang, S. H. & Hsu, C. S. *Chem. Rev.* **109,** 5868-5923 (2009).
42. Weinberger, B. R., Akhtar, M. & Gau, S. C. *Synthetic. Met.* **4,** 187-197 (1982).
43. Glenis, S., Tourillon, G. & Garnier, F. *Thin Solid Films* **139,** 221-231 (1986).
44. Marks, R. N., Halls, J. J. M., Bradley, D. D. C., Friend, R. H. & Holmes, A. B. *J. Phys-condens. Mat.* **6,** 1379-1394 (1994).
45. Gregg, B. A. *J. Phys. Chem. B* **107,** 4688-4698 (2003).
46. Tang, C. W. *Appl. Phys. Lett.* **48,** 183-185 (1986).
47. Sariciftci, N. S., Braun, D., Zhang, C., Srdanov, V. I., Heeger, A. J., Stucky, G. & Wudl, F. *Appl. Phys. Lett.* **62,** 585-587 (1993).
48. Mihailetchi, V. D., van Duren, J. K. J., Blom, P. W. M., Hummelen, J. C., Janssen, R. A. J., Kroon, J. M., Rispens, M. T., Verhees, W. J. H. & Wienk, M. M. *Adv. Funct. Mater.* **13,** 43-46 (2003).
49. Mikhnenko, O. V., Blom, P. W. M. & Nguyen, T.-Q. *Energy Environ. Sci.* **8,** 1867-1888 (2015).
50. Halls, J. J. M., Walsh, C. A., Greenham, N. C., Marseglia, E. A., Friend, R. H., Moratti, S. C. & Holmes, A. B. *Nature* **376,** 498-500 (1995).
51. Yu, G., Gao, J., Hummelen, J. C., Wudl, F. & Heeger, A. J. *Science* **270,** 1789-1791 (1995).
52. Yu, G. & Heeger, A. J. *J. Appl. Phys.* **78,** 4510-4515 (1995).
53. Shaheen, S. E., Brabec, C. J., Sariciftci, N. S., Padinger, F., Fromherz, T. & Hummelen, J. C. *Appl. Phys. Lett.* **78,** 841-843 (2001).
54. Peet, J., Kim, J. Y., Coates, N. E., Ma, W. L., Moses, D., Heeger, A. J. & Bazan, G. C. *Nat. Mater.* **6,** 497-500 (2007).
55. Li, G., Shrotriya, V., Huang, J. S., Yao, Y., Moriarty, T., Emery, K. & Yang, Y. *Nat. Mater.* **4,** 864-868 (2005).
56. Padinger, F., Rittberger, R. S. & Sariciftci, N. S. *Adv. Funct. Mater.* **13,** 85-88 (2003).
57. Campoy-Quiles, M., Ferenczi, T., Agostinelli, T., Etchegoin, P. G., Kim, Y., Anthopoulos, T. D., Stavrinou, P. N., Bradley, D. D. C. & Nelson, J. *Nat. Mater.* **7,** 158-164 (2008).
58. Yiu, A. T., Beaujuge, P. M., Lee, O. P., Woo, C. H., Toney, M. F. & Frechet, J. M. J. *J. Am. Chem. Soc.* **134,** 2180-2185 (2012).
59. Li, Y. F. *Accounts. Chem. Res.* **45,** 723-733 (2012).
60. Liu, Y. H., Zhao, J. B., Li, Z. K., Mu, C., Ma, W., Hu, H. W., Jiang, K., Lin, H. R., Ade, H. & Yan, H. *Nat. Commun.* **5,** 5293 (2014).
61. Zhou, Y. H., Fuentes-Hernandez, C., Shim, J., Meyer, J., Giordano, A. J., Li, H., Winget, P., Papadopoulos, T., Cheun, H., Kim, J., Fenoll, M., Dindar, A., Haske, W., Najafabadi, E., Khan, T. M., Sojoudi, H., Barlow, S., Graham, S., Bredas, J. L., Marder, S. R., Kahn, A. & Kippelen, B. *Science* **336,** 327-332 (2012).
62. Yang, X., Chueh, C. C., Li, C. Z., Yip, H. L., Yin, P. P., Chen, H. Z., Chen, W. C. & Jen, A. K. Y. *Adv. Energy Mater.* **3,** 666-673 (2013).
63. Li, C. Z., Chang, C. Y., Zang, Y., Ju, H. X., Chueh, C. C., Liang, P. W., Cho, N., Ginger, D. S. & Jen, A. K. Y. *Adv. Mater.* **26,** 6262-6267 (2014).

64. Chen, J. D., Zhou, L., Ou, Q. D., Li, Y. Q., Shen, S., Lee, S. T. & Tang, J. X. *Adv. Energy Mater.* **4,** 1777 (2014).
65. Chang, Y. M., Zhu, R., Richard, E., Chen, C. C., Li, G. & Yang, Y. *Adv. Funct. Mater.* **22,** 3284-3289 (2012).
66. Atwater, H. A. & Polman, A. *Nat. Mater.* **9,** 205-213 (2010).
67. Walter, M. G., Warren, E. L., McKone, J. R., Boettcher, S. W., Mi, Q., Santori, E. A. & Lewis, N. S. *Chem. Rev.* **110,** 6446-73 (2010).
68. Son, J., Kundu, S., Verma, L. K., Sakhuja, M., Danner, A. J., Bhatia, C. S. & Yang, H. *Sol. Energ. Mat. Sol. C.* **98,** 46-51 (2012).
69. Elminir, H. K., Ghitas, A. E., Hamid, R. H., El-Hussairly, F., Beheary, M. M. & Abdel-Moneim, K. M. *Energ. Convers. Manage* **47,** 3192-3203 (2006).
70. Kalowekamo, J. & Baker, E. *Sol. Energy* **83,** 1224-1231 (2009).
71. Wagner, T., Neinhuis, C. & Barthlott, W. *Acta Zool-stockholm.* **77,** 213-225 (1996).
72. Neinhuis, C. & Barthlott, W. *Ann. Bot-london.* **79,** 667-677 (1997).
73. Sun, T. L., Feng, L., Gao, X. F. & Jiang, L. *Accounts. Chem. Res.* **38,** 644-652 (2005).
74. Liu, M. J., Wang, S. T. & Jiang, L. *Mrs. Bull.* **38,** 375-382 (2013).
75. Wenzel, R. N. *Ind. Eng. Chem.* **28,** 988-994 (1936).
76. Cassie, A. B. D. & Baxter, S. *Trans. Faraday Soc.* **40,** 0546-0550 (1944).
77. Young, T. *Philos. Trans. R. Soc. London* **95,** 65-87 (1805).
78. Tuteja, A., Choi, W., Ma, M. L., Mabry, J. M., Mazzella, S. A., Rutledge, G. C., McKinley, G. H. & Cohen, R. E. *Science* **318,** 1618-1622 (2007).
79. Tuteja, A., Choi, W., Mabry, J. M., McKinley, G. H. & Cohen, R. E. *Proc. Natl. Acad. Sci. U. S. A.* **105,** 18200-18205 (2008).
80. Liu, T. Y. & Kim, C. J. *Science* **346,** 1096-1100 (2014).
81. Bico, J., Marzolin, C. & Quere, D. *Europhys. Lett.* **47,** 220-226 (1999).
82. Krupenkin, T. N., Taylor, J. A., Wang, E. N., Kolodner, P., Hodes, M. & Salamon, T. R. *Langmuir* **23,** 9128-9133 (2007).
83. Verho, T., Korhonen, J. T., Sainiemi, L., Jokinen, V., Bower, C., Franze, K., Franssila, S., Andrew, P., Ikkala, O. & Ras, R. H. A. *Proc. Natl. Acad. Sci. U. S. A.* **109,** 10210-10213 (2012).
84. Johnson, R. E. & Dettre, R. H. *J. Phys. Chem.* **68,** 1744-1750 (1964).
85. Patankar, N. A. *Langmuir* **19,** 1249-1253 (2003).
86. Papadopoulos, P., Mammen, L., Deng, X., Vollmer, D. & Butt, H. J. *Proc. Natl. Acad. Sci. U. S. A.* **110,** 3254-3258 (2013).
87. Tadanaga, K., Katata, N. & Minami, T. *J. Am. Ceram. Soc.* **80,** 3213-3216 (1997).
88. Nakajima, A., Fujishima, A., Hashimoto, K. & Watanabe, T. *Adv. Mater.* **11,** 1365-1368 (1999).
89. Lau, K. K. S., Bico, J., Teo, K. B. K., Chhowalla, M., Amaratunga, G. A. J., Milne, W. I., McKinley, G. H. & Gleason, K. K. *Nano Lett.* **3,** 1701-1705 (2003).
90. Shirtcliffe, N. J., McHale, G., Newton, M. I. & Perry, C. C. *Langmuir* **19,** 5626-5631 (2003).
91. Roig, A., Molins, E., Rodriguez, E., Martinez, S., Moreno-Manas, M. & Vallribera, A. *Chem. Commun.* 2316-2317 (2004).
92. Zhai, L., Cebeci, F. C., Cohen, R. E. & Rubner, M. F. *Nano Lett.* **4,** 1349-1353 (2004).
93. Dorrer, C. & Ruhe, J. *Adv. Mater.* **20,** 159-163 (2008).
94. Levkin, P. A., Svec, F. & Frechet, J. M. J. *Adv. Funct. Mater.* **19,** 1993-1998 (2009).
95. Artus, G. R. J. & Seeger, S. *Adv. Colloid Interfac* **209,** 144-162 (2014).
96. Sacher, E., Sapieha, J. K., Schrieber, H. P., Wertheimer, N. R. & McIntyre, N. S., In Silanes, surfaces, and interfaces. **1986**; Vol. I. London, p 189-202.
97. Morra, M., Occhiello, E. & Garbassi, F. *Langmuir* **5,** 872-876 (1989).
98. Oner, D. & McCarthy, T. J. *Langmuir* **16,** 7777-7782 (2000).

99. Teshima, K., Sugimura, H., Inoue, Y., Takai, O. & Takano, A. *Langmuir* **19,** 10624-10627 (2003).
100. Shirtcliffe, N. J., Aqil, S., Evans, C., McHale, G., Newton, M. I., Perry, C. C. & Roach, P. *J. Micromech. Microeng* **14,** 1384-1389 (2004).
101. Tserepi, A. D., Vlachopoulou, M. E. & Gogolides, E. *Nanotechnology* **17,** 3977-3983 (2006).
102. Choi, C. H. & Kim, C. J. *Nanotechnology* **17,** 5326-5333 (2006).
103. Gao, L. C. & McCarthy, T. J. *J. Am. Chem. Soc.* **128,** 9052-9053 (2006).
104. Rao, A. V., Bhagat, S. D., Hirashima, H. & Pajonk, G. M. *J. Colloid Interf. Sci* **302,** 705-705 (2006).
105. Wang, L. L., Zhang, X. T., Fu, Y., Li, B. & Liu, Y. C. *Langmuir* **25,** 13619-13624 (2009).
106. Ji, J., Fu, J. H. & Shen, J. C. *Adv. Mater.* **18,** 1441-1444 (2006).
107. Liu, Y., Lin, Z. Y., Lin, W., Moon, K. S. & Wong, C. P. *ACS Appl. Mater. Interfaces* **4,** 3959-3964 (2012).
108. Artus, G. R. J., Jung, S., Zimmermann, J., Gautschi, H. P., Marquardt, K. & Seeger, S. *Adv. Mater.* **18,** 2758-2762 (2006).
109. Deng, X., Mammen, L., Butt, H. J. & Vollmer, D. *Science* **335,** 67-70 (2012).
110. Artus, G. R. J. & Seeger, S. *Ind. Eng. Chem. Res.* **51,** 2631-2636 (2012).
111. Rahmawan, Y., Xu, L. B. & Yang, S. *J. Mater. Chem. A* **1,** 2955-2969 (2013).
112. Fresnais, J., Chapel, J. P. & Poncin-Epaillard, F. *Surf. Coat. Tech.* **200,** 5296-5305 (2006).
113. Vourdas, N., Tserepi, A. & Gogolides, E. *Nanotechnology* **18,** (2007).
114. Di Mundo, R., Palumbo, F. & d'Agostino, R. *Langmuir* **24,** 5044-5051 (2008).
115. Her, E. K., Ko, T. J., Shin, B., Roh, H., Dai, W., Seong, W. K., Kim, H. Y., Lee, K. R., Oh, K. H. & Moon, M. W. *Plasma Processes Polym.* **10,** 481-488 (2013).
116. Kwak, G., Seol, M., Tak, Y. & Yong, K. *J. Phys. Chem. C* **113,** 12085-12089 (2009).
117. Kim, J. H., Lee, M., Lim, T. Y., Hwang, J. H., Kim, E. & Kim, S. H. *J. Ceram. Process. Res.* **11,** 259-262 (2010).
118. Kwak, G., Jung, S. & Yong, K. *Nanotechnology* **22,** (2011).
119. Park, H. K., Yoon, S. W., Chung, W. W., Min, B. K. & Do, Y. R. *J. Mater. Chem. A* **1,** 5860-5867 (2013).
120. Kumar, P. S., Sundaramurthy, J., Zhang, X., Mangalaraj, D., Thavasi, V. & Ramakrishna, S. *J. Alloy. Compd.* **553,** 375-382 (2013).
121. Verho, T., Bower, C., Andrew, P., Franssila, S., Ikkala, O. & Ras, R. H. A. *Adv. Mater.* **23,** 673-678 (2011).
122. Cao, L. L. & Gao, D. *Faraday. Discuss.* **146,** 57-65 (2010).
123. Karunakaran, R. G., Lu, C. H., Zhang, Z. H. & Yang, S. *Langmuir* **27,** 4594-4602 (2011).
124. Xu, L. B., Karunakaran, R. G., Guo, J. & Yang, S. *ACS Appl. Mater. Interfaces* **4,** 1118-1125 (2012).
125. Hsu, S. H., Chang, Y. L., Tu, Y. C., Tsai, C. M. & Su, W. F. *ACS Appl. Mater. Interfaces* **5,** 2991-2998 (2013).
126. de Francisco, R., Tiemblo, P., Hoyos, M., Gonzalez-Arellano, C., Garcia, N., Berglund, L. & Synytska, A. *ACS Appl. Mater. Interfaces* **6,** 18998-19010 (2014).
127. Dyett, B. P., Wu, A. H. & Lamb, R. N. *ACS Appl. Mater. Interfaces* **6,** 18380-18394 (2014).
128. Deng, X., Mammen, L., Zhao, Y. F., Lellig, P., Mullen, K., Li, C., Butt, H. J. & Vollmer, D. *Adv. Mater.* **23,** 2962-2965 (2011).
129. Retsch, M., Schmelzeisen, M., Butt, H. J. & Thomas, E. L. *Nano Lett.* **11,** 1389-1394 (2011).
130. Xu, L. & He, J. *Langmuir* **28,** 7512-8 (2012).
131. Yablonovitch, E. *J. Opt. Soc. Am.* **72,** 899-907 (1982).
132. Yablonovitch, E. & Cody, G. D. *IEEE. T. Electron Dev.* **29,** 300-305 (1982).

133. Bartelt, J. A., Beiley, Z. M., Hoke, E. T., Mateker, W. R., Douglas, J. D., Collins, B. A., Tumbleston, J. R., Graham, K. R., Amassian, A., Ade, H., Frechet, J. M. J., Toney, M. F. & McGehee, M. D. *Adv. Energy Mater.* **3,** 364-374 (2013).
134. Sista, S., Hong, Z. R., Chen, L. M. & Yang, Y. *Energy Environ. Sci.* **4,** 1606-1620 (2011).
135. Hadipour, A., de Boer, B. & Blom, P. W. M. *Adv. Funct. Mater.* **18,** 169-181 (2008).
136. Brongersma, M. L., Cui, Y. & Fan, S. H. *Nat. Mater.* **13,** 451-460 (2014).
137. Rand, B. P., Peumans, P. & Forrest, S. R. *J. Appl. Phys.* **96,** 7519-7526 (2004).
138. Kim, S. S., Na, S. I., Jo, J., Kim, D. Y. & Nah, Y. C. *Appl. Phys. Lett.* **93,** (2008).
139. Lindquist, N. C., Luhman, W. A., Oh, S. H. & Holmes, R. J. *Appl. Phys. Lett.* **93,** (2008).
140. Kim, J. B., Kim, P., Pegard, N. C., Oh, S. J., Kagan, C. R., Fleischer, J. W., Stone, H. A. & Loo, Y. L. *Nat. Photonics* **6,** 327-332 (2012).
141. Tang, Z., Elfwing, A., Bergqvist, J., Tress, W. & Inganas, O. *Adv. Energy Mater.* **3,** 1606-1613 (2013).
142. Chen, J.-D., Cui, C., Li, Y.-Q., Zhou, L., Ou, Q.-D., Li, C., Li, Y. & Tang, J.-X. *Adv. Mater.* 4535-4541 (2014).
143. Zhou, L., Ou, Q. D., Chen, J. D., Shen, S., Tang, J. X., Li, Y. Q. & Lee, S. T. *Scientific Reports* **4,** (2014).
144. Chen, C.-C., Chang, W.-H., Yoshimura, K., Ohya, K., You, J., Gao, J., Hong, Z. & Yang, Y. *Adv. Mater.* **26,** 5670-5677 (2014).
145. You, J. B., Dou, L. T., Yoshimura, K., Kato, T., Ohya, K., Moriarty, T., Emery, K., Chen, C. C., Gao, J., Li, G. & Yang, Y. *Nat. Commun.* **4,** 1446 (2013).
146. You, J. B., Chen, C. C., Hong, Z. R., Yoshimura, K., Ohya, K., Xu, R., Ye, S. L., Gao, J., Li, G. & Yang, Y. *Adv. Mater.* **25,** 3973-3978 (2013).
147. Kang, H., Kee, S., Yu, K., Lee, J., Kim, G., Kim, J., Kim, J.-R., Kong, J. & Lee, K. *Adv. Mater.* **27,** 1408-1413 (2014).
148. Zhou, H., Zhang, Y., Mai, C. K., Collins, S. D., Bazan, G. C., Nguyen, T. Q. & Heeger, A. J. *Adv. Mater.* **27,** 1767 (2015).
149. Shockley, W. & Queisser, H. J. *J. Appl. Phys.* **32,** 510-519 (1961).
150. Luo, J. S., Im, J. H., Mayer, M. T., Schreier, M., Nazeeruddin, M. K., Park, N. G., Tilley, S. D., Fan, H. J. & Gratzel, M. *Science* **345,** 1593-1596 (2014).
151. Cook, T. R., Dogutan, D. K., Reece, S. Y., Surendranath, Y., Teets, T. S. & Nocera, D. G. *Chem. Rev.* **110,** 6474-502 (2010).
152. McCrory, C. C. L., Jung, S. H., Peters, J. C. & Jaramillo, T. F. *J. Am. Chem. Soc.* **135,** 16977-16987 (2013).
153. Kanan, M. W. & Nocera, D. G. *Science* **321,** 1072-1075 (2008).
154. May, M. M., Lewerenz, H. J., Lackner, D., Dimroth, F. & Hannappel, T. *Nat. Commun.* **6,** (2015).
155. Licht, S., Wang, B., Mukerji, S., Soga, T., Umeno, M. & Tributsch, H. *J. Phys. Chem. B* **104,** 8920-8924 (2000).
156. Esiner, S., van Eersel, H., Wienk, M. M. & Janssen, R. A. J. *Adv. Mater.* **25,** 2932-2936 (2013).
157. Gao, Y., Gereige, I., El Labban, A., Cha, D., Isimjan, T. T. & Beaujuge, P. M. *ACS Appl. Mater. Interfaces* **6,** 2219-2223 (2014).
158. Kota, A. K., Li, Y. X., Mabry, J. M. & Tuteja, A. *Adv. Mater.* **24,** 5838-5843 (2012).
159. Bhushan, B., Jung, Y. C. & Koch, K. *Langmuir* **25,** 3240-3248 (2009).
160. Zhu, J., Hsu, C. M., Yu, Z. F., Fan, S. H. & Cui, Y. *Nano Lett.* **10,** 1979-1984 (2010).
161. Nishimoto, S. & Bhushan, B. *RSC Adv.* **3,** 671-690 (2013).
162. Chen, Y., Zhang, Y. B., Shi, L., Li, J., Xin, Y., Yang, T. T. & Guo, Z. G. *Appl. Phys. Lett.* **101,** 033701 (2012).

163. Lai, Y. K., Tang, Y. X., Gong, J. J., Gong, D. G., Chi, L. F., Lin, C. J. & Chen, Z. *J. Mater. Chem.* **22,** 7420-7426 (2012).
164. Mertaniemi, H., Jokinen, V., Sainiemi, L., Franssila, S., Marmur, A., Ikkala, O. & Ras, R. H. A. *Adv. Mater.* **23,** 2911-2914 (2011).
165. Shirtcliffe, N. J., McHale, G., Newton, M. I. & Zhang, Y. *ACS Appl. Mater. Interfaces* **1,** 1316-1323 (2009).
166. Jin, H., Kettunen, M., Laiho, A., Pynnonen, H., Paltakari, J., Marmur, A., Ikkala, O. & Ras, R. H. A. *Langmuir* **27,** 1930-1934 (2011).
167. Zahner, D., Abagat, J., Svec, F., Frechet, J. M. J. & Levkin, P. A. *Adv. Mater.* **23,** 3030-3034 (2011).
168. Mumm, F., van Helvoort, A. T. J. & Sikorski, P. *ACS Nano* **3,** 2647-2652 (2009).
169. Yao, X., Song, Y. L. & Jiang, L. *Adv. Mater.* **23,** 719-734 (2011).
170. You, I., Kang, S. M., Lee, S., Cho, Y. O., Kim, J. B., Lee, S. B., Nam, Y. S. & Lee, H. *Angew. Chem. Int. Edit.* **51,** 6126-6130 (2012).
171. Park, Y. B., Im, H., Im, M. & Choi, Y. K. *J. Mater. Chem.* **21,** 633-636 (2011).
172. Arias, A. C., MacKenzie, J. D., McCulloch, I., Rivnay, J. & Salleo, A. *Chem. Rev.* **110,** 3-24 (2010).
173. Ebert, D. & Bhushan, B. *Langmuir* **28,** 11391-11399 (2012).
174. Zhang, X., Kono, H., Liu, Z., Nishimoto, S., Tryk, D. A., Murakami, T., Sakai, H., Abe, M. & Fujishima, A. *Chem. Commun.* 4949-4951 (2007).
175. Tarwal, N. L. & Patil, P. S. *Appl. Surf. Sci.* **256,** 7451-7456 (2010).
176. Xue, C. H., Yin, W., Jia, S. T. & Ma, J. Z. *Nanotechnology* **22,** 415603 (2011).
177. Kwak, G., Jung, S. & Yong, K. *Nanotechnology* **22,** 115705 (2011).
178. Lee, Y. J., Ruby, D. S., Peters, D. W., McKenzie, B. B. & Hsu, J. W. P. *Nano Lett.* **8,** 1501-1505 (2008).
179. Clapham, P. B. & Hutley, M. C. *Nature* **244,** 281-282 (1973).
180. Raguin, D. H. & Morris, G. M. *Appl. Opt.* **32,** 1154-1167 (1993).
181. Sugunan, A., Warad, H. C., Boman, M. & Dutta, J. *J. Sol-Gel Sci. Technol.* **39,** 49-56 (2006).
182. Yoshikawa, H. & Adachi, S. *Jpn. J. Appl. Phys.* **36,** 6237-6243 (1997).
183. Liu, J., She, J. C., Deng, S. Z., Chen, J. & Xu, N. S. *J. Phys. Chem. C* **112,** 11685-11690 (2008).
184. Enger, R. C. & Case, S. K. *Appl. Opt.* **22,** 3220-3228 (1983).
185. Nishino, T., Meguro, M., Nakamae, K., Matsushita, M. & Ueda, Y. *Langmuir* **15,** 4321-4323 (1999).
186. Qin, H. C., Li, W. Y., Xia, Y. J. & He, T. *ACS Appl. Mater. Interfaces* **3,** 3152-3156 (2011).
187. Tian, Z. R. R., Voigt, J. A., Liu, J., McKenzie, B., McDermott, M. J., Rodriguez, M. A., Konishi, H. & Xu, H. F. *Nat. Mater.* **2,** 821-826 (2003).
188. Beard, K. V. *J. Atmos. Sci.* **33,** 851-864 (1976).
189. Spilhaus, A. F. *J. Meteorol.* **5,** 108-110 (1948).
190. Beaujuge, P. M. & Frechet, J. M. J. *J. Am. Chem. Soc.* **133,** 20009-20029 (2011).
191. Cabanetos, C., El Labban, A., Bartelt, J. A., Douglas, J. D., Mateker, W. R., Frechet, J. M. J., McGehee, M. D. & Beaujuge, P. M. *J. Am. Chem. Soc.* **135,** 4656-4659 (2013).
192. Piliego, C., Holcombe, T. W., Douglas, J. D., Woo, C. H., Beaujuge, P. M. & Frechet, J. M. J. *J. Am. Chem. Soc.* **132,** 7595-7597 (2010).
193. Lee, Y. J., Sounart, T. L., Scrymgeour, D. A., Voigt, J. A. & Hsu, J. W. P. *J. Cryst. Growth* **304,** 80-85 (2007).
194. Kim, M. K., Yi, D. K. & Paik, U. *Langmuir* **26,** 7552-7554 (2010).
195. Ahn, H., Park, J. H., Kim, S. B., Jee, S. H., Yoon, Y. S. & Kim, D. J. *Electrochem. Solid-State Lett.* **13,** J125-J128 (2010).

196. Gao, Y. Q., Hou, Y. F. & Beaujuge, P. M. *Adv. Mater. Interfaces* **2,** 1500078-1500087 (2015).
197. Spurr, R. T. & Butlin, J. G. *Nature* **179,** 1187-1187 (1957).
198. Beysens, D. & Knobler, C. M. *Phys. Rev. Lett.* **57,** 1433-1436 (1986).
199. Family, F. & Meakin, P. *Phys. Rev. Lett.* **61,** 428-431 (1988).
200. Knobler, C. M. & Beysens, D. *Europhys. Lett.* **6,** 707-712 (1988).
201. Fritter, D., Knobler, C. M. & Beysens, D. A. *Phys. Rev. A* **43,** 2858-2869 (1991).
202. Blaschke, J., Lapp, T., Hof, B. & Vollmer, J. *Phys. Rev. Lett.* **109,** (2012).
203. Rayleigh, L. *Nature* **86,** 416-418 (1911).
204. Miljkovic, N., Enright, R. & Wang, E. N. *ACS Nano* **6,** 1776-1785 (2012).
205. Paxson, A. T., Yague, J. L., Gleason, K. K. & Varanasi, K. K. *Adv. Mater.* **26,** 418-423 (2014).
206. Widawski, G., Rawiso, M. & Francois, B. *Nature* **369,** 387-389 (1994).
207. Kabuto, T., Hashimoto, Y. & Karthaus, O. *Adv. Funct. Mater.* **17,** 3569-3573 (2007).
208. Galeotti, F., Andicsova, A., Yunus, S. & Botta, C. *Soft Matter* **8,** 4815-4821 (2012).
209. Wan, L. S., Li, J. W., Ke, B. B. & Xu, Z. K. *J. Am. Chem. Soc.* **134,** 95-98 (2012).
210. Zhu, Y. D., Sheng, R. L., Luo, T., Li, H., Sun, J. J., Chen, S. D., Sun, W. Y. & Cao, A. *ACS Appl. Mater. Interfaces* **3,** 2487-2495 (2011).
211. Stenzel, M. H., Barner-Kowollik, C. & Davis, T. P. *J. Polym. Sci. Pol. Chem* **44,** 2363-2375 (2006).
212. Li, X. F., Zhang, L. A., Wang, Y. X., Yang, X. L., Zhao, N., Zhang, X. L. & Xu, J. A. *J. Am. Chem. Soc.* **133,** 3736-3739 (2011).
213. Kon, K., Brauer, C. N., Hidaka, K., Lohmannsroben, H. G. & Karthaus, O. *Langmuir* **26,** 12173-12176 (2010).
214. Boker, A., Lin, Y., Chiapperini, K., Horowitz, R., Thompson, M., Carreon, V., Xu, T., Abetz, C., Skaff, H., Dinsmore, A. D., Emrick, T. & Russell, T. P. *Nat. Mater.* **3,** 302-306 (2004).
215. Connal, L. A. & Qiao, G. G. *Adv. Mater.* **18,** 3024-3028 (2006).
216. Bunz, U. H. F. *Adv. Mater.* **18,** 973-989 (2006).
217. Park, J. S., Lee, S. H., Han, T. H. & Kim, S. O. *Adv. Funct. Mater.* **17,** 2315-2320 (2007).
218. Yabu, H. & Shimomura, M. *Langmuir* **21,** 1709-1711 (2005).
219. Yabu, H. & Shimomura, M. *Chem. Mater.* **17,** 5231-5234 (2005).
220. Yabu, H., Takebayashi, M., Tanaka, M. & Shimomura, M. *Langmuir* **21,** 3235-3237 (2005).
221. Brown, P. S., Talbot, E. L., Wood, T. J., Bain, C. D. & Badyal, J. P. S. *Langmuir* **28,** 13712-13719 (2012).
222. Hernandez-Guerrero, M. & Stenzel, M. H. *Polym. Chem.* **3,** 563-577 (2012).
223. Bai, H., Du, C., Zhang, A. J. & Li, L. *Angew. Chem. Int. Edit.* **52,** 12240-12255 (2013).
224. Dadgostar, S., Tajabadi, F. & Taghavinia, N. *ACS Appl. Mater. Interfaces* **4,** 2964-2968 (2012).
225. Koo, H. J., Kim, Y. J., Lee, Y. H., Lee, W. I., Kim, K. & Park, N. G. *Adv. Mater.* **20,** 195-199 (2008).
226. Li, H. X., Bian, Z. F., Zhu, J., Zhang, D. Q., Li, G. S., Huo, Y. N., Li, H. & Lu, Y. F. *J. Am. Chem. Soc.* **129,** 8406-8407 (2007).
227. Balgar, T., Bautista, R., Hartmann, N. & Hasselbrink, E. *Surf. Sci.* **532,** 963-969 (2003).
228. Banga, R., Yarwood, J., Morgan, A. M., Evans, B. & Kells, J. *Langmuir* **11,** 4393-4399 (1995).
229. Bunker, B. C., Carpick, R. W., Assink, R. A., Thomas, M. L., Hankins, M. G., Voigt, J. A., Sipola, D., de Boer, M. P. & Gulley, G. L. *Langmuir* **16,** 7742-7751 (2000).
230. Jung, G. Y., Li, Z. Y., Wu, W., Chen, Y., Olynick, D. L., Wang, S. Y., Tong, W. M. & Williams, R. S. *Langmuir* **21,** 1158-1161 (2005).

231. Hozumi, A., Ushiyama, K., Sugimura, H. & Takai, O. *Langmuir* **15,** 7600-7604 (1999).
232. Legrange, J. D., Markham, J. L. & Kurkjian, C. R. *Langmuir* **9,** 1749-1753 (1993).
233. Gau, H. & Herminghaus, S. *Phys. Rev. Lett.* **84,** 4156-4159 (2000).
234. Rykaczewski, K., Chinn, J., Walker, M. L., Scott, J. H. J., Chinn, A. & Jones, W. *ACS Nano* **5,** 9746-9754 (2011).
235. Rykaczewski, K., Landin, T., Walker, M. L., Scott, J. H. J. & Varanasi, K. K. *ACS Nano* **6,** 9326-9334 (2012).
236. Rykaczewski, K., Osborn, W. A., Chinn, J., Walker, M. L., Scott, J. H. J., Jones, W., Hao, C. L., Yao, S. H. & Wang, Z. K. *Soft Matter* **8,** 8786-8794 (2012).
237. Seo, D., Lee, C. & Nam, Y. *Langmuir* **30,** 15468-76 (2014).
238. Dennler, G., Scharber, M. C., Ameri, T., Denk, P., Forberich, K., Waldauf, C. & Brabec, C. J. *Adv. Mater.* **20,** 579-583 (2008).
239. Liang, J. J., Huang, L., Li, N., Huang, Y., Wu, Y. P., Fang, S. L., Oh, J. Y., Kozlov, M., Ma, Y. F., Li, F. F., Baughman, R. & Chen, Y. S. *ACS Nano* **6,** 4508-4519 (2012).
240. Zhan, X. W., Facchetti, A., Barlow, S., Marks, T. J., Ratner, M. A., Wasielewski, M. R. & Marder, S. R. *Adv. Mater.* **23,** 268-284 (2011).
241. Zhou, H. X., Yang, L. Q. & You, W. *Macromolecules.* **45,** 607-632 (2012).
242. Mei, J. G. & Bao, Z. N. *Chem. Mater.* **26,** 604-615 (2014).
243. Lee, J. K., Ma, W. L., Brabec, C. J., Yuen, J., Moon, J. S., Kim, J. Y., Lee, K., Bazan, G. C. & Heeger, A. J. *J. Am. Chem. Soc.* **130,** 3619-3623 (2008).
244. Dang, M. T., Hirsch, L., Wantz, G. & Wuest, J. D. *Chem. Rev.* **113,** 3734-3765 (2013).
245. Graham, K. R., Cabanetos, C., Jahnke, J. P., Idso, M. N., El Labban, A., Ndjawa, G. O. N., Heumueller, T., Vandewal, K., Salleo, A., Chmelka, B. F., Amassian, A., Beaujuge, P. M. & McGehee, M. D. *J. Am. Chem. Soc.* **136,** 9608-9618 (2014).
246. Bartelt, J. A., Douglas, J. D., Mateker, W. R., El Labban, A., Tassone, C. J., Toney, M. F., Frechet, J. M. J., Beaujuge, P. M. & McGehee, M. D. *Adv. Energy Mater.* **4,** 1301733 (2014).
247. Hau, S. K., Yip, H. L., Acton, O., Baek, N. S., Ma, H. & Jen, A. K. Y. *J. Mater. Chem.* **18,** 5113-5119 (2008).
248. He, Z. C., Zhong, C. M., Su, S. J., Xu, M., Wu, H. B. & Cao, Y. *Nat. Photonics* **6,** 591-595 (2012).
249. He, Z. C., Wu, H. B. & Cao, Y. *Adv. Mater.* **26,** 1006-1024 (2014).
250. Jagadamma, L. K., Al-Senani, M., El-Labban, A., Gereige, I., Ngongang Ndjawa, G. O., Faria, J. C. D., Kim, T., Zhao, K., Cruciani, F., Anjum, D. H., McLachlan, M. A., Beaujuge, P. M. & Amassian, A. *Adv. Energy Mater.* **5,** 1500204 (2015).
251. Kim, J. Y., Lee, K., Coates, N. E., Moses, D., Nguyen, T. Q., Dante, M. & Heeger, A. J. *Science* **317,** 222-225 (2007).
252. Chou, C. H., Kwan, W. L., Hong, Z. R., Chen, L. M. & Yang, Y. *Adv. Mater.* **23,** 1282-1286 (2011).
253. Yang, J., Zhu, R., Hong, Z. R., He, Y. J., Kumar, A., Li, Y. F. & Yang, Y. *Adv. Mater.* **23,** 3465-3470 (2011).
254. Li, N., Stubhan, T., Baran, D., Min, J., Wang, H. Q., Ameri, T. & Brabec, C. J. *Adv. Energy Mater.* **3,** 301-307 (2013).
255. Li, W. W., Furlan, A., Hendriks, K. H., Wienk, M. M. & Janssen, R. A. J. *J. Am. Chem. Soc.* **135,** 5529-5532 (2013).
256. Lee, J., Kang, H., Kong, J. & Lee, K. *Adv. Energy Mater.* **4,** 1301226 (2014).
257. Yusoff, A. B., Kim, D., Kim, H. P., Shneider, F. K., da Silva, W. J. & Jang, J. *Energy Environ. Sci.* **8,** 303-316 (2015).
258. Dou, L. T., You, J. B., Yang, J., Chen, C. C., He, Y. J., Murase, S., Moriarty, T., Emery, K., Li, G. & Yang, Y. *Nat. Photonics* **6,** 180-185 (2012).

259. Hoke, E. T., Vandewal, K., Bartelt, J. A., Mateker, W. R., Douglas, J. D., Noriega, R., Graham, K. R., Frechet, J. M. J., Salleo, A. & McGehee, M. D. *Adv. Energy Mater.* **3,** 220-230 (2013).
260. Yuan, J. Y., Zhai, Z. C., Dong, H. L., Li, J., Jiang, Z. Q., Li, Y. Y. & Ma, W. L. *Adv. Funct. Mater.* **23,** 885-892 (2013).
261. Chen, J.-D., Cui, C., Li, Y.-Q., Zhou, L., Ou, Q.-D., Li, C., Li, Y. & Tang, J.-X. *Adv. Mater.* **27,** 1035 (2014).
262. Warnan, J., Cabanetos, C., Bude, R., El Labban, A., Li, L. & Eaujuge, P. M. *Chem. Mater.* **26,** 2829-2835 (2014).
263. Kang, T. E., Kim, T., Wang, C., Yoo, S. & Kim, B. J. *Chem. Mater.* **27,** 2653-2658 (2015).
264. Zheng, Z., Zhang, S. Q., Zhang, M. J., Zhao, K., Ye, L., Chen, Y., Yang, B. & Hou, J. H. *Adv. Mater.* **27,** 1189-1194 (2015).
265. Zou, Y. P., Najari, A., Berrouard, P., Beaupre, S., Aich, B. R., Tao, Y. & Leclerc, M. *J. Am. Chem. Soc.* **132,** 5330-+ (2010).
266. Zhang, Y., Hau, S. K., Yip, H. L., Sun, Y., Acton, O. & Jen, A. K. Y. *Chem. Mater.* **22,** 2696-2698 (2010).
267. Paraecattil, A. A., Beaupre, S., Leclerc, M., Moser, J. E. & Banerji, N. *J. Phys. Chem. Lett.* **3,** 2952-2958 (2012).
268. Mateker, W. R., Douglas, J. D., Cabanetos, C., Sachs-Quintana, I. T., Bartelt, J. A., Hoke, E. T., El Labban, A., Beaujuge, P. M., Frechet, J. M. J. & McGehee, M. D. *Energy Environ. Sci.* **6,** 2529-2537 (2013).
269. Warnan, J., Cabanetos, C., El Labban, A., Hansen, M. R., Tassone, C., Toney, M. F. & Beaujuge, P. M. *Adv. Mater.* **26,** 4357-4362 (2014).
270. El Labban, A., Warnan, J., Cabanetos, C., Ratel, O., Tassone, C., Toney, M. F. & Beaujuge, P. M. *ACS Appl. Mater. Interfaces* **6,** 19477-19481 (2014).
271. Dyer-Smith, C., Howard, I. A., Cabanetos, C., El Labban, A., Beaujuge, P. M. & Laquai, F. *Adv. Energy Mater.* **5,** 1401778 (2015).
272. Beek, W. J. E., Wienk, M. M., Kemerink, M., Yang, X. N. & Janssen, R. A. J. *J. Phys. Chem. B* **109,** 9505-9516 (2005).
273. Zhao, D. W., Sun, X. W., Jiang, C. Y., Kyaw, A. K. K., Lo, G. Q. & Kwong, D. L. *Appl. Phys. Lett.* **93,** 83305 (2008).
274. Pettersson, L. A. A., Roman, L. S. & Inganas, O. *J. Appl. Phys.* **86,** 487-496 (1999).
275. Burkhard, G. F., Hoke, E. T. & McGehee, M. D. *Adv. Mater.* **22,** 3293-3297 (2010).
276. Bartelt, J. A., Lam, D., Burke, T. M., Sweetnam, S. M. & McGehee, M. D. *Adv. Energy Mater.* DOI 10.1002/aenm.201500577 (online) (2015).
277. Hadipour, A., de Boer, B. & Blom, P. W. M. *Org. Electron.* **9,** 617-624 (2008).
278. Gilot, J., Wienk, M. M. & Janssen, R. A. J. *Adv. Mater.* **22,** E67-E71 (2010).
279. Mcgahan, W. A., Johs, B. & Woollam, J. A. *Thin Solid Films* **234,** 443-446 (1993).
280. Hilfiker, J. N., Singh, N., Tiwald, T., Convey, D., Smith, S. M., Baker, J. H. & Tompkins, H. G. *Thin Solid Films* **516,** 7979-7989 (2008).
281. Ng, A., Li, C. H., Fung, M. K., Djurisic, A. B., Zapien, J. A., Chan, W. K., Cheung, K. Y. & Wong, W. Y. *J. Phys. Chem. C* **114,** 15094-15101 (2010).
282. Lizana, A., Foldyna, M., Stchakovsky, M., Georges, B., Nicolas, D. & Garcia-Caurel, E. *J. Phys. D. Appl. Phys.* **46,** 105501 (2013).
283. Moet, D. J. D., de Bruyn, P. & Blom, P. W. M. *Appl. Phys. Lett.* **96,** 153504 (2010).
284. Riede, M., Uhrich, C., Widmer, J., Timmreck, R., Wynands, D., Schwartz, G., Gnehr, W. M., Hildebrandt, D., Weiss, A., Hwang, J., Sundarraj, S., Erk, P., Pfeiffer, M. & Leo, K. *Adv. Funct. Mater.* **21,** 3019-3028 (2011).

285. Tang, Z., George, Z., Ma, Z. F., Bergqvist, J., Tvingstedt, K., Vandewal, K., Wang, E., Andersson, L. M., Andersson, M. R., Zhang, F. L. & Inganas, O. *Adv. Energy Mater.* **2,** 1467-1476 (2012).
286. Since the spectral absorption of the two subcells overlap, the slight difference in JSC between experimental and modeling results may originate from the sensitivity of the photocurrent to the active layer thickness of the front cell. In fact, the fraction of photons transmitted to the back cell depends largely on the thickness of the front cell —light absorption decreasing exponentially with increasing front cell thickness (aside from interference effects).
287. Haverinen, H. M., Myllyla, R. A. & Jabbour, G. E. *Appl. Phys. Lett.* **94,** (2009).
288. Maenosono, S., Okubo, T. & Yamaguchi, Y. *J. Nanopart. Res.* **5,** 5-15 (2003).
289. Tang, J., Konstantatos, G., Hinds, S., Myrskog, S., Pattantyus-Abraham, A. G., Clifford, J. & Sargent, E. H. *ACS Nano* **3,** 331-338 (2009).
290. Brus, L. E. *J. Chem. Phys.* **79,** 5566-5571 (1983).
291. Brus, L. E. *J. Chem. Phys.* **80,** 4403-4409 (1984).
292. Beard, M. C., Knutsen, K. P., Yu, P. R., Luther, J. M., Song, Q., Metzger, W. K., Ellingson, R. J. & Nozik, A. J. *Nano Lett.* **7,** 2506-2512 (2007).
293. Ellingson, R. J., Beard, M. C., Johnson, J. C., Yu, P. R., Micic, O. I., Nozik, A. J., Shabaev, A. & Efros, A. L. *Nano Lett.* **5,** 865-871 (2005).
294. Luther, J. M., Beard, M. C., Song, Q., Law, M., Ellingson, R. J. & Nozik, A. J. *Nano Lett.* **7,** 1779-1784 (2007).
295. Sambur, J. B., Novet, T. & Parkinson, B. A. *Science* **330,** 63-66 (2010).
296. Semonin, O. E., Luther, J. M., Choi, S., Chen, H. Y., Gao, J. B., Nozik, A. J. & Beard, M. C. *Science* **334,** 1530-1533 (2011).
297. Ip, A. H., Thon, S. M., Hoogland, S., Voznyy, O., Zhitomirsky, D., Debnath, R., Levina, L., Rollny, L. R., Carey, G. H., Fischer, A., Kemp, K. W., Kramer, I. J., Ning, Z. J., Labelle, A. J., Chou, K. W., Amassian, A. & Sargent, E. H. *Nat. Nanotechnol.* **7,** 577-582 (2012).
298. Luther, J. M., Law, M., Beard, M. C., Song, Q., Reese, M. O., Ellingson, R. J. & Nozik, A. J. *Nano Lett.* **8,** 3488-3492 (2008).
299. Ma, W. L., Swisher, S. L., Ewers, T., Engel, J., Ferry, V. E., Atwater, H. A. & Alivisatos, A. P. *ACS Nano* **5,** 8140-8147 (2011).
300. Maraghechi, P., Labelle, A. J., Kirmani, A. R., Lan, X. Z., Adachi, M. M., Thon, S. M., Hoogland, S., Lee, A., Ning, Z. J., Fischer, A., Amassian, A. & Sargent, E. H. *ACS Nano* **7,** 6111-6116 (2013).
301. Pattantyus-Abraham, A. G., Kramer, I. J., Barkhouse, A. R., Wang, X. H., Konstantatos, G., Debnath, R., Levina, L., Raabe, I., Nazeeruddin, M. K., Gratzel, M. & Sargent, E. H. *ACS Nano* **4,** 3374-3380 (2010).
302. Rath, A. K., Bernechea, M., Martinez, L., de Arquer, F. P. G., Osmond, J. & Konstantatos, G. *Nat. Photonics* **6,** 529-534 (2012).
303. Tang, J., Liu, H., Zhitomirsky, D., Hoogland, S., Wang, X. H., Furukawa, M., Levina, L. & Sargent, E. H. *Nano Lett.* **12,** 4889-4894 (2012).
304. Green, M. A. *Prog. Photovoltaics.* **9,** 123-135 (2001).
305. Hanna, M. C. & Nozik, A. J. *J. Appl. Phys.* **100,** (2006).
306. Clifford, J. P., Johnston, K. W., Levina, L. & Sargent, E. H. *Appl. Phys. Lett.* **91,** (2007).
307. Johnston, K. W., Pattantyus-Abraham, A. G., Clifford, J. P., Myrskog, S. H., MacNeil, D. D., Levina, L. & Sargent, E. H. *Appl. Phys. Lett.* **92,** (2008).
308. Klem, E. J. D., MacNeil, D. D., Cyr, P. W., Levina, L. & Sargenta, E. H. *Appl. Phys. Lett.* **90,** (2007).
309. McDonald, S. A., Konstantatos, G., Zhang, S. G., Cyr, P. W., Klem, E. J. D., Levina, L. & Sargent, E. H. *Nat. Mater.* **4,** 138-U14 (2005).

310. Barkhouse, D. A. R., Pattantyus-Abraham, A. G., Levina, L. & Sargent, E. H. *ACS Nano* **2,** 2356-2362 (2008).
311. Kovalenko, M. V., Scheele, M. & Talapin, D. V. *Science* **324,** 1417-1420 (2009).
312. Law, M., Luther, J. M., Song, O., Hughes, B. K., Perkins, C. L. & Nozik, A. J. *J. Am. Chem. Soc.* **130,** 5974-5985 (2008).
313. Lee, J. S., Kovalenko, M. V., Huang, J., Chung, D. S. & Talapin, D. V. *Nat. Nanotechnol.* **6,** 348-352 (2011).
314. Ning, Z. J., Zhitomirsky, D., Adinolfi, V., Sutherland, B., Xu, J. X., Voznyy, O., Maraghechi, P., Lan, X. Z., Hoogland, S., Ren, Y. & Sargent, E. H. *Adv. Mater.* **25,** 1719-1723 (2013).
315. Owen, J. S., Park, J., Trudeau, P. E. & Alivisatos, A. P. *J. Am. Chem. Soc.* **130,** 12279-12281 (2008).
316. Talapin, D. V. & Murray, C. B. *Science* **310,** 86-89 (2005).
317. Yuan, M., Zhitomirsky, D., Adinolfi, V., Voznyy, O., Kemp, K. W., Ning, Z., Lan, X., Xu, J., Kim, J. Y., Dong, H. & Sargent, E. H. *Adv. Mater.* **25,** 5586-92 (2013).
318. Barkhouse, D. A. R., Debnath, R., Kramer, I. J., Zhitomirsky, D., Pattantyus-Abraham, A. G., Levina, L., Etgar, L., Gratzel, M. & Sargent, E. H. *Adv. Mater.* **23,** 3134-3138 (2011).
319. Jean, J., Chang, S., Brown, P. R., Cheng, J. J., Rekemeyer, P. H., Bawendi, M. G., Gradecak, S. & Bulovic, V. *Adv. Mater.* **25,** 2790-2796 (2013).
320. Leschkies, K. S., Jacobs, A. G., Norris, D. J. & Aydil, E. S. *Appl. Phys. Lett.* **95,** (2009).
321. Barkhouse, D. A. R., Kramer, I. J., Wang, X. H. & Sargent, E. H. *Opt. Express* **18,** A451-A457 (2010).
322. Koleilat, G. I., Levina, L., Shukla, H., Myrskog, S. H., Hinds, S., Pattantyus-Abraham, A. G. & Sargent, E. H. *ACS Nano* **2,** 833-840 (2008).
323. Sargent, E. H. *Nat. Photonics* **6,** 133-135 (2012).
324. Nano LettersChoi, J. J., Wenger, W. N., Hoffman, R. S., Lim, Y. F., Luria, J., Jasieniak, J., Marohn, J. A. & Hanrath, T. *Adv. Mater.* **23,** 3144-3148 (2011).
325. Koleilat, G. I., Wang, X. H. & Sargent, E. H. *Nano Lett.* **12,** 3043-3049 (2012).
326. Wang, X. H., Koleilat, G. I., Tang, J., Liu, H., Kramer, I. J., Debnath, R., Brzozowski, L., Barkhouse, D. A. R., Levina, L., Hoogland, S. & Sargent, E. H. *Nat. Photonics* **5,** 480-484 (2011).
327. Aldana, J., Lavelle, N., Wang, Y. J. & Peng, X. G. *J. Am. Chem. Soc.* **127,** 2496-2504 (2005).
328. Zhu, Z. J., Yeh, Y. C., Tang, R., Yan, B., Tamayo, J., Vachet, R. W. & Rotello, V. M. *Nat. Chem.* **3,** 963-968 (2011).
329. Guo, X. G., Zhou, N. J., Lou, S. J., Smith, J., Tice, D. B., Hennek, J. W., Ortiz, R. P., Navarrete, J. T. L., Li, S. Y., Strzalka, J., Chen, L. X., Chang, R. P. H., Facchetti, A. & Marks, T. J. *Nat. Photonics* **7,** 825-833 (2013).
330. Kim, S. J., Kim, W. J., Cartwright, A. N. & Prasad, P. N. *Sol. Energ. Mat. Sol. C.* **93,** 657-661 (2009).
331. Speirs, M. J., Groeneveld, B. G., Protesescu, L., Piliego, C., Kovalenko, M. V. & Loi, M. A. *Phys. Chem. Chem. Phys.* **16,** 7672-6 (2014).
332. Gonzalez-Pedro, V., Zarazua, I., Barea, E. M., Fabregat-Santiago, F., de la Rosa, E., Mora-Sero, I. & Gimenez, S. *J. Phys. Chem. C* **118,** 891-895 (2014).
333. Kang, H., Jung, S., Jeong, S., Kim, G. & Lee, K. *Nature Communications* **6,** (2015).
334. Schubert, S., Müller-Meskamp, L. & Leo, K. *Adv. Funct. Mater.* **24,** 6668-6676 (2014).
335. Schubert, S., Meiss, J., Muller-Meskamp, L. & Leo, K. *Adv. Energy Mater.* **3,** 438-443 (2013).
336. Hutter, O. S. & Hatton, R. A. *Adv. Mater.* 04263 (2014).
337. Ye, S., Rathmell, A. R., Chen, Z., Stewart, I. E. & Wiley, B. J. *Adv. Mater.* (2014).

338. Lampert, M. A. *Phys. Rev.* **103,** 1648-1656 (1956).
339. Putkonen, M. & Niinisto, L. *Thin Solid Films* **514,** 145-149 (2006).
340. Ku, C. S., Lee, H. Y., Huang, J. M. & Lin, C. M. *Mater. Chem. Phys.* **120,** 236-239 (2010).
341. Gieraltowska, S., Wachnicki, L., Witkowski, B. S., Godlewski, M. & Guziewicz, E. *Opt. Appl.* **43,** 17-25 (2013).
342. Knez, M., Kadri, A., Wege, C., Gosele, U., Jeske, H. & Nielsch, K. *Nano Lett.* **6,** 1172-1177 (2006).
343. Klaus, J. W., Sneh, O. & George, S. M. *Science* **278,** 1934-1936 (1997).
344. Duan, Y., Sun, F. B., Yang, Y. Q., Chen, P., Yang, D., Duan, Y. H. & Wang, X. *ACS Appl. Mater. Interfaces* **6,** 3799-3804 (2014).
345. Groner, M. D., Fabreguette, F. H., Elam, J. W. & George, S. M. *Chem. Mater.* **16,** 639-645 (2004).
346. Huang, M. L., Chang, Y. C., Chang, C. H., Lee, Y. J., Chang, P., Kwo, J., Wu, T. B. & Hong, M. *Appl. Phys. Lett.* **87,** (2005).
347. Xuan, Y., Lin, H. C., Ye, P. D. & Wilk, G. D. *Appl. Phys. Lett.* **88,** (2006).
348. Ye, P. D., Wilk, G. D., Kwo, J., Yang, B., Gossmann, H. J. L., Frei, M., Chu, S. N. G., Mannaerts, J. P., Sergent, M., Hong, M., Ng, K. K. & Bude, J. *IEEE. Electr. Device. L* **24,** 209-211 (2003).
349. Tapily, K., Jakes, J. E., Stone, D. S., Shrestha, P., Gu, D., Baumgart, H. & Elmustafa, A. A. *J. Electrochem. Soc.* **155,** H545-H551 (2008).
350. Zhang, L., D'Acunzi, M., Kappl, M., Auernhammer, G. K., Vollmer, D., van Kats, C. M. & van Blaaderen, A. *Langmuir* **25,** 2711-2717 (2009).
351. Chen, S. Y., Yen, Y. T., Chen, Y. Y., Hsu, C. S., Chueh, Y. L. & Chen, L. J. *RSC Adv.* **2,** 1314-1317 (2012).
352. Deceglie, M. G., Ferry, V. E., Alivisatos, A. P. & Atwater, H. A. *Nano Lett.* **12,** 2894-2900 (2012).
353. Ferry, V. E., Polman, A. & Atwater, H. A. *ACS Nano* **5,** 10055-10064 (2011).
354. Ferry, V. E., Verschuuren, M. A., van Lare, M. C., Schropp, R. E. I., Atwater, H. A. & Polman, A. *Nano Lett.* **11,** 4239-4245 (2011).
355. Gao, P. Q., He, J., Zhou, S. Q., Yang, X., Li, S. Z., Sheng, J., Wang, D., Yu, T. B., Ye, J. C. & Cui, Y. *Nano Lett.* **15,** 4591-4598 (2015).
356. Li, J. J., Zuo, L. J., Pan, H. B., Jiang, H., Liang, T., Shi, Y., Chen, H. Z. & Xu, M. S. *J. Mater. Chem. A* **1,** 2379-2386 (2013).
357. van Lare, C., Lenzmann, F., Verschuuren, M. A. & Polman, A. *Nano Lett.* **15,** 4846-52 (2015).
358. van Lare, M., Lenzmann, F. & Polman, A. *Opt. Express* **21,** 20738-20746 (2013).
359. Wei, H. Y., Huang, J. H., Hsu, C. Y., Chang, F. C., Ho, K. C. & Chu, C. W. *Energy Environ. Sci.* **6,** 1192-1198 (2013).
360. Yang, X., Zhou, S. Q., Wang, D., He, J., Zhou, J., Li, X. F., Gao, P. Q. & Ye, J. C. *Nanoscale Res. Lett.* **10,** (2015).
361. Chen, C. Y., Lee, W. K., Chen, Y. J., Lu, C. Y., Lin, H. Y. & Wu, C. C. *Adv. Mater.* 2516-2521 (2015).
362. Pintani, M., Huang, J., Ramon, M. C. & Bradley, D. D. C. *J. Phys-condens. Mat.* **19,** (2007).
363. McLeod, E. & Arnold, C. B. *Nat. Nanotechnol.* **3,** 413-417 (2008).
364. Lee, J. Y., Hong, B. H., Kim, W. Y., Min, S. K., Kim, Y., Jouravlev, M. V., Bose, R., Kim, K. S., Hwang, I. C., Kaufman, L. J., Wong, C. W., Kim, P. & Kim, K. S. *Nature* **460,** 498-501 (2009).
365. McLeod, E., Nguyen, C., Huang, P., Luo, W., Veli, M. & Ozcan, A. *ACS Nano* (2014).
366. McLeod, E. & Ozcan, A. *Nano Today* **9,** 560-573 (2014).

367. Wang, Z. B., Guo, W., Li, L., Luk'yanchuk, B., Khan, A., Liu, Z., Chen, Z. C. & Hong, M. H. *Nat. Commun.* **2,** (2011).
368. Schwartz, J. J., Stavrakis, S. & Quake, S. R. *Nat. Nanotechnol.* **5,** 127-132 (2010).
369. Mudanyali, O., McLeod, E., Luo, W., Greenbaum, A., Coskun, A. F., Hennequin, Y., Allier, C. P. & Ozcan, A. *Nat. Photonics* **7,** 247-254 (2013).
370. Yang, Z., Janmohamed, A., Lan, X., Garcia de Arquer, F. P., Voznyy, O., Yassitepe, E., Kim, G. H., Ning, Z., Gong, X., Comin, R. & Sargent, E. H. *Nano Lett.* (2015).
371. Chuang, C. H. M., Brown, P. R., Bulovic, V. & Bawendi, M. G. *Nat. Mater.* **13,** 796-801 (2014).

LIST OF PBLICATIONS

1. **Gao, Y.**; Gereige, I.; El Labban, A.; Cha, D.; Isimjan, T. T.; Beaujuge, P. M. Highly Transparent and UV-Resistant Superhydrophobic SiO_2-Coated ZnO Nanorod Arrays. *ACS Appl. Mater. Interfaces* **2014**, 6, 2219-2223.

2. **Gao, Y.**; Hou, Y. F.; Beaujuge, P. M. Arrays of Hollow Silica Half-Nanospheres Via the Breath Figure Approach. *Adv. Mater. Interfaces* **2015**, 2.

3. **Gao, Y.**; Le Corre, V.; Gaïtis, A.; Neophytou, M.; Abdul Hamid, M.; Takanabe, K.; Beaujuge, P. M. Homo-Tandem Polymer Solar Cells with $V_{OC} > 1.8$ V for Efficient PV-Driven Water Splitting. (Submitted to Advanced Materials, **2015**)

4. **Gao, Y.**; Kim, T.; Liang, R.; Ning, Z.; Adachi, M. M.; Sargent, E. H.; Amassian, A.; Beaujuge, P. M. Top-illuminated Hybrid Colloidal Quantum Dot-Polymer Bulk Heterojunction Tandem Solar Cells (In preparation)

5. Kim, T.; **Gao, Y.**; Hu, H.; Yan, B.; Ning, Z.; Jagadamma, L. K.; Zhao, K.; Kirmani, A. R.; Eid, J.; Adachi, M. M.; Sargent, E. H.; Beaujuge, P. M.; Amassian, A. Hybrid Tandem Solar cells with Depleted-Heterojunction Quantum Dot and Polymer Bulk Heterojunction Subcells. *Nano Energy* **2015**, 17, 196-205.